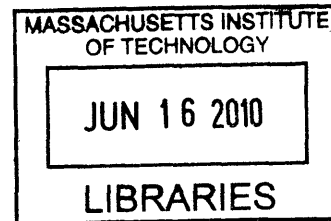


Novel Methods for Fabrication of
Non-Close-Packed Structures through Colloidal
Self-Assembly

by
Vyom Sharma



Submitted to the Department of Materials Science and Engineering
in partial fulfillment of the requirements for the degree of

Doctor of Philosophy

ARCHIVES

at the

MASSACHUSETTS INSTITUTE OF TECHNOLOGY

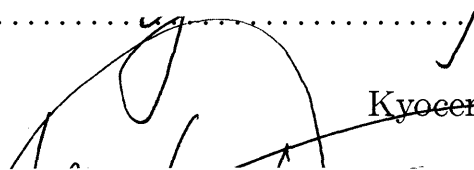
February 2010

© Massachusetts Institute of Technology 2010. All rights reserved.


Author

Department of Materials Science and Engineering
September 3, 2009

Certified by


Yet-Ming Chiang
Kyocera Professor of Ceramics
Thesis Supervisor

Certified by


W. Craig Carter
Professor of Materials Science and Engineering, MacVicar Faculty
Fellow
Thesis Supervisor

Accepted by


Christine Ortiz
Chair, Departmental Committee on Graduate Students

Novel Methods for Fabrication of Non–Close-Packed Structures through Colloidal Self-Assembly

by

Vyom Sharma

Submitted to the Department of Materials Science and Engineering
on September 3, 2009, in partial fulfillment of the
requirements for the degree of
Doctor of Philosophy

Abstract

Colloidal dispersions are usually stabilized by interparticle electrostatic repulsion. However, strong electrostatic potentials prevent nucleation of new structures. When the electrostatic potential is strongly attractive, particles coagulate into a disordered structure; if it is strongly repulsive, known processes can order them into a close-packed structure. Driven by the need to make tailored structures, researchers have focused on circumventing electrostatics to nucleate and stabilize newer structures. Yet most colloidal systems of interest are strongly charged. Reducing the electrostatic potential of a system may create only unstable structures without long-range order. In this thesis, electrostatic interaction between strongly charged particles is exploited to make novel structures. It is shown that —with an added steric component in the interaction potential— oppositely charged particles, which undergo rapid coagulation otherwise, can be arranged into stable, long-range ordered structures. Compared to their like-charged counterparts, these structures have greater stability due to an attractive electrostatic potential. It is shown that an entire class of surfactants, amphiphilic non-ionic surfactants, can be used to stabilize an oppositely charged particle system. Stabilizing these systems, allows for the nucleation of newer structures. For instance, it is shown that a non–close-packed arrangement of positive particles can be obtained on a layer of negatively charged particles. Creating such non–close-packed 2D structures on a template is essential for creating 3D non–close-packed structures. Indeed, it is shown that at high Debye lengths, by varying the concentration of particles in a suspension of like-charged colloids, electrostatic repulsion among particles can stabilize “sparse” structures. In these structures, particles occupy only a few of the many sites that are available to them. Yet, they form an ordered structure. Nuclei of a sparser structure are assembled at higher Debye length and lower particle concentration. Monte Carlo simulations confirm that these structures are stabilized by electrostatic repulsion when particle concentration is low. It is shown that the remaining sites in a sparse structure can be filled by a different particle type. By replicating this process of 2D heterostructure formation, layer by layer, and removing one kind of particle in the last step of the process, a two-layer

non-close-packed structure is obtained.

Thesis Supervisor: Yet-Ming Chiang
Title: Kyocera Professor of Ceramics

Thesis Supervisor: W. Craig Carter
Title: Professor of Materials Science and Engineering, MacVicar Faculty Fellow

Acknowledgments

Completion of a PhD thesis is a big milestone in a person's life. For me, this couldn't have been possible without the help and support of many people. This space is insufficient to thank all of them.

Foremost, I want to thank the one guiding light which has shown me the way all my life and is truly the gift of God, "Shrimad Bhagwat Gita". I am fortunate enough for extending my profound gratitude to this book of knowledge. This explained and taught me the art of living for the enrichment of my mind and heart. This enabled me to seek guidance from the superpowers at the time of confusion for the procurement of processed knowledge and flawless decision.

Next, I want to thank my mother. I definitely would not have been here without her single minded efforts and innumerable sacrifices. Completion of this thesis is truly a testimony to the efforts that she has put bringing me up and I want to dedicate this thesis to her.

I wish I could have met her before, but my wife is indeed the one person who has been with me all along in this ride. I surely will never be able to thank her enough for this. Her support and love were crucial in times of immense pressure. I hope to do bigger and greater things for her.

My thesis advisors, Prof. Yet-Ming Chiang and Prof. Craig Carter have been the most thoughtful and inspiring advisors that I could have imagined. They encouraged me to believe in my ideas and supported me all these years. I am glad that with their help, I was able to finish this work and thank them for their support. Prof. Francesco Stellacci and Prof. Karl Berggren provided crucial insight into the data analysis. This helped me analyze the data and map the trends in the experiments, clearly. Prof. Berggren also granted me access to Nano Structures Laboratory(NSL), and this work could not have been completed without this. I specially want to thank Jim Daley, for being there whenever there were problems at NSL.

My sister and brother-in-law were there for me when I needed them the most and I am thankful for their support. I want to thank them for their help through these

years.

My parents-in-law have been very supportive and helpful through this crucial time and I want to thank them for their blessings and guidance.

My collaborators during this thesis, Prof. C.C. Wong, Dr. Deying Xia, Dr. Qingfeng Yan, and Dr. Yaw Koon Woh, were very helpful. I want to thank all Chiang and Carter group members for making my stay here very fulfilling. I had many useful discussions with Dr. Garry Maskaly, Dr. Ming Tang, and Dr. Rick Rajter. I also want to thank Rubner group for allowing me to use their facilities. I want to thank my MADMEC and 100K team members.

Clearly, this space is limited. As a result, I apologize for not mentioning the names of many others who were a key to finishing this thesis.

Contents

1	Motivation and Layout of the Thesis	25
1.1	Layout of the Thesis	27
2	Colloidal Forces and Methods of Self-Assembly	29
2.1	Brownian Motion	30
2.2	Interactions between Colloidal Particles	32
2.2.1	Van der Waals Interaction	32
2.2.2	Electrostatic Interaction	34
2.2.3	Steric Interaction	41
2.2.4	Hydrophobic Interaction	42
2.3	Stability of Colloidal Dispersions: DLVO Theory	43
2.4	Self-assembly of Colloids	44
2.4.1	Methods of Self-assembly	46
2.4.2	Directed Self-assembly	48
3	Controlled Ordering of Oppositely Charged Colloidal Particles	51
3.1	Introduction	51
3.2	Materials and Methods	53
3.2.1	Colloidal suspensions	53
3.2.2	Surfactants	54
3.2.3	Solvents	55
3.2.4	Template	55
3.2.5	Spin-coating	58

3.2.6	Dip-coating	59
3.3	Spin-coating of Oppositely Charged Colloids	61
3.3.1	Surfactantless spin-coating of colloidal particles	61
3.3.2	Spin-coating of colloidal particles with non-ionic surfactant	62
3.4	Dip-Coating of Oppositely Charged Colloids	67
3.5	Theoretical Calculations	71
3.6	Colloidal Self-assembly on Charged Substrates: Role of Hydrophobicity	75
3.7	Concluding Remarks	76
4	Layer-by-Layer Self-Assembly of Non-Close-Packed Heterostructures	79
4.1	Introduction	79
4.2	Materials and Methods	81
4.2.1	Materials	81
4.2.2	Solvents	82
4.2.3	Template Preparation	83
4.2.4	Colloidal Assembly	84
4.3	Results	85
4.3.1	L1-PS: Sparse Polystyrene Layer	85
4.3.2	Results and Discussion: Mechanism of Sparse Structure Formation	92
4.3.3	Discussion: Conditions for Sparse Structure Formation	93
4.3.4	L1-Silica	96
4.3.5	L2-PS	101
4.3.6	L2-Silica	104
4.3.7	L2	112
4.4	Concluding Remarks	115
5	Stick and Slip During Convective Assembly	117
6	Monte Carlo Simulations of Sparse Ordering	121
6.1	Simulation Set-up	122

6.2	Simulation Results	124
6.3	Discussion	125
6.4	Conclusion	137
7	Conclusions and Outlook	139

List of Figures

2-1	SEM image of the top view and cross-section of a colloidal crystal of polystyrene particles. The particles assemble in a face centered cubic (f.c.c.) structure with (111) orientation relative to the substrate. . . .	45
2-2	Schematic of a convective assembly process.	48
3-1	A schematic for the Lloyd’s Mirror Interference Lithography set-up .	56
3-2	A schematic for the procedure to fabricate the template	57
3-3	SEM image of 100 nm diameter positively charged PS sphere suspension (0.25-w/v%) spin-coated at 3000 rpm on a substrate made from 420 nm diameter negatively charged PS spheres	60
3-4	100 nm diameter positively charged PS sphere suspension (1.0-w/v%) spin-coated at 3000 rpm on a substrate made from 420 nm diameter negatively charged PS spheres	60
3-5	100 nm diameter positively charged PS sphere suspension (1.0-w/v%) in isopropanol (80%) – DI water (20%) spin-coated at 3000 rpm on a substrate made from 420 nm diameter negatively charged PS spheres	63
3-6	100 nm diameter positively charged PS sphere suspension (0.25-w/v%) in DI water with Triton X-100, spin-coated at 3000 rpm on a substrate made from 420 nm diameter negatively charged PS spheres for 60 seconds	64
3-7	Pair distribution function (pdf) for small particles from fig. 3-6, σ is the diameter of the small sphere	64

3-8	210 nm diameter positively charged PS sphere suspension (1.0-w/v%) in DI water, spin-coated at 3000 rpm on a substrate made from 420 nm diameter negatively charged PS spheres for 60 seconds	65
3-9	Pair distribution function (pdf) for small particles from fig. 3-8, σ is the diameter of the small sphere	65
3-10	100 nm diameter positively charged PS sphere suspension (1.0-w/v%) in DI water, spin-coated at 6000 rpm on a substrate made from 420 nm diameter negatively charged PS spheres for 60 seconds	66
3-11	Pair distribution function (pdf) for small particles from fig. 3-10, σ is the diameter of the small sphere	66
3-12	SEM image of a larger domain with LS_6 ordering	67
3-13	SEM image of a larger domain with LS_2 ordering	68
3-14	140 nm diameter positively charged PS sphere suspension (1.0-w/v%) in DI water, spin-coated at 3000 rpm on a substrate made from 250 nm diameter negatively charged PS spheres for 60 seconds. The layer of 250 nm particles were assembled on a template with holes arranged in (100) symmetry, through convective assembly.	68
3-15	A schematic showing the first two layers for a layer-by-layer assembly of ZnS-type structure. Green spheres represent positive PS particles in the second layer and red spheres represent negative PS particles from the first layer. In the second layer only half of the total interstices are occupied.	69
3-16	A schematic showing the first three layers for the layer-by-layer as- sembly of ZnS-type structure. Green spheres represent positive PS particles in the second layer and red spheres represent negative PS particles. The position of negative particles in the third layer is shown in translucent blue.	70
3-17	A schematic showing the first four layers for a layer-by-layer assembly of ZnS-type structure. Green spheres represent positive PS particles in the fourth layer and red spheres represent negative PS particles . .	70

3-18 SEM image after a suspension of 0.1-w/v% 140 nm diameter positively charged amidine functionalized PS spheres with Triton X-100, deposited on a substrate of 420 nm negatively charged PS particles which were arranged in f.c.c. pattern with (111) orientation. The dip-coating lasted for 60 seconds	71
3-19 Normalized electrostatic force (relative to the Brownian force) and electrostatic energy (relative to $k_B T$) with respect to the position of a 100 nm positive PS sphere moving on the surface of one of the 420 nm negative PS spheres, which are packed into close packed with fcc (111) orientation. Salt concentration has been assumed to be 0.001 mM whereas the surface charge density for each kind of sphere has been assumed to be identical to the value supplied by the manufacturer. The calculation was done by solving the linearized Poisson Boltzmann equation for a system of 7 negative PS spheres and one positive PS sphere through the PoissonBoltzmann solver. For position 1, the positive PS sphere sits in the crevice formed by 3 negative PS spheres. $\theta_2 = 45^\circ, \theta_3 = 55^\circ, \theta_4 = 65^\circ, \theta_5 = 75^\circ$ and $\theta_6 = 90^\circ$	73
3-20 DLVO (van der Waals + electrostatic) interaction energy (in red) and DLVO + steric interaction energy (in blue). The above calculations are for a negative 420 nm PS and a positive 100 nm PS approaching each other in water. For the steric interaction, $\phi = 0.10, \nu_1 = 0.03nm^3$ and $\chi = 0.45$	74
3-21 DLVO + steric interaction as a function of the adsorbed surfactant volume fraction ϕ	75
4-1 SEM image of a silicon template, which has holes arranged in a pattern with (100) symmetry. The holes were 45 nm deep. This template was created according to the procedure described in section 3.2.4	83
4-2 Contact angle measurement on a bare silicon template after exposure to oxygen plasma. The contact angle was 0.80°	84

4-3	Schematic showing the different kinds of ordering seen on the template.	85
4-4	SEM image of a template after convective assembly of PS particles from a 0.025-v/v% aqueous suspension. Due to stick and slip of the meniscus, the particles assemble in bands, separated by regions on the template without any particles. In this image, bright regions are bands of PS particles, whereas dark regions are regions on the template without any particles	86
4-5	SEM image of a template, after convective assembly of 250 nm PS particles from a 0.01-v/v% aqueous suspension. The withdrawal speed of the suspension was 46.1 $\mu\text{m}/\text{min}$ at 35°C. κ^{-1} was 204 nm. This was inferred from conductivity measurement of the solvent. As seen in this image, particles arrange in a sparse pattern. The inset shows a schematic arrangement of particles on the template: red circles denote particles and open circles denote empty holes. Due to the low concentration of the particles in suspension, narrow bands of PS particles assemble on the template.	87
4-6	SEM image of a template, after convective assembly of 250 nm PS particles from a 0.025-v/v% aqueous suspension. The withdrawal speed of the suspension was 46.1 $\mu\text{m}/\text{min}$ at 35°C. κ^{-1} was 204 nm. This was inferred from conductivity measurement of the solvent. As seen in this image, particles arrange in a sparse pattern. The inset shows a schematic arrangement of particles on the template: red circles denote particles on holes and open circles denote empty holes.	88
4-7	SEM image of a template after convective assembly of 250 nm PS particles from a 0.1-v/v% aqueous suspension. The withdrawal speed of the suspension was 46.1 $\mu\text{m}/\text{min}$ at 35°C. κ^{-1} was 204 nm. This was inferred from conductivity measurement of the solvent. Due to high concentration of PS particles in the suspension, they fill all the holes in the template. The inset shows a schematic arrangement of particles on the template. Red circles denote PS particles on holes.	89

4-8	Plot of the pair distribution function for the arrangement of 250 nm PS particles in fig. 4-5 and fig. 4-6. σ is the diameter of the sphere	89
4-9	Plot of the pair distribution function for the arrangement of 250 nm PS particles in fig. 4-7. σ is the diameter of the sphere	90
4-10	SEM image of the cross-section of a template with 250 nm PS particles ordered in L1-PS arrangement	90
4-11	SEM image after convective assembly of 250 nm PS particles from a 0.025-v/v% aqueous suspension. The withdrawal speed of the suspension was 46.1 $\mu\text{m}/\text{min}$ at 35°C. κ^{-1} was 30 nm. This was inferred from conductivity measurement of the solvent. Random filling may be associated with the reduced Debye length.	91
4-12	Plot of the pair distribution function for the arrangement of 250 nm PS particles in fig. 4-11. σ is the diameter of the sphere. Due to low κ^{-1} , the arrangement shows short-range order compared to the arrangement of particles in fig. 4-6	91
4-13	SEM image of a large area of the template after convective assembly of 250 nm PS particles from their 0.025-v/v% aqueous suspension. The withdrawal speed of the suspension was 46.1 $\mu\text{m}/\text{min}$ at 35°C. κ^{-1} was 204 nm. This was inferred from conductivity measurement of solvent. This image shows a L1-PS band where PS particles are arranged akin to their arrangement in fig. 4-6. Thus, typical L1-PS domains were 15 μm wide along the direction of withdrawal of the suspension and hundreds of μm large, perpendicular to it.	92
4-14	Variation of λ_{band} and δ_{band} when PS particles were assembled onto templates, fixed at different orientations relative to the direction of withdrawal of the suspension. The suspension was withdrawn at 46.1 $\mu\text{m}/\text{min}$ at 35°C.	93
4-15	Variation of ϕ_{sparse} when PS particles were assembled onto templates, fixed at different orientations relative to the direction of withdrawal of the suspension. The suspension was withdrawn at 46.1 $\mu\text{m}/\text{min}$ at 35°C.	94

4-16	Contact angle measurement on L1-PS substrate, after it was exposed to oxygen plasma for 10 seconds. The contact angle of water was 4.7°	96
4-17	SEM image of a template with 250 nm PS particles arranged on the template. This image was taken after silica particles were assembled from a 0.025-v/v% ethanol suspension, on a substrate with 250 nm PS particles arranged on the template. PS particles are partially soluble in ethanol. As a result, they swell to 350 nm and coalesce	97
4-18	SEM image showing the arrangement of 250 nm silica and PS particles, after silica particles were assembled from a 0.025-v/v% aqueous suspension, at 50°C, on L1-PS substrate. The speed of withdrawal of the suspension was 46.1 $\mu\text{m}/\text{min}$. This kind of order is referred to as L1. PS particles appear dark and silica particles appear bright. The contrast is due to different material composition	98
4-19	SEM image of a large area with L1 ordering. This region is made of dark 250 nm PS particles arranged in every other hole and bright 250 nm silica particles filling the remaining holes. The contrast is due to different material composition. Typical bands with L1 order were 8 μm wide along the direction of withdrawal of the suspension, and tens of micrometers large, perpendicular to it	99
4-20	SEM image of a template after convective assembly of 250 nm PS particles from their 0.01-v/v% aqueous suspension. The withdrawal speed of the suspension was 46.1 $\mu\text{m}/\text{min}$ at 35°C and κ^{-1} was 250 nm. This was inferred from conductivity measurement of the solvent. Due to low concentration of PS particles in the suspension and due to high κ^{-1} , sparser pattern was stabilized by electrostatic repulsion between particles	100

4-21	SEM image of 250 nm bright silica particles and 250 nm dark PS particles arranged on a template. Silica particles were deposited on a template with PS particles arranged in a sparser pattern, shown in fig. 4-20. Silica particles were deposited from a 0.025-v/v% aqueous suspension at 50°C. The suspension was withdrawn at 46.1 $\mu\text{m}/\text{min}$.	101
4-22	SEM image of a large area with 250 nm PS particles arranged in a sparse pattern in the second layer. The underlying first layer had L1 order. PS particles were deposited from a 0.025-v/v% aqueous suspension at 23.3 $\mu\text{m}/\text{min}$ and 35°C, through convective assembly. Typical bands with L2-PS order were 5 μm wide.	102
4-23	SEM image of a region with 250 nm PS particles arranged in a sparse pattern on the second layer. The underlying, first layer had L1 order. PS particles were deposited from a 0.025-v/v% aqueous suspension at 23.3 $\mu\text{m}/\text{min}$ and 35°C, through convective assembly	103
4-24	PS particles in L2-PS in fig. 4-23, are colored in green. Dull green discs denote vacancies, whereas bright green discs denote PS particles. Here, L2-PS domain is made of three L2-PS grains. These are represented by coloring the rim of the discs differently. Discs with identically colored rims belong to the same grain	103
4-25	SEM image of a region with 250 nm PS particles arranged in a sparse pattern in the second layer. In the first layer PS particles occupy all the holes. Larger domains of PS particles with sparse ordering were observed when the underlying layer was made solely of PS particles. Here, PS particles were deposited in the second layer from a 0.025-v/v% aqueous suspension at 23.3 $\mu\text{m}/\text{min}$ and 35°C, through convective assembly	104
4-26	Variation of $\lambda_{\text{silica-band}}$ and $\delta_{\text{silica-band}}$ for silica particles after dip-coating in different suspensions of PAH	106
4-27	Variation of ϕ_{L2} after dip-coating in different suspensions of PAH . .	107

4-28	SEM image after 250 nm silica particles were deposited in the second layer, from a 0.025-v/v% aqueous suspension at 50°C and 46.1 $\mu\text{m}/\text{min}$, through convective assembly. Prior to silica deposition, the substrate was dipped in 1 mg/ml suspension of PAH for 10 minutes	107
4-29	Identical SEM image to fig. 4-28. PS particles in the second layer are colored green and silica particles in the second layer are colored red, for better visual contrast. The colored particles form a L2 domain . .	108
4-30	SEM image after 250 nm silica particles were deposited in the second layer, from a 0.025-v/v% aqueous suspension at 50°C and 46.1 $\mu\text{m}/\text{min}$, through convective assembly. Prior to silica deposition, the substrate was dipped in 3 mg/ml suspension of PAH for 5 minutes	108
4-31	Identical SEM image to fig. 4-30. PS particles in the second layer are colored green and silica particles in the second layer are colored red, for better visual contrast. The colored particles form a L2 domain . .	109
4-32	SEM image after 250 nm silica particles were deposited in the second layer, from a 0.025-v/v% aqueous suspension at 50°C and 46.1 $\mu\text{m}/\text{min}$, through convective assembly. Prior to silica deposition, the substrate was dipped in 7 mg/ml suspension of PAH for 5 minutes. Note that a negatively charged silica particle is perched on top of another particle in the first layer. This may indicate that charge reversal took place for particles in the first layer, after dipping in the 7 mg/ml suspension of PAH	110
4-33	Variation of $\lambda_{\text{silica-band}}$ and $\delta_{\text{silica-band}}$ after deposition of silica particles at different relative humidities.	111
4-34	Variation of ϕ_{L2} after deposition of silica particles at different relative humidities	112
4-35	SEM image showing a band of 250 nm silica particles arranged in a 3D non-close-packed structure. PS particles were removed from the sample by exposure to oxygen plasma.	113

4-36	SEM image of 250 nm silica particles arranged in a 3D non-close-packed structure. PS particles were removed from the original sample by exposure to oxygen plasma	114
4-37	SEM image of a cross-section of a template with 250 nm silica particles arranged in a 3D non-close-packed structure	114
5-1	Plot of the surface tension forces during convective assembly. The suspension is withdrawn at a rate v_z	118
6-1	Plot of τ across $\ln(c) - T$ landscape, for the arrangement of 140 nm particles, when $\kappa^{-1}=30$ nm	125
6-2	Plot of τ across $\ln(c) - T$ landscape, for the arrangement of 140 nm particles, when $\kappa^{-1}=100$ nm	126
6-3	Plot of τ across $\ln(c) - T$ landscape, for the arrangement of 140 nm particles, when $\kappa^{-1}=204$ nm	126
6-4	Plot of τ across $\ln(c) - T$ landscape, for the arrangement of 250 nm particles, when $\kappa^{-1}=30$ nm	127
6-5	Plot of τ across $\ln(c) - T$ landscape, for the arrangement of 250 nm particles, when $\kappa^{-1}=100$ nm	127
6-6	Plot of τ across $\ln(c) - T$ landscape, for the arrangement of 250 nm particles, when $\kappa^{-1}=204$ nm	128
6-7	Plot of τ across $\ln(c) - T$ landscape, for the arrangement of 500 nm particles, when $\kappa^{-1}=30$ nm	128
6-8	Plot of τ across $\ln(c) - T$ landscape, for the arrangement of 500 nm particles, when $\kappa^{-1}=100$ nm	129
6-9	Plot of τ across $\ln(c) - T$ landscape, for the arrangement of 500 nm particles, when $\kappa^{-1}=204$ nm	129

6-10 (a)Arrangement of 140 nm particles at $\kappa^{-1}=204$ nm, $\ln(c)=40.1$ and $T=1100$ K. (b)Pair Distribution Function (PDF) for the particles on the template, in (a), is plotted in red. For comparison, PDF for the arrangement of particles at $\kappa^{-1}=100$ nm and 30 nm are plotted in blue and green respectively. These PDF plots show that unlike at $\kappa^{-1}=204$ nm, at $\kappa^{-1}=30$ nm, all sites on the template are occupied. 131

6-11 (a)Arrangement of 140 nm particles at $\kappa^{-1}=204$ nm, $\ln(c)=40.1$ and $T=3100$ K. (b)Pair Distribution Function (PDF) for the particles on the template, in (a), is plotted in red. For comparison, PDF for the arrangement of particles at $\kappa^{-1}=100$ nm and 30 nm are plotted in blue and green respectively. These PDF plots show that unlike at $\kappa^{-1}=204$ nm, at $\kappa^{-1}=30$ nm, all sites on the template are occupied. 131

6-12 (a)Arrangement of 140 nm particles at $\kappa^{-1}=204$ nm, $\ln(c)=40.1$ and $T=5100$ K. (b)Pair Distribution Function (PDF) for the particles on the template, in (a), is plotted in red. For comparison, PDF for the arrangement of particles at $\kappa^{-1}=100$ nm and 30 nm are plotted in blue and green respectively. These PDF plots show that at $\kappa^{-1}=30$ nm all sites on the template are occupied; many domains where all sites are occupied, are also stabilized for $\kappa^{-1}=204$ nm. 132

6-13 (a)Arrangement of 140 nm particles at $\kappa^{-1}=204$ nm, $\ln(c)=40.1$ and $T=7100$ K. (b)Pair Distribution Function (PDF) for the particles on the template, in (a), is plotted in red. For comparison, PDF for the arrangement of particles at $\kappa^{-1}=100$ nm and 30 nm are plotted in blue and green respectively. These PDF plots show that at all κ^{-1} values, all sites on the template are occupied. 132

6-14 (a)Arrangement of 250 nm particles at $\kappa^{-1}=204$ nm, $\ln(c)=40.1$ and $T=1100$ K. (b)Pair Distribution Function (PDF) for the particles on the template, in (a), is plotted in red. For comparison, PDF for the arrangement of particles at $\kappa^{-1}=100$ nm and 30 nm are plotted in blue and green respectively. These PDF plots show that unlike at $\kappa^{-1}=204$ nm, at $\kappa^{-1}=30$ nm, all sites on the template are occupied. 133

6-15 (a)Arrangement of 250 nm particles at $\kappa^{-1}=204$ nm, $\ln(c)=40.1$ and $T=3100$ K. (b)Pair Distribution Function (PDF) for the particles on the template, in (a), is plotted in red. For comparison, PDF for the arrangement of particles at $\kappa^{-1}=100$ nm and 30 nm are plotted in blue and green respectively. These PDF plots show that unlike at $\kappa^{-1}=204$ nm, at $\kappa^{-1}=30$ nm, all sites on the template are occupied. 133

6-16 (a)Arrangement of 250 nm particles at $\kappa^{-1}=204$ nm, $\ln(c)=40.1$ and $T=5100$ K. (b)Pair Distribution Function (PDF) for the particles on the template, in (a), is plotted in red. For comparison, PDF for the arrangement of particles at $\kappa^{-1}=100$ nm and 30 nm are plotted in blue and green respectively. These PDF plots show that at $\kappa^{-1}=30$ nm all sites on the template are occupied; many domains where all sites are occupied, are also stabilized for $\kappa^{-1}=204$ nm. 134

6-17 (a)Arrangement of 250 nm particles at $\kappa^{-1}=204$ nm, $\ln(c)=40.1$ and $T=7100$ K. (b)Pair Distribution Function (PDF) for the particles on the template, in (a), is plotted in red. For comparison, PDF for the arrangement of particles at $\kappa^{-1}=100$ nm and 30 nm are plotted in blue and green respectively. These PDF plots show that at all κ^{-1} values, all sites on the template are occupied. 134

- 6-18 (a)Arrangement of 500 nm particles at $\kappa^{-1}=204$ nm, $ln(c)=40.1$ and $T=1100K$. (b)Pair Distribution Function (PDF) for the particles on the template, in (a), is plotted in red. For comparison, PDF for the arrangement of particles at $\kappa^{-1}=100$ nm and 30 nm are plotted in blue and green respectively. These PDF plots show that unlike at $\kappa^{-1}=204$ nm, at $\kappa^{-1}=30$ nm, all sites on the template are occupied. 135
- 6-19 (a)Arrangement of 500 nm particles at $\kappa^{-1}=204$ nm, $ln(c)=40.1$ and $T=3100K$. (b)Pair Distribution Function (PDF) for the particles on the template, in (a), is plotted in red. For comparison, PDF for the arrangement of particles at $\kappa^{-1}=100$ nm and 30 nm are plotted in blue and green respectively. These PDF plots show that unlike at $\kappa^{-1}=204$ nm, at $\kappa^{-1}=30$ nm, all sites on the template are occupied. 135
- 6-20 (a)Arrangement of 500 nm particles at $\kappa^{-1}=204$ nm, $ln(c)=40.1$ and $T=5100K$. (b)Pair Distribution Function (PDF) for the particles on the template, in (a), is plotted in red. For comparison, PDF for the arrangement of particles at $\kappa^{-1}=100$ nm and 30 nm are plotted in blue and green respectively. These PDF plots show that at $\kappa^{-1}=30$ nm all sites on the template are occupied; many domains where all sites are occupied, are also stabilized for $\kappa^{-1}=204$ nm. 136
- 6-21 (a)Arrangement of 500 nm particles at $\kappa^{-1}=204$ nm, $ln(c)=40.1$ and $T=7100K$. (b)Pair Distribution Function (PDF) for the particles on the template, in (a), is plotted in red. For comparison, PDF for the arrangement of particles at $\kappa^{-1}=100$ nm and 30 nm are plotted in blue and green respectively. These PDF plots show that at all κ^{-1} values, all sites on the template are occupied. 136

List of Tables

3.1	Variation of Debye length with increasing NaCl concentration in water	59
3.2	Variation of Triton-X 100 coverage on Polystyrene with bulk concentration of Triton- X 100, as determined by QCM	72
4.1	Variation in λ_{band} , ϕ_{sparse} , and δ_{band} at different Debye lengths and concentrations for 250 nm PS particles	87
4.2	Formation of the sparse structure at different speeds of withdrawal of the suspension	95
4.3	Summary of Dip-coating in PAH	105
4.4	Characteristics of L1-PS bands from carboxyl and sulphate functionalized PS particles	111

Chapter 1

Motivation and Layout of the Thesis

Colloidal dispersions were regarded as ideal systems to experimentally simulate molecular behavior [1, 2, 3]. Thus, the behavior of colloidal particles in suspension has been the subject of several studies [4, 5]. It is only in the last few years that researchers have come to realize the significance of colloidal crystals. These ordered aggregates of colloidal particles have shown a remarkable promise as sensors [6, 7, 8] and molecular filters [9, 10], and most notably as photonic crystals [11, 12, 13].

Colloidal self-assembly on bare substrates produces close-packed structures. As a result, templates are required to nucleate and stabilize non-close-packed structures. Recently, Santamaria et al. demonstrated that a diamond cubic complete photonic band gap (CPBG) structure is produced when polymer and silica particles are robotically placed, one by one, on a template [14]. Since this process is lengthy and expensive, methods that rely on self-assembly are favored. In the last few years, researchers have used mildly repulsive and hard-sphere potentials to make perfect close-packed crystals [15]-[19]. Others have proposed that templated assembly of ionic colloidal crystals (ICCs), in a dispersion with mildly attractive electrostatic potential, may be able to create CPBG photonic crystals [20, 21].

In this thesis, novel self-assembly methods are used to order strongly charged particles. These methods utilize electrostatic interaction to nucleate newer structures. It

is shown that the motif of these structures can serve as a starting point for generating the complex periodic architectures, which are needed for integrated photonic crystal applications.

The objective of this thesis is twofold. The first objective is to outline methods that can be used to create stable aggregates from strongly charged particles, whether they are similarly or oppositely charged. The second objective is to utilize these methods to create binary and non-close-packed structures through directed self-assembly.

It is shown that when particles are oppositely charged, a steric force is necessary to order them into stable structures [22]. Binary colloidal crystals are nucleated and show greater stability compared to their like-charged counterparts. Therefore, they are better candidates for making low-volume and non-close-packed architectures. Findings from this study are contrary to published reports, which state that only mild electrostatic attraction can nucleate stable and ordered structures [23]. It is also shown that like-charged particles order in a non-close-packed arrangement on a close-packed substrate of oppositely charged particles. Clearly, greater attraction between particles leads to a more stable structure. Stability of these structures is verified through theoretical calculations.

When particles are similarly charged, it is shown that a suitable 2D template can be used to nucleate non-close-packed structures [24]. These structures are sparsely ordered*. In other words, the particles occupy only a few of the sites available to them. Yet, they form an ordered structure. Experiments and computational Monte Carlo simulations show that a high Debye length in the solvent and a low concentration of particles in the suspension are necessary requirements for nucleating sparse structures. If the Debye length is small, thermal motion would prevent the nucleation of sparse domains. It is shown that sparse arrangement of particles can be exploited to make a non-close-packed two-layered structure.

*In this thesis, sparse ordering refers to an arrangement of particles, such that they are ordered with a (110) orientation (with respect to the underlying substrate) on a template with holes arranged in (100) orientation. Additionally, only 50% of the holes on the template are occupied.

1.1 Layout of the Thesis

Chapter 2 provides a background of colloidal forces. Later in the chapter, a brief literature survey of colloidal self-assembly is presented. Thereafter, a few self-assembly and directed self-assembly methods, relevant to this thesis, are discussed.

Chapter 3 discusses a simple and rapid layer-by-layer method to order strongly and oppositely charged particles. By using a spin-coating method, stable LS_2 and LS_6 structures are nucleated. Later in the chapter, a dip-coating method is used to make two layers of a non-close-packed structure. Theoretical calculations show that, using oppositely charged particles creates more stable structures compared to similarly charged particles. At the end of this chapter, the role of hydrophobic interaction during self-assembly of charged particles on charged substrates, is discussed.

Chapter 4 discusses the formation of a sparse layer of particles on a template, with holes arranged in (100) symmetry. It is shown that the sparse order depends on the Debye length of the solvent and concentration of particles in the suspension. Subsequently, a 2D heterostructure is formed by filling the unoccupied sites in the sparse layer. Thereafter, the conditions and experiments for the formation of a two-layer heterostructure are discussed. It is shown that the removal of one type of particle from this structure, leads to a two-layer structure with non-close-packed arrangement of particles.

Chapter 5 reviews the mechanism behind stick and slip. Recently, a few methods have been used to make colloidal crystals; in these methods there was no stick and slip of the meniscus. In this chapter, the feasibility of these methods, such as Langmuir-Blodgett (LB), to assemble a sparse pattern of particles, is discussed.

Chapter 6 discusses the results from Monte Carlo simulations. Conditions for the arrangement of colloidal particles into sparse domains are discussed. The results from these simulations show that the formation of sparse domains requires a large Debye length in the solvent and a low concentration of particles in the suspension. Further, conditions for the formation of sparser[†] domains are discussed.

[†]In this thesis, sparser ordering refers to an arrangement of particles, such that they are ordered with a (111) orientation (with respect to the underlying substrate) on a template with holes arranged

In Chapter 7, general conclusions and the scope of this thesis are discussed. In the end, future directions for this work are outlined.

in (100) orientation. Additionally, only 25% of the holes on the template are occupied.

Chapter 2

Colloidal Forces and Methods of Self-Assembly

Colloidal science has its roots in nineteenth-century discoveries concerning the behavior of minute particles suspended in a solvent. These systems are called colloidal dispersions. A distinguishing feature of these dispersions is that the area of contact between the dispersed particles, and the solvent is relatively large. The name “colloid” itself, comes from a study of colloidal dispersions by Thomas Graham in 1860. While looking at the passage of various solute dispersions through a dialysis membrane, one kind of solute could not pass through. This solute (natural gum) led Graham to coin the term “colloid” (after kolla, meaning natural gum). Presently, colloidal dispersions are used all around us. Some notable examples are milk, paints, etc.

Colloidal dispersions occur in many forms. The most widely used and studied are dispersions of solids in liquids. The majority of conclusions from these studies are applicable to dispersions of liquids in liquids (emulsions) and gases in liquids (foams). However, those conclusions cannot be extended to dispersions of solids or liquids in gases (aerosols). This thesis will be focused on dispersions of solids in liquids.

Particle size and shape are of considerable importance in setting the properties of a colloidal system. A colloidal particle is a macroscopic entity, composed of a number of atoms or molecules. The size of a colloidal particle ranges from a few nanometers

to hundreds of micrometers. However, the solute particles should be distinguishable from the solvent molecules. As a result, the colloidal particles should be no smaller than a nanometer.

Since the latter part of the 20th century, production of near-monodisperse dispersions has enabled many fundamental studies on colloidal particles. These particles are uniform in size, shape, composition and surface properties. Spherical colloids in particular, have been the most successful, best-established examples of monodisperse systems. Elaborate schemes exist to synthesize spherical colloids from different materials. Driven by the minimization of interfacial energy, the spherical shape may represent the simplest form into which a colloidal particle can develop for isotropic surface energies. Experimental studies on spherical colloids have greatly enriched our understanding of their light-scattering properties, interactions between colloidal particles and their hydrodynamic properties.

In addition, spherical colloids represent ideal building blocks that can be readily assembled into ordered structures. These ordered lattices are referred to as colloidal crystals. Colloidal crystals allow for the observation of interesting functionality from long-range ordered structures and not just the constituent particles. For example, the beautiful colors of opal are the result of light diffraction from close-packed crystals of silica colloids, which are themselves colorless. More recently, calculations have shown that some colloidal crystal structures have a complete photonic band gap. This has generated a lot of excitement and heralded newer ways of controlling crystal growth orientation. As a result, newer ways of assembling colloidal crystals have been proposed and almost all of these rely on controlling colloidal interaction. More detailed discussions on these topics can be found elsewhere [25]-[32].

2.1 Brownian Motion

For very dilute suspensions, any interparticle interactions can be ignored. When these dispersions are viewed under a microscope, the particles are seen to move in a random motion. This is called Brownian motion. Brownian motion of particles

originates due to an uneven bombardment of the particles by solvent molecules. At each step, the particles move in the direction of lower molecular densities. Due to the random motion of water molecules, the directional motion of colloidal particles fluctuates in a random manner and their velocities are governed by hydrodynamic drag. For a spherical particle, the Stokes drag factor, s_v , is a function of the radius of the sphere, a , and the viscosity of the fluid, η , as shown in eq. 2.1:

$$s_v = 6\pi\eta a. \quad (2.1)$$

The root mean squared (rms) velocity depends on the rms distance moved, x_{rms} , in a time interval t , as:

$$v_{rms} = x_{rms}/t. \quad (2.2)$$

The work done to move the particle is the hydrodynamic force, $f_v = v_{rms}s_v$, times the distance x_{rms} . This is the same as the thermal energy for the particle, $k_B T$, where k_B is the Boltzmann's constant and T is the absolute temperature. Two important parameters can be derived from the above equations. The first is the diffusion coefficient, D , shown in eq. 2.3:

$$D = \frac{x^2}{t} = \frac{k_B T}{6\pi\eta a}. \quad (2.3)$$

The above equation, eq. 2.3, is the Stokes-Einstein equation. The second parameter is t_c : the characteristic time it takes for a particle to diffuse a distance equal to its radius, and is given by eq. 2.4:

$$t_c = \frac{6\pi\eta a^3}{k_B T}. \quad (2.4)$$

The above equation is the Einstein-Smoluchowski equation. For an isolated $1 \mu\text{m}$ particle at 20°C in water, the characteristic time is 0.5 seconds. For concentrated colloidal dispersions, the movement of particles is influenced by neighboring particles and interparticle forces (electrostatic, hydrodynamic or van der Waals).

2.2 Interactions between Colloidal Particles

2.2.1 Van der Waals Interaction

The van der Waals (vdW) interaction is the term used to describe the forces resulting from interactions between dipoles, quadrupoles and multipoles. There are several interactions that can occur, which are electrodynamic in origin; traditionally, these are separated into three distinct forms. These are dipole–dipole interaction (Keesom interaction) [33, 34, 35], dipole–induced dipole interaction (Debye interaction) [36, 37] and induced dipole–induced dipole interaction (London interaction) [38, 39]. More details about these forces can be obtained from an excellent review by French [40]. In general, colloidal particles do not have permanent dipoles. In that case, London forces dominate the total van der Waals interaction and are briefly discussed below.

London forces describe the interaction that results between non-polar substances. For colloids, the London interaction between two particles is assumed to be the sum of the pairwise interactions of their atoms. The interaction energy can be written as follows [39]:

$$U = -\frac{C_L}{r^6}. \quad (2.5)$$

The London constant, C_L , is proportional to the ionization energy of the outer electrons, $h\nu_1$, and the polarizability α :

$$C_L \propto h\nu_1\alpha^2. \quad (2.6)$$

For two dissimilar molecules, this becomes:

$$C_L \propto h\alpha_1\alpha_2 \frac{\nu_{11}\nu_{12}}{\nu_{11} + \nu_{12}}. \quad (2.7)$$

In 1937, Hamaker published an article where he investigated the properties of van der Waals interaction between large bodies [41]. The analysis in this paper was far-reaching and showed that the strength of vdW interaction between large bodies is distinct from vdW interaction between molecules, which had been considered

previously. Hamaker used pairwise summation approximation to calculate these interactions. The idea in this approximation was that infinitesimal parts of large bodies interact with one another according to the London equation. The total strength of the vdW interaction between two bodies integrates over all such infinitesimal interaction terms. De Boer had shown previously [42] that the vdW interaction between large planar slabs varies as the inverse of the square of separation distance between them. As a result, vdW interaction came to be viewed as a longer-range interaction than previously thought.

Of special importance in colloidal science is the interaction between two spherical particles, 1 and 3, in a medium, 2. This is given by eq. 2.8 [43]:

$$U_{vdW} = -\frac{A_{123}}{6} \left[\frac{2a_1a_3}{r^2 - (a_1 + a_3)^2} + \frac{2a_1a_3}{r^2 - (a_1 - a_3)^2} + \ln \left[\frac{r^2 - (a_1 + a_3)^2}{r^2 - (a_1 - a_3)^2} \right] \right], \quad (2.8)$$

where r is the separation between particles with radii a_1 and a_3 . The influence of the intervening medium, 2, and material properties of the bodies, 1 and 3, is captured by the Hamaker constant A_{123} . From eq. 2.8, the interaction is divergent at contact. In order to avoid this, a cut-off radius equal to the diameter of the solvent molecule is used as the limiting distance for vdW interaction [44].

The Hamaker constant, A_{123} , is of central importance in the analysis of vdW forces between colloids. Although it is difficult to calculate in most instances, approximate values of the Hamaker constant for materials in vacuum are 100–300 zJ for metals, 10–30 zJ for ionic materials and 3 zJ for hydrocarbons. In a solvent, these values are greatly reduced due to screening of the interaction.

A_{123} can be approximated from the Hamaker constant of materials in vacuum, as shown in eq. 2.9 [28]:

$$A_{123} = (\sqrt{A_{11}} - \sqrt{A_{22}})(\sqrt{A_{33}} - \sqrt{A_{22}}). \quad (2.9)$$

Early theories relied on pairwise additivity to calculate A_{123} . This ignores the influence that neighboring atoms or molecules have on the interaction between any two atoms. This interaction was treated exactly by Lifschitz [45]. According to his theory,

the Hamaker constant for the interaction of two media 1 and 3, across the medium 2, is given by eq. 2.10 [28]:

$$A_{123} \approx \frac{3}{4} k_B T \left(\frac{\epsilon_1 - \epsilon_2}{\epsilon_1 + \epsilon_2} \right) \left(\frac{\epsilon_3 - \epsilon_2}{\epsilon_3 + \epsilon_2} \right) + \frac{3h}{4\pi} \int_{\nu}^{\infty} \left(\frac{\epsilon_1(i\nu) - \epsilon_2(i\nu)}{\epsilon_1(i\nu) + \epsilon_2(i\nu)} \right) \left(\frac{\epsilon_3(i\nu) - \epsilon_2(i\nu)}{\epsilon_1(i\nu) + \epsilon_2(i\nu)} \right) d\nu, \quad (2.10)$$

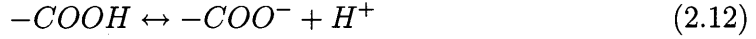
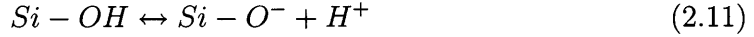
where ϵ_1 , ϵ_2 and ϵ_3 are the static dielectric constants of the three media and $\epsilon(i\nu)$ are the values of ϵ at imaginary frequencies. The first term gives the zero frequency energy of van der Waals interaction and includes the Keesom and the Debye interaction. The second term includes the contribution from London dispersion interaction. Two important points should be noted about eq. 2.10: (i) first, the vdW force between any two bodies in vacuum is attractive; (ii) second, vdW force between identical bodies across all media is attractive, but may be attractive or repulsive for dissimilar bodies in a medium.

2.2.2 Electrostatic Interaction

If vdW forces were to act alone, one might expect all suspended particles to coagulate. Normally, this does not happen because the suspended particles are stabilized by electrostatic repulsion or steric repulsion, and do not coalesce. Electrostatic interaction is one of the most important stabilizing forces for charged colloidal dispersions. Steric interaction is another, and is discussed later.

Interfaces between colloidal particles and ionic solutions, like water, almost always acquire charge. This alters the concentration and spatial variation of free ions in solution. Several mechanisms have been identified for the charging of colloidal particles [30]. Two relevant mechanisms for the purpose of this thesis are:

(i) The ionization of surface groups: for instance, ionization of surface hydroxyl groups, shown in eq. 2.11, leads to negatively charged silica particles, whereas ionization of carboxyl groups (or sulfonic acid groups), shown in eq. 2.12, leads to negatively charged latex particles. Ionization of amine and amidine groups leads to positively charged latex particles.



(ii) Adsorption or covalent bonding of charged entities from the suspension, onto an uncharged surface. For instance, adsorption of amphiphilic polyelectrolytes charges hydrophobic particles in water.

Poisson-Boltzmann Equation

Helmholtz gave the earliest treatment to describe the electrostatics related to a charged particle in solution. He proposed a simple model, wherein a uniformly charged sphere is surrounded by ions of opposite polarity, the counter-ions, in a uniform layer. The counter-ions were assumed to be point charges. Later, a more complete treatment of this was offered, wherein the finite size of the counter-ions and the diffuse nature of the counter-ion distribution were taken into consideration [46]. The counter-ions (that include particle counter-ions, ions from dissociated salts and ions from self-dissociated solvent molecules) form an oppositely charged atmosphere in rapid thermal motion close to the surface. This is called the diffuse double layer.

A model for the distribution of counter-ions, ρ_ψ , depends on the electrostatic potential, ψ , and is given by eq. 2.13 [28]:

$$\rho_\psi = \rho_i \exp\left(\frac{-z_i e \psi}{k_B T}\right), \quad (2.13)$$

where

$$\rho_i = \sum_i n_i z_i e. \quad (2.14)$$

Together with the Poisson equation, eq. 2.15:

$$-\epsilon \epsilon_0 \nabla^2 \psi = \rho_\psi, \quad (2.15)$$

this leads to the Poisson-Boltzmann equation (PBE), eq. 2.16:

$$\nabla^2\psi = -\sum_i \frac{z_i n_i e}{\epsilon_r \epsilon_0} \exp\left(\frac{-z_i e \psi}{k_B T}\right), \quad (2.16)$$

where n_i is the number density of ions i of valence z_i and e is the electronic charge. PBE is one of the most important equations in colloidal science, and is the basis for understanding the electrostatic interaction between colloidal particles.

Solutions of the Poisson-Boltzmann Equation

PBE is a second-order non-linear differential equation. It can be simplified by making the following assumptions:

(i) Although there may be multiple salt species present in the solution, the ionic concentration is dependent upon the majority salt component.

(ii) While a colloidal solution does not have an equal number of positive and negative ions, the number of counter-ions from colloidal particles is small and can be safely ignored. Moreover, the majority of salts are symmetric: that is, they have the same magnitude for positive and negative ions.

With the above assumptions, the summation in eq. 2.16 reduces to a sum of two exponentials. The resulting equation is shown in eq. 2.17:

$$\nabla^2\psi = 2\frac{zne}{\epsilon_r \epsilon_0} \sinh\left(\frac{ze\psi}{k_B T}\right). \quad (2.17)$$

The hyperbolic sine term in eq. 2.17 can be expanded as shown in eq. 2.18:

$$\sinh(x) = x + \frac{x^3}{3!} + \frac{x^5}{5!} + \dots \quad (2.18)$$

Eq. 2.17 can be simplified further if the electrical energy $|ze\psi|$ is small compared to the thermal energy $k_B T$. In this case the first term in the \sinh series is much larger than the second term. As a result, all higher order terms can be ignored. With these assumptions, eq. 2.17 can be linearized. The resulting equation, eq. 2.19, is known

as the Debye-Hückel approximation:

$$\nabla^2\psi = \left[\frac{z^2 e^2 n}{\epsilon_0 \epsilon_r k_B T}\right]\psi = \kappa^2\psi, \quad (2.19)$$

where

$$\kappa = \left[\frac{e^2 n z^2}{\epsilon k_B T}\right]^{1/2}. \quad (2.20)$$

For a system with surface charge, eq. 2.19 has an additional term for the surface charge density, $\rho_s(x, y, z)$. Eq. 2.21 is the modified equation [28]:

$$\nabla^2\psi = \kappa^2\psi + \frac{\rho_s(x, y, z)}{\epsilon_0 \epsilon_r}. \quad (2.21)$$

The variable κ is known as the Debye-Hückel parameter and plays a central role in describing the strength of electrostatic interaction in colloidal systems. The extent of the double layer is measured by κ^{-1} , also known as Debye length, and ranges between 1 nm to 250 nm for most aqueous systems. At 25 °C in water, κ^{-1} is given by eq. 2.22:

$$\frac{1}{\kappa} = \left(\frac{\epsilon_0 \epsilon_r R T}{2000 F^2}\right)^{1/2} \frac{1}{\sqrt{I}} [m] \quad (2.22)$$

$$= 0.304 \frac{1}{\sqrt{I}} [nm], \quad (2.23)$$

where I is the ionicity and F is Faraday's constant. The linearized PBE, eq. 2.19, is valid for surface potentials where $\psi_s < 25$ mV. For a colloidal particle with $\psi_s > 25$ mV, the non-linearized PBE, eq. 2.17, should be numerically solved, since the linearized PBE is no longer valid at close proximity to the particle. However, for a many-particle system where $\psi_s > 25$ mV, this becomes computationally prohibitive. As a result, although solution of the linearized PBE may be less accurate, it continues to be widely used in order to obtain behavioral trends and to identify regimes where more detailed models may be required. Thus, larger phase-space can be analyzed by compromising a bit on the accuracy of the solution.

Boundary Conditions and Interparticle Potential

Linearized PBE, eq. 2.21, is a second order equation. Therefore any mechanism to obtain a solution requires two boundary conditions. One boundary condition is that the gradient of ψ vanishes as $r \rightarrow \infty$:

$$\nabla\psi \cdot \vec{r}/|\vec{r}| = 0 \quad \text{as} \quad r \rightarrow \infty. \quad (2.24)$$

The limitations for the second boundary condition are: constant surface charge or constant surface potential. It is instructive to consider the following scenarios to infer the correct boundary condition. For an isolated particle, both boundary conditions lead to an identical solution. The choice is more subtle when particles start to interact. For like-charged particles with a constant charge boundary condition, the electrostatic potential at the point of contact of particles would be close to twice the surface potential of an isolated particle. On the other hand, for like-charged particles with a constant potential boundary condition, close approach leads to an increase of surface charge. Thus, although the results in these two regimes may be different for like-charged particles, the physical behavior is similar: like-charged particles repel each other. For oppositely charged particles with a constant potential boundary condition, the surface charge would be infinity at the point of contact of particles. Thus, oppositely charged particles would be inseparable on contact. In reality, this is an incorrect assumption since each particle has limited charging sites, and therefore the surface charge approaches a maximum as the particle separation becomes small. As a result, one usually assumes a constant charge boundary condition for analyzing colloidal interactions.

Choosing correct interparticle potential is also critical. There are two principal potentials: the screened electrostatic Yukawa-type potential [47, 48] and the Ohshima potential [49]. The Yukawa-type potential is valid at low ionic strengths. An important assumption for this potential is that the particle interior has properties (dielectric constant and ionic strength) similar to the bulk solvent. Assuming that interactions with neighboring particles can be neglected, the potentials can be superimposed. On

the other hand, the Ohshima potential assumes a Yukawa-type potential as the first-order term and corrects for the ionic strength and dielectric constant of the particle core by adding a series of converging infinite sums. However, in making these corrections, an additional assumption is made that two interacting particles are only surrounded by the solvent. Thus, the Ohshima potential is not useful for low ionic strength dispersions.

The interaction energy in the case of the Yukawa-type potential is given by a product of the point-charge representation of one particle and the potential field of other particles. The effective point-charge for a particle with radius, a , and surface potential, ψ_s , is given by eq. 2.25 [50, 51]:

$$q_{point} = 4\pi\epsilon a\psi_s \exp(\kappa). \quad (2.25)$$

This is the result of superposition of the potential field of other particles and is known as the linear superposition approximation (LSA). The total energy of interaction between particles 1 and 2, with radii a_1 and a_2 , is given by eq. 2.26:

$$U_{12} = q_1 q_2 \frac{\exp(-\kappa r)}{r} \quad (2.26)$$

$$= [4\pi\epsilon a_1 \psi_{s,1} \exp(\kappa a_1)] [4\pi\epsilon a_2 \psi_{s,2} \exp(\kappa a_2)] \frac{\exp(-\kappa r)}{(4\pi\epsilon)} \quad (2.27)$$

$$= 4\pi\epsilon a_1 a_2 \psi_{s,1} \psi_{s,2} \exp(\kappa(a_1 + a_2)) \frac{\exp(-\kappa r)}{r}. \quad (2.28)$$

The interaction potential in eq. 2.28 is called a Yukawa-type potential, or a screened electrostatic potential [52]-[67]. It is widely used in this thesis to model the electrostatic interaction between particles.

Zeta Potential

Information regarding the interaction between particles depends on the electrical double layer around them. Determining the zeta potential [26], ζ , for a colloidal particle is a useful way of obtaining information about the structure of the double

layer. Electrokinetic processes are usually used to determine ζ . Electrokinetics refers to processes in which the boundary layer between one charged phase and another is forced to undergo some sort of shearing process. During this process the charge associated with the particle's compact layer will move in one direction, and that associated with the diffuse layer in the liquid, will move in the opposite direction. Zeta potential is an electrokinetic potential, and is defined as the equilibrium potential at the "surface of shear," where the velocity of liquid is zero.

Many electrokinetic processes can be used to determine ζ , although electrophoresis is most widely used. When an electric field is applied to a particle, there is an external force that moves the particle with a velocity that is proportional to ζ . Using a force balance, eq. 2.29, one can obtain information about ζ by measuring the terminal velocity of the particle, v , which is related to the electrophoretic mobility, μ , and the applied electric field, E , by eq. 2.30:

$$F = -\beta v + Eq = 0 \quad (2.29)$$

and

$$v = \frac{Eq}{\beta} = E\mu, \quad (2.30)$$

where $\beta = 1/s_v$.

Electrophoretic mobility for a particle can be related to ζ through numerous methods. Two most common models are: the Hückel model [68] (for $\kappa a \ll 1$) and the Smoluchowski model [69] (for $\kappa a \gg 1$), where a is the radius of the particle.

The Hückel regime is applicable when particles have a very thick double layer. In this case, the electric field lines are unaffected by the particle, and the electrical force on the particle is balanced by the viscous drag of the solvent. Thus:

$$\mu = \frac{v}{E} = \frac{4\pi\epsilon\zeta a}{6\pi\eta a} = \frac{2\epsilon\zeta}{3\eta}. \quad (2.31)$$

The Smoluchowski regime is applicable when particles have a thin double layer. In this case, the viscous force on the particle, on a volume element with surface area A , is balanced by the electrical force. The viscous term is derived from the Stokes

equation and the electrostatic term is obtained from the Poisson equation. Thus, one has:

$$F = \eta A \frac{d^2 v}{dx^2} + EA\epsilon \frac{d^2 \psi}{dx^2}. \quad (2.32)$$

For the first integration, eq. 2.32 can be simplified by assuming that only velocity, v , and electrical potential, ψ , vary. As a result, eq. 2.32 becomes eq. 2.33:

$$\eta \frac{dv}{dx} = -E\epsilon \frac{d\psi}{dx} + C \quad (2.33)$$

After integration of eq. 2.33, two boundary conditions are required in order to obtain ζ . These are: (i) electrical potential approaching zero, very far from the particle and (ii) the velocity equal to zero at the surface of shear. With these, the electrophoretic mobility is related to the zeta potential by eq. 2.34:

$$\mu = \frac{\epsilon \zeta}{\eta}. \quad (2.34)$$

For most colloidal systems, it is easier to arrange for $\kappa a > 1$ than $\kappa a < 1$. Therefore, the Smoluchowski regime is more appropriate for colloidal systems than the Hückel regime.

2.2.3 Steric Interaction

In many colloidal systems, one adds non-ionic materials that adsorb on the surface of the particles and prevent coagulation. In order to stabilize a colloidal system, these molecules should not just adsorb onto the surface of particles, but also extend into the solvent. The purpose of this morphology is to prevent particles from coming in such close proximity, that aggregation may result. This is known as steric stabilization while the interaction of polymer sheets as particles approach each other is called steric interaction [31], [70]-[87]. The most notable steric stabilizers are non-ionic block copolymers (BCP). One end of the BCP, usually lyophobic, adsorbs onto the surface of the particle, whereas the other end, usually lyophilic, extends into the

solvent. Simple homopolymers are rarely used for this purpose, as they need to be chemically grafted into the particle surface, if they are lyophilic. On the other hand, if they are lyophobic, they would form a dense layer on the particle surface and will be ineffective as stabilizers. Simple surfactant molecules also serve as good steric stabilizers.

Most models that analyze steric interaction have two regimes. In the first regime, when two sterically stabilized particles approach, the outermost parts of the surfactants start to mix. This results in increased enthalpy, as molecules prefer to be in the solvent. This is called the osmotic regime, as the osmotic pressure of the solvent, in the overlap zone, will be lower than in the bulk solvent. This leads to a driving force for spontaneous flow of the solvent into the overlap zone, which pushes the particles apart.

The second regime is when the separation between particles is less than the length of one layer of surfactant. In this regime, the polymers (or surfactants) are compressed. As a result, there are fewer possible configurations available for each molecule. This leads to a reduction in entropy.

In order to analyze steric interaction, three pieces of information are required. These are (i) the coverage of the polymer (in other words, the amount of polymer adsorbed on a unit area of the particle surface); (ii) the thickness of the adsorbed layer, once it extends into the solvent, and (iii) the profile of the outer part of the layer.

2.2.4 Hydrophobic Interaction

Water molecules are known to form an extensive network of hydrogen bonds (H-bonds) with one another. When a non-polar substance is placed in water, water molecules can reorient themselves around it without much loss of the hydrogen bonding. Reorientation is highly unfavorable entropically, as the molecules have fewer available orientations. This is the reason why hydrocarbons are insoluble in water. This effect on the H-bonding of water in the presence of non-polar substances, is called the “hydrophobic effect.” Closely tied to this is the hydrophobic interaction

[88]-[94].

For some time in the colloid community, it has been well known that hydrophobic particles placed in water attract each other over a distance of 10–30 nm, with forces that are 10–100 times stronger than vdW force. However, no conclusive evidence exists about the origins of this force. First measurements of the hydrophobic force were completed 27 years ago [92]. One source of confusion about the origin of this force is the existence of two different force regimes. It has been suggested that the measured hydrophobic force between particles is a combination of a short-range (< 10 nm) truly hydrophobic force (that originates from the reorientation of water molecules), and a long-range force (> 10 nm) due to a mechanism only indirectly related to the hydrophobicity of the surfaces. Overcoming hydrophobic interaction, either between particles or between a particle and a surface, is crucial in obtaining higher mobilities of hydrophobic colloidal particles over surfaces. As will be shown later (section 3.6), higher mobilities of colloidal particles are almost always required for perfect 3D colloidal assembly.

2.3 Stability of Colloidal Dispersions: DLVO Theory

The stability of colloidal dispersions is dependent upon interactions that occur between particles and the solvent, as well as among particles. Collisions between particles that are suspended in a solvent are inevitable. If the particles are large, these can be due to Brownian motion, agitation and flow, hydrodynamics or sedimentation. As a result of these collisions, if the particles rebound off one another, the dispersion is considered stable. On the other hand, if the particles coagulate as a result of collisions the dispersion is considered unstable.

The stability of monodisperse spherical colloids is often described by the “Derjaguin [95], Landau, Verwey and Overbeek [96]” (DLVO) theory. In this theory, the stability of the colloidal dispersion is interpreted as a change in energy, resulting from

the effects of colloidal forces, as two particles approach each other. The total energy is given by eq. 2.35:

$$U_{DLVO} = U_{electrostatic} + U_{vdW}. \quad (2.35)$$

For most aqueous dispersions of monodisperse particles, at an interparticle separation of 100 nm or more, vdW and electrostatic interactions have no effect on particles. When the particles approach one another, there is an increase in the electrostatic as well as vdW interaction. As the vdW force increases faster than the electrostatic force, there is a slight domination of the vdW force resulting in a weak secondary minimum. As the interparticle separation decreases further, the repulsive electrostatic interaction leads to a barrier that prevents particles from coming closer. This occurs until a critical distance is reached, at which the vdW force dominates the electrostatic force, resulting in strong irreversible coagulation. The behavior of particles on close approach is also dictated by their kinetic energy. If the kinetic energy of colliding particles is large enough to surmount the barrier, coagulation in the primary minimum will result. If the particles do not have enough kinetic energy, then stable weak particle associations result in the secondary minimum. The depth of the secondary minimum depends on the Hamaker constant and particle characteristics such as surface charge density, particle radius, etc.

2.4 Self-assembly of Colloids

Self-assembly is defined as the spontaneous organization of two or more components into larger aggregates using covalent or non-covalent bonds. It is a bottom-up approach that relies on the cooperative interactions of small components. The components assemble spontaneously to produce larger structures in two or three dimensions [97].

This section describes two types of self-assembly of colloidal particles: (i) non-templated self-assembly, where the individual particles interact to produce a larger structure without the influence of external forces or spatial constraints and (ii) templated self-assembly, where the individual particles interact with each other and an

external force or a spatial constraint to produce a larger structure. More detailed discussion on other aspects of self-assembly can be obtained elsewhere [98].

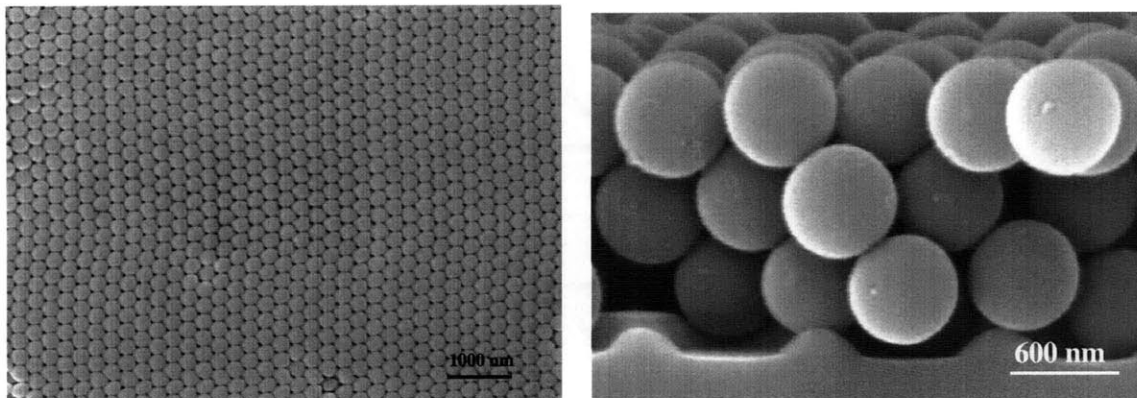


Figure 2-1: SEM image of the top view and cross-section of a colloidal crystal of polystyrene particles. The particles assemble in a face centered cubic (f.c.c.) structure with (111) orientation relative to the substrate.

In a dispersion of charged monodisperse particles with radius R , three-dimensional organization of particles into close-packed structures, such as face centered cubic (f.c.c.), takes place at low κR . More complexity can be added by using a binary system—in other words, a dispersion with two types of particles. A beautiful example of this phenomenon is the formation of Ionic colloidal crystals (ICCs) [23], [99, 100, 101]. ICCs are crystals that form in a dispersion with two particle types, such that the particles are oppositely charged. They are formed at large Debye lengths (>100 nm). This concept was proposed by Dr. Garry Maskaly [101] and experimentally demonstrated by Leunissen et al. [23]. Since these structures are formed in the solvent, solvent behavior plays a central role in their formation. As a result, ICCs can be easily destroyed on exposure to atmosphere (this leads to an increase in κR) or vibrations. Thus, the majority of methods are based on obtaining colloidal crystals without the solvent (made solely of colloidal particles). These structures are known as colloidal crystals.

The easiest way to obtain a colloidal crystal is by drying a dispersion of monodisperse colloids. As the solvent evaporates, capillary forces pack the particles into a close-packed structure [102]. A scanning electron microscope (SEM) image of this

structure is shown in fig. 2-1. Amid a self-assembly process, there are only a few parameters that can be controlled to influence the final structure. Chief among these are the concentration of the dispersion, Debye length and density of the solvent.

If there were no interactions between particles in a dispersion, on collision they would behave like billiard balls. This type of interaction is called a hard-sphere interaction [103]. However, if the particles are charged, they interact mainly through electrostatic and vdW interactions. Hence, they behave as soft spheres because their “presence” is felt by other spheres in the suspension. Hard-sphere suspensions act like fluids at low volume fraction of particles, ϕ , but crystallize into a close-packed structure when $\phi > 0.55$. On the other hand, suspensions of charged particles form close-packed f.c.c. with (111) orientation (relative to the substrate at $\phi > 0.10$ [104]. By lowering ϕ further, one can obtain a structure with body centered cubic (b.c.c.) packing. Detailed studies have been done on the phase behavior of colloids and can be explained by a pure Yukawa or a hard-sphere plus Yukawa-type potential.

In order to assemble more complex structures with different orientations, newer periodic potentials should be created. These potentials need to be anisotropic so that they break the isotropic symmetry of the colloidal interactions that results in f.c.c. crystals with (111) orientation. Such potentials have been created by applying external electric or optical fields and by manipulating the interaction potentials. Crystal orientation can also be controlled by using a patterned surface. Periodic one- or two-dimensional height profiles impose uniformly varying potentials on the colloidal spheres, during their assembly. Van Blaaderen et al. [105] were among the first to explore this idea. In the following subsections, processes used for self-assembly of colloids are discussed.

2.4.1 Methods of Self-assembly

Colloidal assembly can be induced by gravitational [106, 107, 108], electric [109]-[112] and magnetic fields [113, 114]. Although sedimentation is conceptually easy to understand, precise control of parameters, such as size and density of the particles, is needed to obtain a large single crystal. Particles will only settle, in times that are

short enough to be observed, if their size and density are large enough. Controlled sedimentation of particles in a gravitational field leads to a f.c.c. crystal. Unfortunately, the process of sedimentation is rather slow, and successful fabrication of a crystal can take weeks. The sedimentation can be expedited through centrifugation or filtration [115]. Although these processes are faster, the quality of the crystals shows negligible improvement.

Another disadvantage of the gravity method is that the thickness of the colloidal crystal cannot be controlled during sedimentation. In comparison, vertical deposition techniques [116]-[122] are ideal for controlling the thickness of the colloidal crystal. During vertical deposition, a substrate is held vertically in a beaker that has a colloidal dispersion. Colloids assemble on the substrate either when the substrate is pulled out slowly, or when the suspension is evaporated or pumped out slowly. Convective assembly is one of the most widely used vertical deposition method [117]. Convective assembly has often been used to make 2D colloidal crystals (or, in other words, colloidal monolayers). During convective assembly, crystallization is initiated in the solvent meniscus by attractive capillary forces between the particles at the drying front. These capillary forces lead to particle aggregation. A schematic showing the shape of a meniscus and arrangement of particles on the substrate is shown in fig. 2-2.

A balance between convection and capillary forces is essential for the formation of a uniform monolayer. A few recent reports [2, 21] use one or another form of vertical deposition to obtain a particle monolayer. The formation of two-layer binary colloidal crystal was also first reported using vertical deposition [123]. For this process, a close-packed layer of large particles is first formed through convective assembly. In the second step, depending on the concentration of smaller particles in the dispersion, some or all of the interstices in the first layer are filled. In order to have precise control of thickness, domain size and ordering in the crystal, a number of parameters need to be carefully controlled simultaneously. These include the choice of substrate material, tilt angle of the substrate with respect to the liquid-air interface, solvent, ambient temperature, relative humidity, concentration of colloids and evaporation

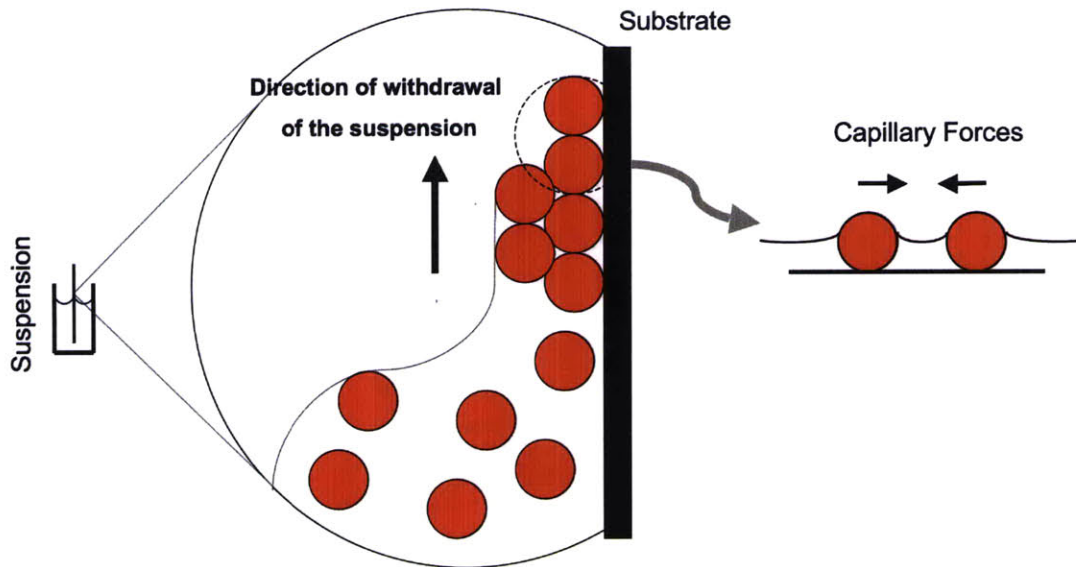


Figure 2-2: Schematic of a convective assembly process.

rate. Fabrication of large photonic devices demands large ordered domains. As shown by Xia et al. [124], using physical confinement of colloidal particles leads to colloidal crystals, with different orientation and larger ordered domains, compared to crystals created on bare substrates.

2.4.2 Directed Self-assembly

Using bare templates makes it difficult to control the orientation of colloidal crystals. Templated assembly allows for the fabrication of crystals with predefined orientation. In-depth discussion of the progress in templated assembly of colloids is available elsewhere [125]-[129].

Templates can be created by physical patterning [130]-[133] (known as hard lithography) or by chemical patterning [134]-[138]. Chemical patterning methods, like soft lithography and nanoimprint lithography, are widely used to print and attach molecules on the surface of a substrate. The topological pattern of the stamp determines the chemical pattern on the substrate. Colloids can be assembled on these chemically patterned regions of the template by vertical deposition methods. Another

widely used method is dip-coating. In dip-coating, chemically patterned substrates are dipped, held and then withdrawn from a colloidal dispersion [139]-[144]. Chemical patterns can lead to either positive or negative patterns of particles. In positive patterns, particles assemble only in regions that are chemically stamped, whereas in negative patterns they assemble only in regions without the chemical stamp. Colloidal assembly on chemically patterned templates occurs because of a combination of electrostatic and hydrophobic interaction between the chemical pattern and the particles and capillary interaction between colloidal spheres.

Assembly on Templates created by Lithography

Although chemically patterned templates are easier to make, physically patterned templates offer better control of the orientation of assembled structures. Van Blaaderen et al. [105] were the first to demonstrate the use of a patterned template to obtain a colloidal crystal with a known crystallographic orientation. Morphological patterning of substrates has been successfully used to direct crystallization in the semiconductor industry as well as in block copolymer ordering. Standard approaches used to create these, are electron beam lithography and interference lithography.

One of the simplest topographical templates consists of periodic grooves with a rectangular shape. Whitesides et al. [145] studied the coupling of laminar flow of colloidal dispersions with topological confinement of particles in the groove. They showed the formation of close-packed hexagonal, rhombic or disordered structures depending upon the ratio of the particle diameter to the width of the groove. More recently, Ozin et al. [146] used templates with tapered dimensions to fabricate colloidal crystals with (100) orientation relative to the substrate. They created anisotropically etched, V-shaped grooves inside Si(100) wafers through lithography. Subsequently, colloidal particles were sucked into these grooves by capillary forces during convective assembly. Colloidal crystals with multiple layers formed as a result. Following the same approach, Yodh et al. [147], achieved well-ordered and defect-free f.c.c. colloidal crystals (up to 50 layers) by using a template with a square pattern.

As a nice continuation of the above approach, Xia et al. [148, 149] used a template

with etched 2D regular arrays of pyramidal tips in Si. The objective was to obtain a f.c.c. colloidal crystal with an orientation different from (111). They were able to obtain f.c.c. crystals with (100) orientation. Matuso et al. [150] demonstrated that by varying the opening angle of the pyramids through lithography, one can control the orientation of the assembled crystal. They obtained f.c.c. colloidal crystals with (100) as well as with (110) orientations. In another work, Xia et al. [129] created colloidal particle aggregates with many shapes such as dimers, triangles, pentagons and hexagons. For this work, they used a template with holes patterned in (110) symmetry. Thereafter, by varying the ratio of the particle diameter to the hole diameter, they were able to create differently shaped aggregates.

Binary colloidal crystals exhibiting building blocks of different sizes were fabricated using a layer-by-layer method by van Blaaderen et al. [123]. The authors prepared a hexagonally close-packed layer of large particles using convective assembly. In the second layer, smaller like-charged particles were directed into the interstices of the first layer, also using convective assembly. The array of arrangements included AB , AB_2 and AB_3 , depending upon the concentration of smaller particles that were used for deposition. More recently, Wang et al. [151] have shown that spin-coating of particles can be used to prepare the second layer. In this method, spin speed determines the final structure. At lower speeds the authors obtained AB_2 order, and at higher speeds, AB_3 order.

Templated self-assembly was originally conceived as a promising route to fabricate complete photonic band gap (CPBG) structures. Colloids are of interest as CPBG building blocks because, by changing the size of the constituent particles, the band gap can be shifted. Although the results outlined in this section are useful, they fail to offer a clear procedure for making CPBG structures. Recently, Santamaria et al. [14] fabricated the diamond cubic structure by using a prefabricated template (with holes arranged in a square pattern), silica and polystyrene (PS) particles. This method is an excellent example of templated assembly.

Chapter 3

Controlled Ordering of Oppositely Charged Colloidal Particles

3.1 Introduction

Ordered crystalline packing of nanoscale particles have technological applications, including those in photonic materials [11, 12, 13], sensing [6, 7, 8] and molecular filters [9, 10]. Ordering in colloidal suspensions, which is a well-known phenomenon, provides a template for ordered nanoscaled structures, if the suspending media can be removed without disrupting particle ordering [152]. Conventional processes for ordering colloids, which employ repulsive forces between particles that carry electrostatic charges of the same sign, produce close-packed crystalline analogs. Using a composite suspension of two particle types, each monodisperse with a different size and with opposing charge, provides a method to create colloidal crystals of lower symmetry [23, 101, 153], and therefore may produce stable structures with novel photonic, sensing, and filtering properties. However, processing methods that produce lower symmetry structures prove to be more difficult to realize, primarily because the colloidal composites attractive electrostatic and vdW forces limits the length scale of ordering.

Researchers have shown that a suspension with oppositely charged particles can have long-range order if the particles are weakly charged and sterically stabilized

[23]. Additionally, the Debye length needs to be on the scale of particle diameter and the vdW forces need to be absent. As a result, although the particles can stay ordered (in the solvent), the stabilizing forces are mild. Therefore the structure can be destroyed on exposure to atmosphere or vibrations, or when the solvent is removed. Such a system has limited applicability. Recently, Mukhopadhaya et al. [154] showed that strongly and oppositely charged PS particles can order irrespective of their surface charge. Neither did they disclose the Debye length in the system from which these structures were crystallized, nor did they elaborate on the stabilizing forces and mechanism. Their results are contrary to the available literature about oppositely charged particles. For instance, a simple experiment shows that when positively charged PS particles are distributed onto a layer of negatively charged PS particles, attractive electrostatic forces are so strong that they trap the particles in a deep primary minimum. The resulting structure has no long-range order. Therefore, in the absence of a clear explanation it becomes imperative to understand the mechanism for ordering oppositely charged colloids. Factors that influence the assembly of oppositely charged particles into ordered structures can then be exploited to make three dimensional structures that remain ordered as the solvent dries.

Ordered aggregates of oppositely charged particles show greater stability compared to their like-charged counterparts. Therefore, they are better candidates for making low-volume non-close-packed structures. Whereas the like-charged analogs are stabilized by vdW forces only, the oppositely charged non-close-packed structures are stabilized by vdW as well as electrostatic forces.

A layer-by-layer method is reported herein [22], and demonstrates a simple processing route for making 2D low-symmetry packing of strongly and oppositely charged colloids. Previous observations [23] demonstrate that sterically stabilized, weakly and oppositely charged colloidal particles can produce low-symmetry ordering in suspensions. However, these colloidal crystals are stable when in suspension and for weakly charged particles. Schevchenko [155] on the other hand, has shown that it is possible to evaporate the solvent and retain order for smaller, weakly charged nanoparticles.

Three studies are discussed in this chapter. In the first study, spin-coating is

used to distribute charge-stabilized colloids [151] on an underlying layer of larger and oppositely charged colloidal particles. It is demonstrated that a surface agent, which produces short-range steric repulsion, permits ordering even as the particles' opposing charges are increased to magnitudes that prevent ordering in previous observations.

In the second study, it is shown that, by manipulating the electrostatic repulsion between like-charged particles, a non-close-packed layer of particles can be assembled on a layer of close-packed and oppositely charged particles. Since capillary attraction between particles can lead to close-packed structures, schemes that rely on rapid assembly through evaporation of the solvent cannot be used here. As a result, dip-coating is used to distribute and arrange particles in the second layer.

In the third study [156], ordering of hydrophobic, charged particles on charged surfaces is discussed. It is shown that amphiphilic surfactants can be used to order hydrophobic particles on hydrophobic, like-charged surfaces.

3.2 Materials and Methods

3.2.1 Colloidal suspensions

Suspensions of monodisperse polystyrene (PS) beads measuring 100 nm (amidine functionalized, $\zeta = 52.56$ mV at $\kappa^{-1} = 127$ nm, and charge density measured by the manufacturer equal to 0.032 C/m²) 210 nm (amidine functionalized, $\zeta = 54.62$ mV at $\kappa^{-1} = 127$ nm, and charge density measured by the manufacturer equal to 0.1 C/m²) and 420 nm (sulphate functionalized, $\zeta = -61.57$ mV at $\kappa^{-1} = 127$ nm, and charge density measured by the manufacturer equal to -0.032 C/m²) were purchased from Molecular Probes Inc., Eugene, OR. Electrophoretic mobility for different colloidal samples was measured using a Zeta-PALS (Brookhaven Instruments Corporation). Once electrophoretic mobility was measured, zeta potential was calculated using the Smoluchowski model. The PS suspensions were dialyzed against DI water to lower their salt concentrations before use.

3.2.2 Surfactants

Triton-X 100 ($(C_{14}H_{22}O(C_2H_4O)_n)$) was purchased from VWR International Inc. In most cases 60-70 μl of 10 w/v% Triton X-100 was added to 1 ml of the final suspension of colloidal particles before spin-coating. Adsorption of the non-ionic surfactant on PS was measured by Quartz Crystal Microbalance (QCM-D E4 from Q-Sense AB, Sweden). A single sensor crystal with PS spin-coated on gold, which was purchased from Q-Sense, was used for all the experiments. QCM can measure the change in the resonance frequency depending on the change in mass of the sensor crystal, i.e. if anything is adsorbed or desorbed from the sensor crystal. The change in frequency can be related to the change in mass by the Sauerbrey equation (eq. 3.1).

$$\Delta m = -C \frac{\Delta f}{n}, \quad (3.1)$$

where Δm is the change in mass and Δf is the corresponding change in resonance frequency. C is $17.7 \text{ ng cm}^{-2} \text{ Hz}^{-1}$ and denotes a constant that characterizes the sensitivity of the equipment to the change in mass and n is the resonance overtone. For all the measurements described in this study, the third overtone ($n=3$) was used at a temperature of 25°C . The fundamental resonance frequency for the sensor crystal was 4.95 Mhz. The sensor crystal was cleaned with copious amount of de-ionized (DI) water prior to any measurement. Thereafter, it was placed in the QCM cell where a baseline measurement was done in DI water. This was followed by QCM measurements in Triton-X 100 suspensions in DI water. Five suspensions of Triton-X 100 in DI water were used in this study. They were 0.01cmc, 0.1cmc, cmc, 5cmc and 10cmc, where cmc is the critical micelle concentration for Triton-X 100 (cmc for Triton-X 100 in water is 0.24 mM [157]). Between any two measurements, the adsorbed surfactant was washed off the sensor crystal by running DI water through the cell. A flow rate of 0.5 ml/min was maintained during all the QCM measurements.

Cationic Polyelectrolyte Dodecyltrimethylammonium bromide (DTAB, $CH_3 - (CH_2)_{11} - N^+ - (CH_3)_3 - Br^-$) has a cmc of 15.6 mM/l (i.e., 4.810 mg/ml). It dissociates in aqueous solution with a positively charged headgroup. The concentra-

tions used in this study ranged from 0 to 4 mg/ml. Block copolymer (BCP) Poly(N-methyl 2-vinyl pyridinium iodide-b-ethylene oxide) (P2VPQ-PEO) was bought from Polymer Source Inc. Between 0-0.5 M of this amphiphilic and cationic BCP, was used in experiments.

3.2.3 Solvents

De-ionized water (DI water) was used for most of the experiments and was readily available. However, in one case, Class 1 isopropanol (Hubbard Hall Inc.) 80%-DI water 20% mixture, was used. The Debye screening length for DI water with varying salt concentrations was calculated based on conductivity measurements (YSI 3200 Conductivity Instrument).

3.2.4 Template

Interference Lithography

Interference lithography (IL) provides an easy and simple way to create periodic patterns on a substrate. With a single exposure, pattern of gratings with periods as small as 170 nm can be written. More complex patterns, like grids, holes or poles can be written with multiple exposures.

The basic principle of interference lithography (IL) is as follows: two mutually coherent beams of light intersect and form a standing wave in the region where these two overlap. Fig. 3-1 shows the set-up for an IL system. For this thesis, Lloyd's mirror IL was used. In a Lloyd's mirror IL set-up, spatial as well as temporal coherence is important to consider. Temporal coherence defines the narrowness of the range of wavelengths from a light source. For IL, the important measure of temporal coherence is coherence length. This defines the maximum distance along the direction of propagation of the light wave, over which, waves can be expected to show mutual coherence. If light waves come from different sources, they would be incoherent. Thus, a single light source is used to promote mutual coherence. In a Lloyd's mirror set-up, the mirror divides a wavefront from the source into two overlapping beams that form

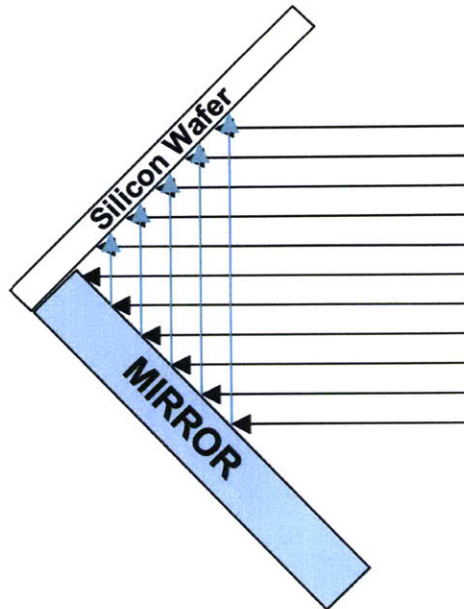


Figure 3-1: A schematic for the Lloyd's Mirror Interference Lithography set-up

the interference pattern. In order to form a fringe pattern with good contrast, the path lengths of the two interfering beams from the source to a point on the substrate should differ by less than the coherence length. In the current set-up, the light comes from a helium-cadmium (HeCd) laser, emitting at 325 nm. The particular model of laser used in the Lloyds mirror has good temporal coherence, with a coherence length of 30 cm, long enough that temporal coherence is generally not a concern.

Spatial coherence defines the uniformity of the wavefronts along the width of the beam. For instance, if a source has good spatial resolution, it will appear like a point in space and the wavefronts will appear as concentric spheres centered on a point. In the Lloyd's mirror set-up, the light is spatially filtered before reaching the substrate. Practically, the beam should expand to cover the exposure area with high intensity and uniformity. This is achieved by using a lens to focus the beam through a $5\ \mu\text{m}$ pinhole. Since there are no collimating optics between the pinhole and the substrate, the beam expands to a diameter of about 30 cm at the wafer chuck. As the spatial filter is the last element before the light reaches the substrate, the wavefronts reaching

the substrate are nearly spherical.

Template preparation

Silicon templates were prepared through IL. A 4-inch silicon wafer was spin coated with negative photoresist PS4. After baking, this was exposed to a 325 nm wavelength, HeCd laser. A pattern of holes arranged in (110) symmetry was created as follows. The baked wafer was exposed in IL for 33 seconds at 0.23 mW. It was then rotated 90 degrees and exposed again for 33 seconds at 0.23 mW. The resulting pattern was baked for 90 seconds at 110 °C and then developed in CD-26 developer for 60 seconds. This creates a pattern of holes with (110) symmetry in the photoresist. To etch the pattern of holes into silicon, the sample is treated in a plasma-etcher with $CF_4 - O_2$ plasma at 20 mTorr for 3 minutes. In the end, the photoresist is removed by treating in O_2 plasma at 20 mTorr for 7 minutes. A schematic for template preparation is shown in fig. 3-2.

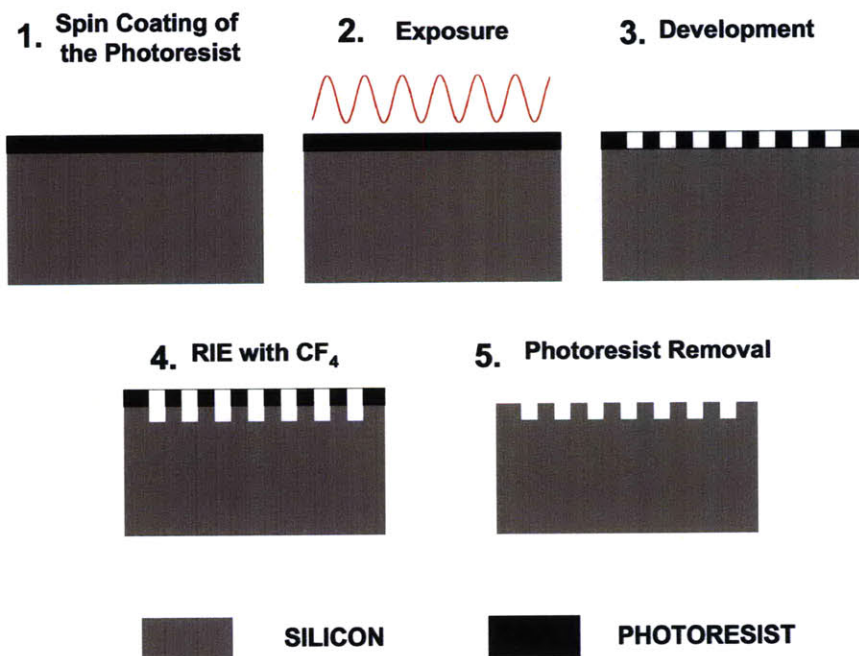


Figure 3-2: A schematic for the procedure to fabricate the template

3.2.5 Spin-coating

Glass substrates to be used, were cleaned by ultrasonication in acetone followed by treatment in Pirhana solution, which is a mixture of concentrated sulfuric acid (VWR international Inc.) and hydrogen peroxide (Alfa Aesar) ($H_2SO_4 : H_2O_2 = 3:1$, volume ratio) to obtain a hydrophilic surface. It was then washed with copious amounts of water and dried with nitrogen gas before use. The first layer from negatively charged PS particles was made by convective self-assembly. In this method the clean micro glass plate was fixed vertically inside a beaker, which contained the colloidal suspension at 35°C as the suspension is slowly pumped out of the beaker forcing the particles to pack under the capillary forces.

Spin-coating was used to distribute the positive PS particles on the substrate made from negative PS particles. Spin-coating has been previously used to make charge stabilized 2D colloidal crystals [151]. Starting with $50\mu\text{l}$ of the dialyzed colloidal solution with manufacturer supplied concentrations (provided above), 0.25-w/v% and 1.0 w/v% suspensions of 100nm positive PS particles were prepared for spin-coating in DI water whereas 1.0-w/v% solution of 210 nm positive PS particles was prepared in DI water. In most cases $60\text{-}70\ \mu\text{l}$ of 10-w/v% Triton X-100 was added to the final solution before spin-coating. Spin-coating was done at 3000 rpm for 60 seconds for all of the above systems by putting approximately $20\ \mu\text{l}$ of the resulting solution, on a substrate of negatively charged 420 nm PS particles. Additionally, for 0.25-w/v% solution of 100nm positive PS particles, spin-coating at 3000 rpm was done with 0.01635 mM, 0.094 mM and 0.879 mM NaCl salt concentrations. Table 3.1 lists the Debye lengths that are inferred from conductivity measurements on solvents without addition of any colloidal particles to the solvent, for the above three salt concentrations and a measurement with no added salt (DI water). Calculations show that on addition of colloidal particles, the change in Debye length, due to the counterions from charged particles is not substantial. Therefore, the Debye lengths calculated [158] for solvents without addition of particles were used for all calculations in this work. For 1-w/v% solution of 100 nm positive PS particles, spin coating at 6000 rpm

for 60 seconds was also done. Finally, the spin-coated substrates were sputtered with gold for 20 seconds before being imaged under the Scanning Electron Microscope (SEM) (Gemini 982, Zeiss).

Table 3.1: Variation of Debye length with increasing NaCl concentration in water

NaCl concentration [$\times 0.01$ mM]	Debye screening length [nm]
No added salt (DI water)	250.354
1.635	75.22
9.4672	31.26
87.9	10.256

3.2.6 Dip-coating

Dip-coating was used to form a non-close-packed layer of colloidal particles on an underlying layer of oppositely charged particles. The substrate was a close-packed layer of 420 nm negatively charged spheres. Before dip-coating the substrate, it was made hydrophilic by exposure to oxygen plasma for 10 seconds. This is required for obtaining a monolayer of particles in subsequent deposition steps. Thereafter, it was dipped in a 0.1-w/v% suspension of 140 nm positively charged PS particles for 60 seconds. In order to reduce irreversible coagulation of oppositely charged colloidal particles due to electrostatic attraction, Triton-X 100 was added to the suspension of positively charged particles. By lowering the surface tension of water, Triton-X 100 also reduces capillary attraction between positive PS particles. To further limit the close-packing of positive PS spheres, the substrate is slowly withdrawn, manually, from the suspension of colloids and immersed in DI water without drying. It is allowed to stay in water for about 60 seconds, after which it is dried at ambient temperature (25°C).

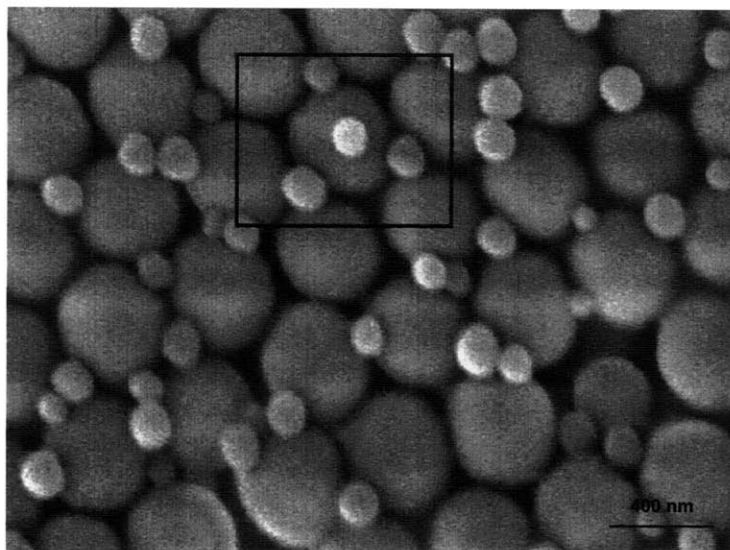


Figure 3-3: SEM image of 100 nm diameter positively charged PS sphere suspension (0.25-w/v%) spin-coated at 3000 rpm on a substrate made from 420 nm diameter negatively charged PS spheres

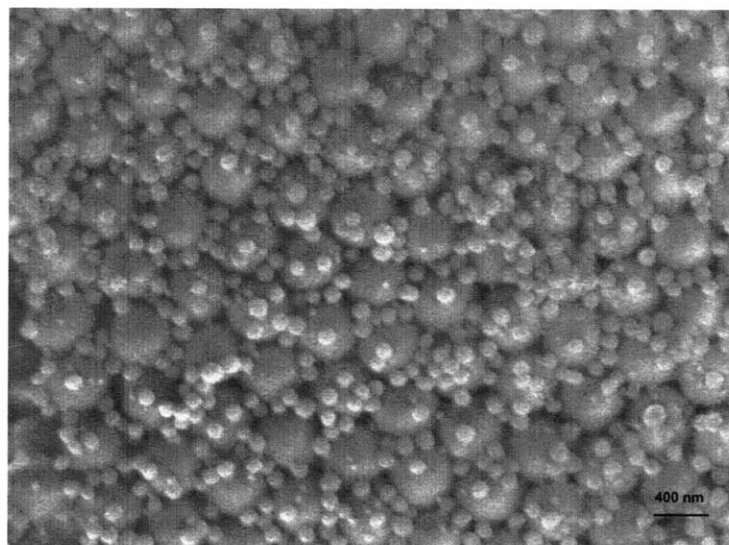


Figure 3-4: 100 nm diameter positively charged PS sphere suspension (1.0-w/v%) spin-coated at 3000 rpm on a substrate made from 420 nm diameter negatively charged PS spheres

3.3 Spin-coating of Oppositely Charged Colloids

Fig. 3-3 and fig. 3-4 are SEM images for 100 nm positively charged polystyrene (PS) particles suspended in DI water and spin-coated on a hexagonally ordered packing made from 420 nm negatively charged PS particles. These figures indicate that some short-range order may be present but long-range ordering is not produced by spin-coating positive PS particles on the negatively charged substrate of PS particles when no surfactant is added. While not representative of most of the system, the short-range order (enclosed within the box in fig. 3-3) showing a 100 nm positive PS sphere separated from the other three 100 nm ($= D$) diameter spheres by a distance $h (= r - R_1 - R_2)$ of 193.97 nm ($\approx 2D$), is produced by electrostatic repulsion between the positively charged PS spheres since the Debye length in the present case is on the order of the interstitial spacing ($250.5 \text{ nm} \approx 2.5D$). The absence of long-range order in fig. 3-3 and fig. 3-4 can be attributed to the strong DLVO attraction between oppositely charged PS particles. Besides the strong electrostatic attraction between oppositely charged colloids, the hydrophobic interaction between PS spheres also reduces the mobility of positive PS spheres, being spin-coated. However, as discussed in section 3.5, introduction of a short-range repulsive interaction, in the form of a steric barrier can lead to ordered assemblies.

3.3.1 Surfactantless spin-coating of colloidal particles

In the absence of a non-ionic surfactant, electrostatic and vdW attraction prevent ordering of the spin-coated oppositely charged colloidal spheres whereas the hydrophobic interaction between the positive and negative PS spheres reduces their mobility.

Spin-coating positive PS spheres from a suspension with reduced electrostatic interaction (in other words by increasing the salt concentration) leads to lower electrostatic attraction between oppositely charged colloidal spheres. The increased salt concentration concomitantly reduces the electrostatic repulsion between positively charged PS spheres, resulting in their coagulation during spin-coating. Additionally, hydrophobic interaction between the positive and negative PS spheres still prevents

greater mobility of the spin-coated PS spheres. In order to improve the mobility of the spin-coated positive PS spheres the solvent was changed from DI water to an isopropanol(80%)-DI Water(20%) mixture. Isopropanol wets PS better than water and therefore leads to greater mobility of the particles being spin-coated on the substrate. Additionally, isopropanol has a lower surface tension than water and exerts a weaker capillary force than water. This can lead to fewer coagulates. Not surprisingly, DI water-IPA suspension of 100 nm negatively charged PS particles when spin-coated onto a substrate made from 420 nm negatively charged PS leads to an ordered packing. However, on spin-coating positively charged PS particles suspended in a mixture of isopropanol and DI water, there are a number of coagulates as well as a disordered structure as shown in fig. 3-5. Isopropanol has a relative permittivity (≈ 20) nearly a fourth that of water (≈ 80.1) and therefore a Debye length which is half that of water under identical salt concentrations. The coagulation in the presence of isopropanol can therefore be explained based on reduced Debye length. Moreover on using 80%-20% mixture of isopropanol- DI water, although leading to greater mobility for spin-coated positive PS spheres, is not sufficient to offset the strong electrostatic and vdW attractive forces. This leads to the disordered packing observed in fig. 3-5.

3.3.2 Spin-coating of colloidal particles with non-ionic surfactant

Long-range and well ordered regions of oppositely charged colloidal particles are observed on spin-coating positive PS sphere suspension with a non-ionic surfactant (Triton X-100 ($C_{14}H_{22}O(C_2H_4O)_n$ with $n \approx 9 - 10$) [159, 160] on the substrate made from negative PS spheres (fig. 3-6), where the hydrophobic end of the surfactant adsorbs to the PS surface; the other end is hydrophilic and soluble in water. Adsorption of the non-ionic surfactant on the positive PS particle surface leads to a steric barrier, which serves as a short-range repulsive force. Because this surfactant is non-ionic, it has no effect on the total surface charge and prevents particle coagulation whereas

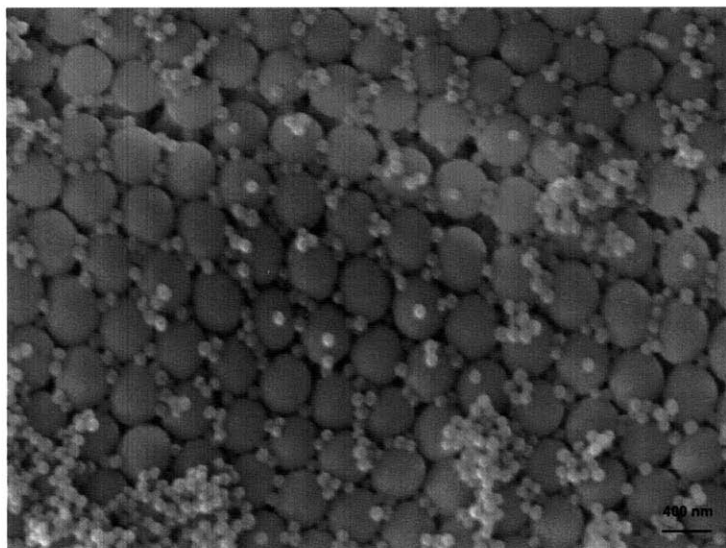


Figure 3-5: 100 nm diameter positively charged PS sphere suspension (1.0-w/v%) in isopropanol (80%) – DI water (20%) spin-coated at 3000 rpm on a substrate made from 420 nm diameter negatively charged PS spheres

the amphiphilic character of it produces a change in the hydrophobicity of PS. As shown in section 3.5, this promotes particle rearrangement into lower energy configurations during spin-coating. Other non-ionic, amphiphilic surfactants may produce long-range ordering as well. Spin-coating from a 0.25-w/v% suspension of positively charged PS particles in water at 3000 rpm, with Triton-X 100 in the suspension, produces the 2D LS_2 ordered structure shown in fig. 3-6 (size ratio of 4.2). The LS_2 structure remains stable up to a particle size ratio of 2 (210nm positive PS on 420 nm negative PS) (fig. 3-8). On doubling the rotation rate of the spin-coater to 6000 rpm and increasing the concentration of 100nm positive PS particles in the suspension to 1.0-w/v%, a LS_6 long-range ordering is present (fig. 3-10). Ordered regions were typically 200-400 μm^2 large, as shown in fig. 3-12 and fig. 3-13. Combining rapid ordering of oppositely charged colloids through spin-coating with templated assembly, one can fabricate binary colloidal crystals with a non close packed orientation. By using a template, a layer of 250 nm negatively charged PS particles were ordered with (110) orientation, through convective assembly. In the second step, spin-coating was used to spread 20-40 μl of a 1.5-w/v% suspension of 140 nm positively charged

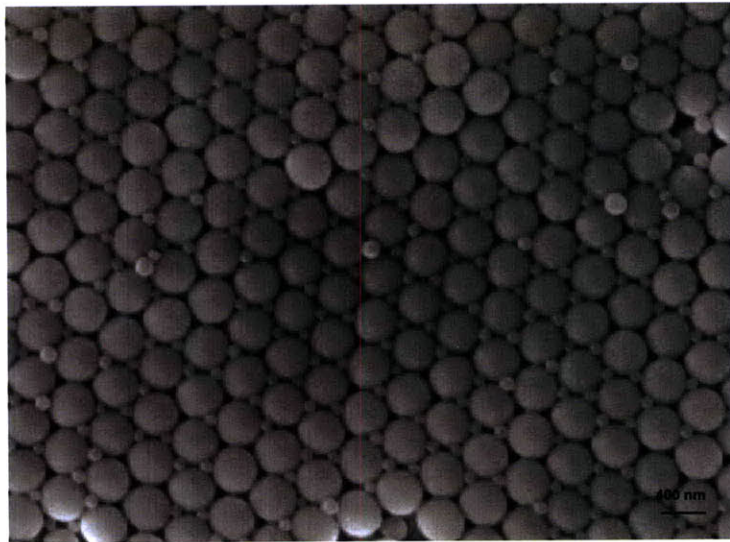


Figure 3-6: 100 nm diameter positively charged PS sphere suspension (0.25-w/v%) in DI water with Triton X-100, spin-coated at 3000 rpm on a substrate made from 420 nm diameter negatively charged PS spheres for 60 seconds

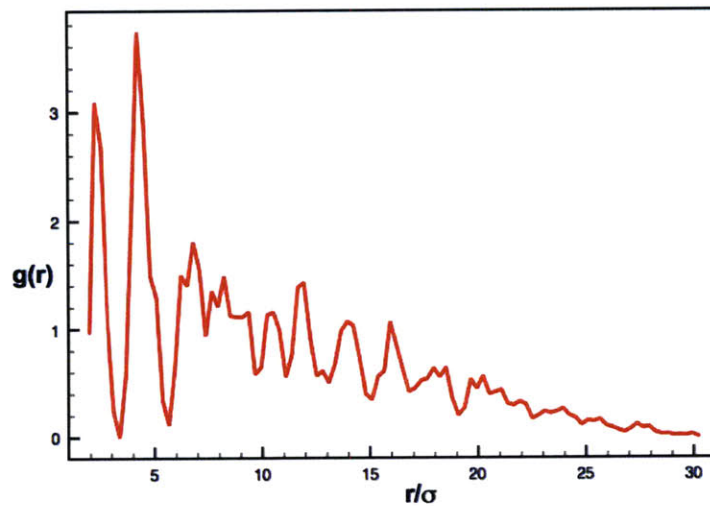


Figure 3-7: Pair distribution function (pdf) for small particles from fig. 3-6, σ is the diameter of the small sphere

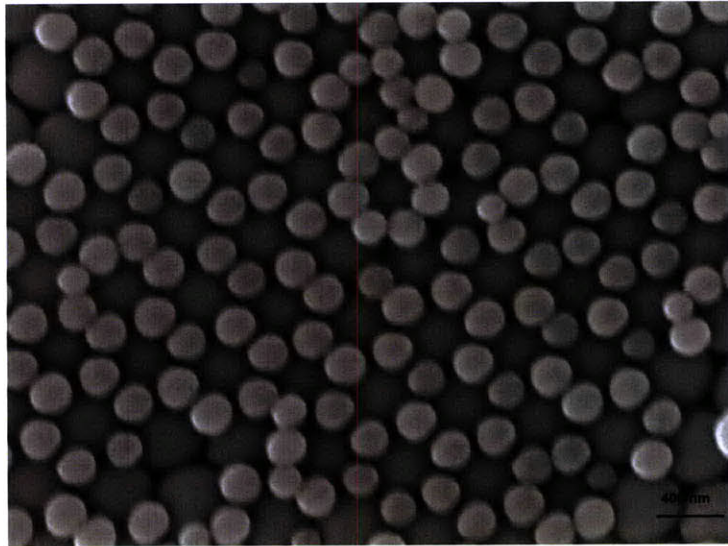


Figure 3-8: 210 nm diameter positively charged PS sphere suspension (1.0-w/v%) in DI water, spin-coated at 3000 rpm on a substrate made from 420 nm diameter negatively charged PS spheres for 60 seconds

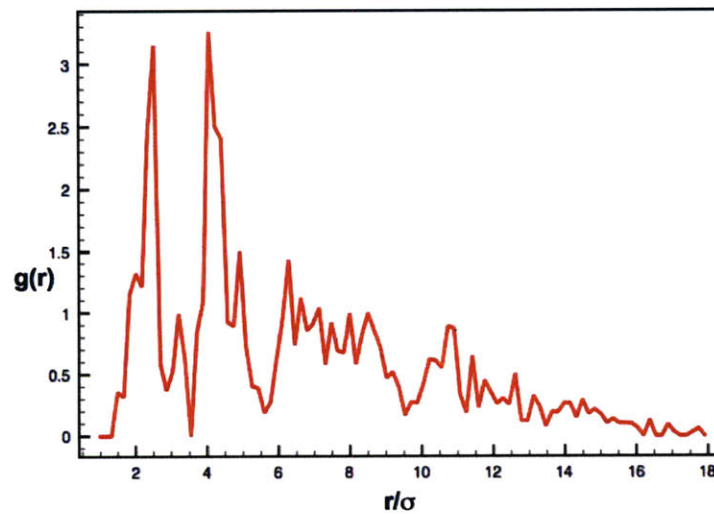


Figure 3-9: Pair distribution function (pdf) for small particles from fig. 3-8, σ is the diameter of the small sphere

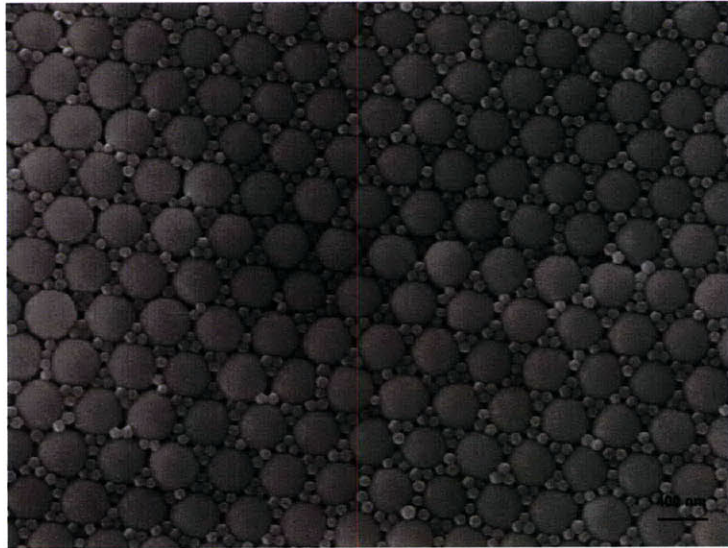


Figure 3-10: 100 nm diameter positively charged PS sphere suspension (1.0-w/v%) in DI water, spin-coated at 6000 rpm on a substrate made from 420 nm diameter negatively charged PS spheres for 60 seconds

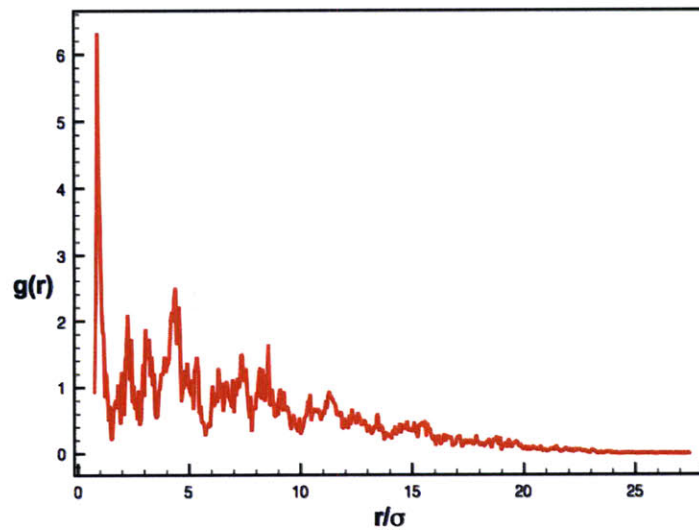


Figure 3-11: Pair distribution function (pdf) for small particles from fig. 3-10, σ is the diameter of the small sphere

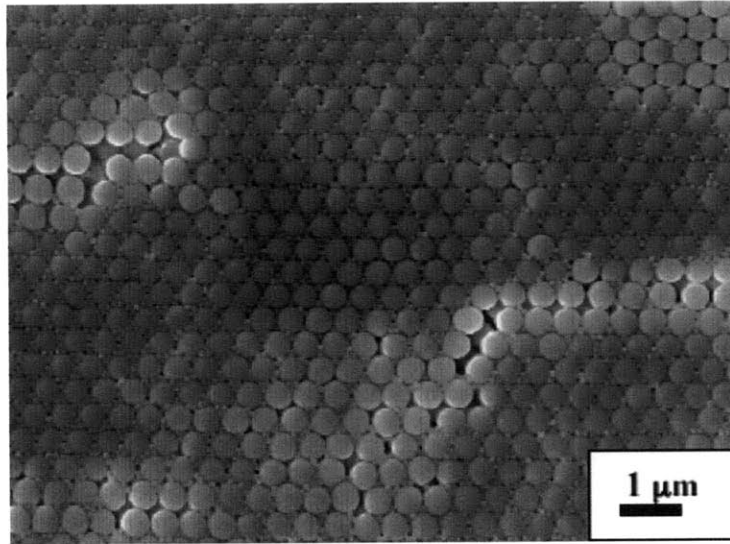


Figure 3-12: SEM image of a larger domain with LS_6 ordering

PS particles on the substrate at 3000 rpm. The resulting structure has CsCl symmetry. Fig. 3-14 shows a SEM micrograph where the first layer of 250 nm negative PS particles and the second layer of 210 nm positive PS particles are seen.

3.4 Dip-Coating of Oppositely Charged Colloids

The zinc blende or the ZnS structure has been reported to have a complete photonic band gap (CPBG) [12] with a large enough dielectric contrast. Indeed, by merely scaling the size of the colloidal constituents in this structure, the frequencies that are blocked can be changed. Along the (111) plane, ZnS presents a unique configuration in which only one type of charged species constitutes a layer. The assembly of ZnS type structure was attempted through the following procedure: the starting substrate should have f.c.c. symmetry with (111) orientation and it should be made of like-charged (negative) colloids. The second layer of particles should be oppositely charged and smaller. These should fill only half of the interstices on the first layer. The final structure is akin to the schematic shown in fig. 3-15. The third layer of negatively charged colloids then sits on top of the positive ones. Fig. 3-16 shows the most

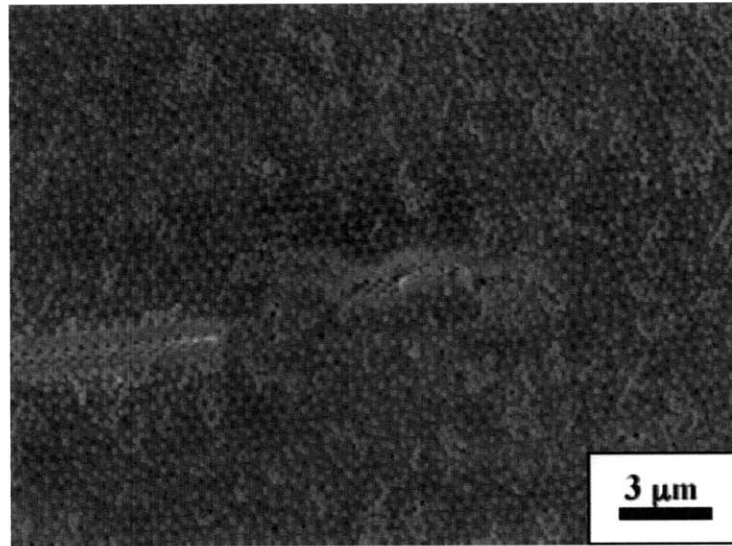


Figure 3-13: SEM image of a larger domain with LS_2 ordering

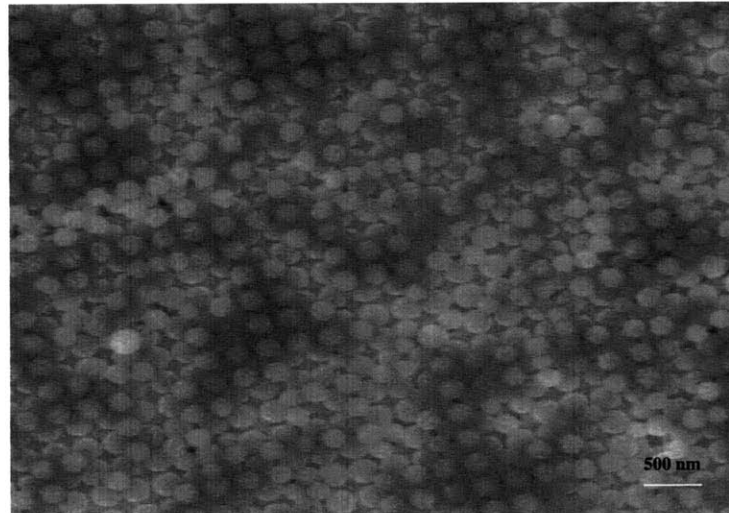


Figure 3-14: 140 nm diameter positively charged PS sphere suspension (1.0-w/v%) in DI water, spin-coated at 3000 rpm on a substrate made from 250 nm diameter negatively charged PS spheres for 60 seconds. The layer of 250 nm particles were assembled on a template with holes arranged in (100) symmetry, through convective assembly.

energetically favorable positions for negative PS particles in the third layer. The most energetically favorable positions for positive particles in the fourth layer are shown in fig. 3-17.

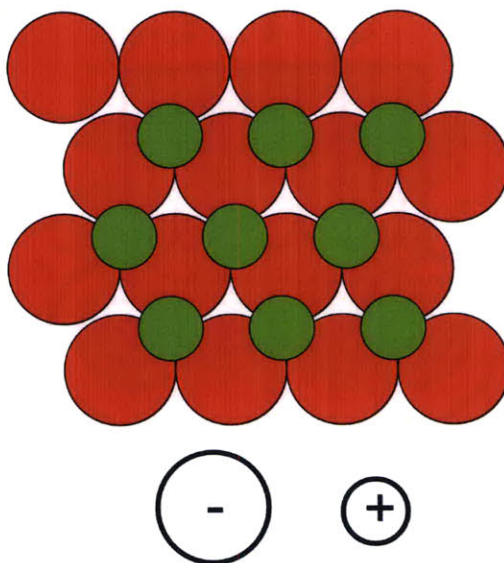


Figure 3-15: A schematic showing the first two layers for a layer-by-layer assembly of ZnS-type structure. Green spheres represent positive PS particles in the second layer and red spheres represent negative PS particles from the first layer. In the second layer only half of the total interstices are occupied.

Fig. 3-18 is a SEM micrograph of a non-close-packed layer of 140 nm positive PS particles arranged on top of a close-packed layer of 420 nm negative PS particles. The first layer of negative particles was deposited using convective transport from a suspension of 420 nm PS particles. For the second layer, adsorption seems to be the most appropriate method. The parameter that determines the ordering in the second layer is the Debye screening length in the suspension of positive PS particles. Since the particles are oppositely charged, the amount of contact between the negatively charged substrate and the suspension of positively charged particles is critical. As a result, convective assembly cannot be used to deposit particles in the second layer. Although an assembly of particles through dip-coating is less uniform, limited time of contact between oppositely charged particles is a more important factor.

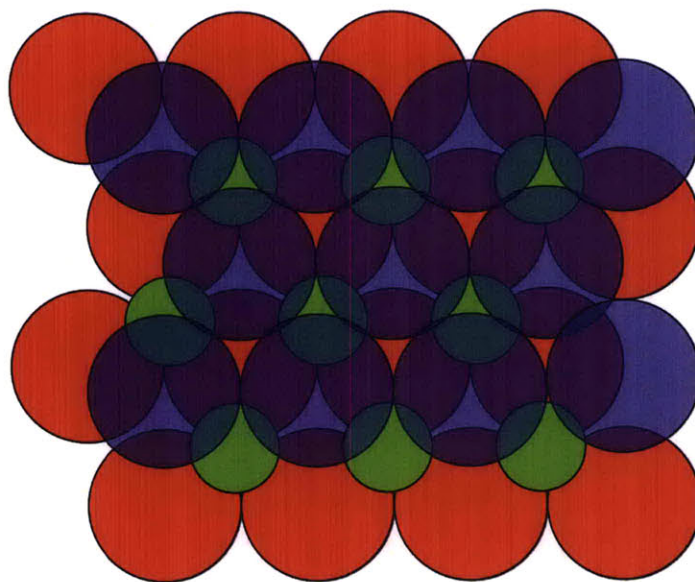


Figure 3-16: A schematic showing the first three layers for the layer-by-layer assembly of ZnS-type structure. Green spheres represent positive PS particles in the second layer and red spheres represent negative PS particles. The position of negative particles in the third layer is shown in translucent blue.

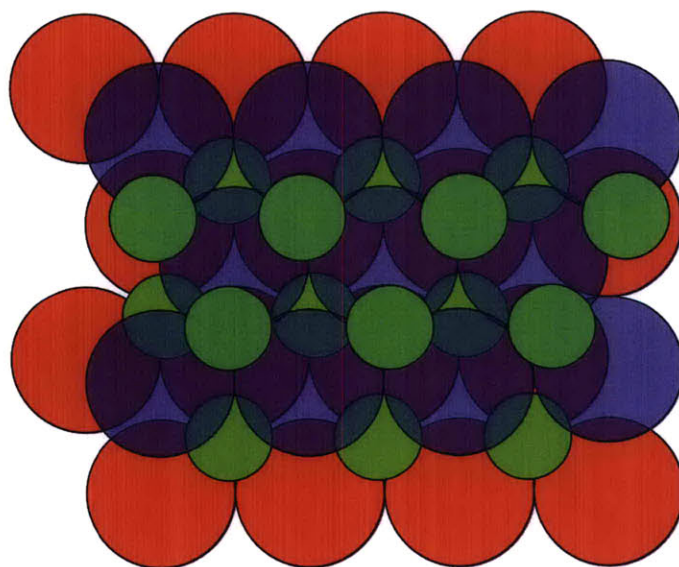


Figure 3-17: A schematic showing the first four layers for a layer-by-layer assembly of ZnS-type structure. Green spheres represent positive PS particles in the fourth layer and red spheres represent negative PS particles

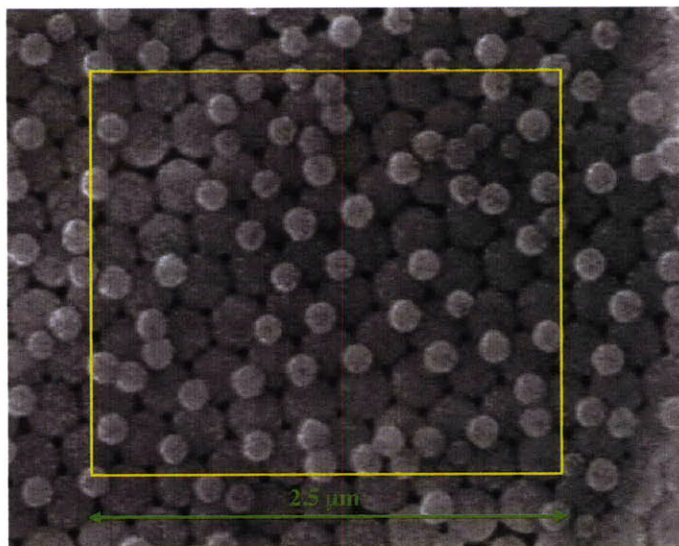


Figure 3-18: SEM image after a suspension of 0.1-w/v% 140 nm diameter positively charged amidine functionalized PS spheres with Triton X-100, deposited on a substrate of 420 nm negatively charged PS particles which were arranged in f.c.c. pattern with (111) orientation. The dip-coating lasted for 60 seconds

3.5 Theoretical Calculations

Most studies on the heterocoagulation of charged colloidal particles rely on determining the stability factor through turbidity studies [161]-[164]. However, here the interparticle energy for colloidal particles with and without Triton-X 100 is calculated and it is shown that the increased stability imparted by adsorbing Triton-X 100 onto oppositely charged particles maybe the reason for ordering.

The interaction energy of geometric configurations relevant to the observed structures was calculated as follows. Following Maskaly et al., the method of Derjaguin, Landau, Verwey and Overbeek (DLVO theory) is adapted to model interactions between oppositely charged colloidal particles. The two important interaction terms in DLVO theory for the present systems are the vdW and electrostatic. Although the Hogg Healy and Fuerstenau model (HHF) [165] is usually used to describe the electrostatic behavior for heterocoagulation studies, it is valid at high ionic concentrations. Because here experiments were done at low ionic concentration, the Yukawa pair-potential provides a good approximation to the electrostatic interaction between

two charged spheres. However, a two-particle potential may not suffice in cases where local order produces multiple particle proximity effects. Thus, a numerical solution of the Poisson-Boltzmann equation [166] is used to calculate the interaction energy for a collection of charged spheres.

The steric interaction between colloidal particles was modeled by using Vincents formulation [167]. QCM measurements, described earlier in section 3.2.2 show that the adsorption plateau is reached at close to cmc of Triton-X 100. These results are tabulated in table 3.2. As the concentration of Triton X 100 used for the current experiments were always greater than cmc, a uniform profile for the adsorbed non-ionic surfactant is assumed. Vincents analysis had two steric contributions for approaching polymer or surfactant coated spheres: if δ denotes the average thickness of the surfactant coils covering the particle surface then the interaction has an osmotic component at intermediate separations H , i.e. ($\delta < H < 2\delta$) (eq. 3.2).

Table 3.2: Variation of Triton-X 100 coverage on Polystyrene with bulk concentration of Triton- X 100, as determined by QCM

Triton-X 100 concentration in DI water [\times cmc] (cmc = 0.24 mM)	Coverage [$\mu\text{M}/\text{m}^2$]
0.01	1.16
0.1	2.2
1.0	3.57
5.0	3.40
10.0	3.44

$$E_{osm}(\delta < H < 2\delta) = 8\pi k_B T R_1 R_2 \phi^2 (0.5 - \chi) \frac{(\delta - 0.5H)^2}{\nu_1(R_1 + R_2)}. \quad (3.2)$$

At smaller separations an elastic component arises and the interaction is modeled as shown below in eq. 3.3

$$E_{osm}(0 < H < \delta) = 8\pi k_B T \delta^2 R_1 R_2 \phi^2 (0.5 - \chi) \frac{(\frac{H}{2}\delta - 0.25\ln(\frac{H}{\delta}))}{\nu_1(R_1 + R_2)}, \quad (3.3)$$

where R_1 and R_2 are the radii for spheres 1 and 2 respectively, ϕ is the effective volume

fraction of the segments in the adsorbed layer, ν_1 is the molecular volume of the solvent and χ is the Flory-Huggins solvency parameter. $\nu_1(\text{water}) = 2.99 \times 10^{-29} \text{m}^3$ and χ is 0.45 for Triton-water. Using the electrostatic interaction, the interaction energy is calculated in the absence of a surfactant, at sequential positions (fig. 3-19) of a 100 nm positive PS sphere on the surface of one of the seven negative 420 nm PS spheres that form a close-packed layer. As shown, the most stable configuration occurs when the positively charged particle settles into the interstice of the fixed negatively charge particles. Although it is energetically favorable, this configuration is rarely observed on large length-scales after spin-coating in the absence of Triton-X.

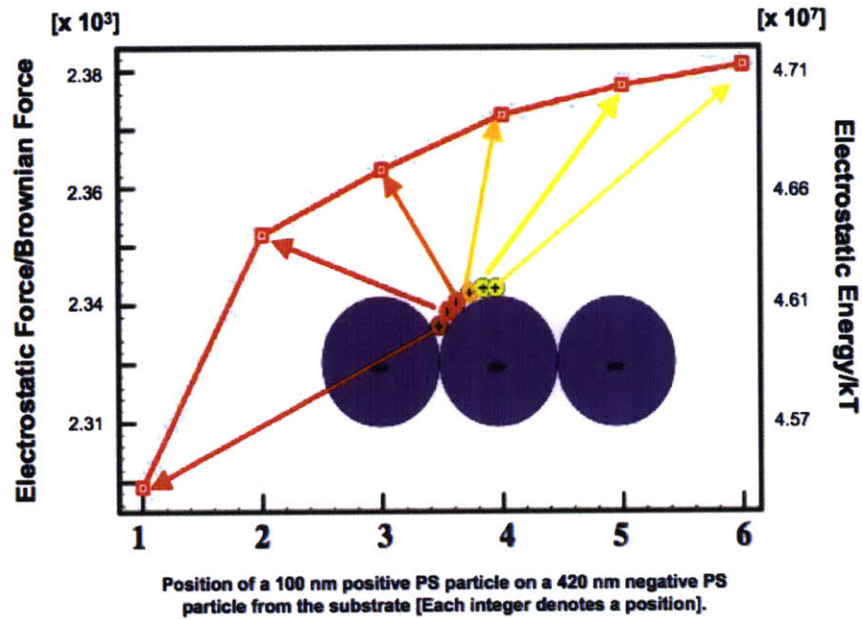


Figure 3-19: Normalized electrostatic force (relative to the Brownian force) and electrostatic energy (relative to $k_B T$) with respect to the position of a 100 nm positive PS sphere moving on the surface of one of the 420 nm negative PS spheres, which are packed into close packed with fcc (111) orientation. Salt concentration has been assumed to be 0.001 mM whereas the surface charge density for each kind of sphere has been assumed to be identical to the value supplied by the manufacturer. The calculation was done by solving the linearized Poisson Boltzmann equation for a system of 7 negative PS spheres and one positive PS sphere through the PoissonBoltzmann solver. For position 1, the positive PS sphere sits in the crevice formed by 3 negative PS spheres. $\theta_2 = 45^\circ$, $\theta_3 = 55^\circ$, $\theta_4 = 65^\circ$, $\theta_5 = 75^\circ$ and $\theta_6 = 90^\circ$

Because thermal effects should be insufficient to produce disorder, it can be inferred that the presence of surfactant's steric hindrance promotes ordering via surface slip after and during deposition. This surface slip is accommodated by the larger equilibrium separation. This is illustrated by fig. 3-21 where the interaction is the sum total of the vdW, electrostatic and the steric energies. With no steric hindrance the attractive interaction produces different minimizing configurations. These observations suggest that steric hindrance makes the primary minima (of the DLVO potential) inaccessible and leaves the observed interstitial positions as the only energetically favored location.

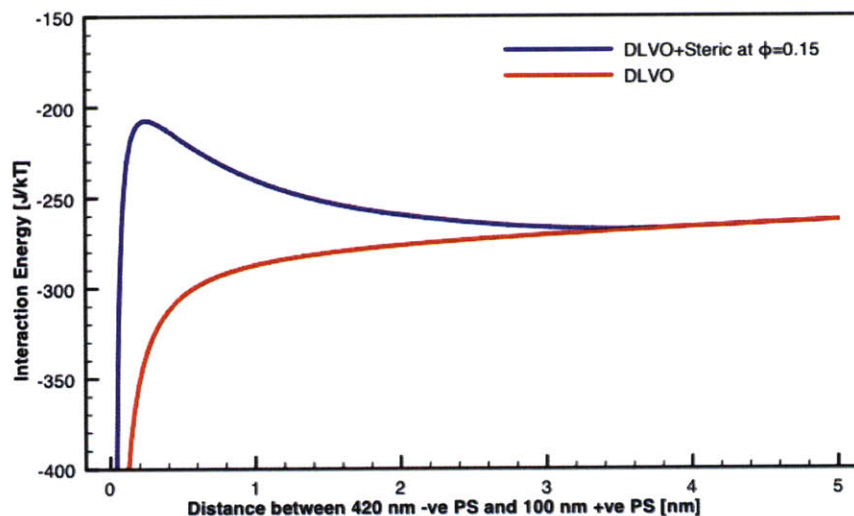


Figure 3-20: DLVO (van der Waals + electrostatic) interaction energy (in red) and DLVO + steric interaction energy (in blue). The above calculations are for a negative 420 nm PS and a positive 100 nm PS approaching each other in water. For the steric interaction, $\phi = 0.10$, $\nu_1 = 0.03nm^3$ and $\chi = 0.45$

The steric interaction between colloidal particles has been widely researched and extensive literature exists detailing the various aspects that control it ([31] and the references contained therein). From eq. 3.2 and eq. 3.3 one of the most important parameters in controlling the interaction is ϕ . By changing the volume fraction of the adsorbed surfactant one can vary the magnitude of the steric repulsion even in the presence of very strong electrostatic attraction as modeled in fig. 3-21.

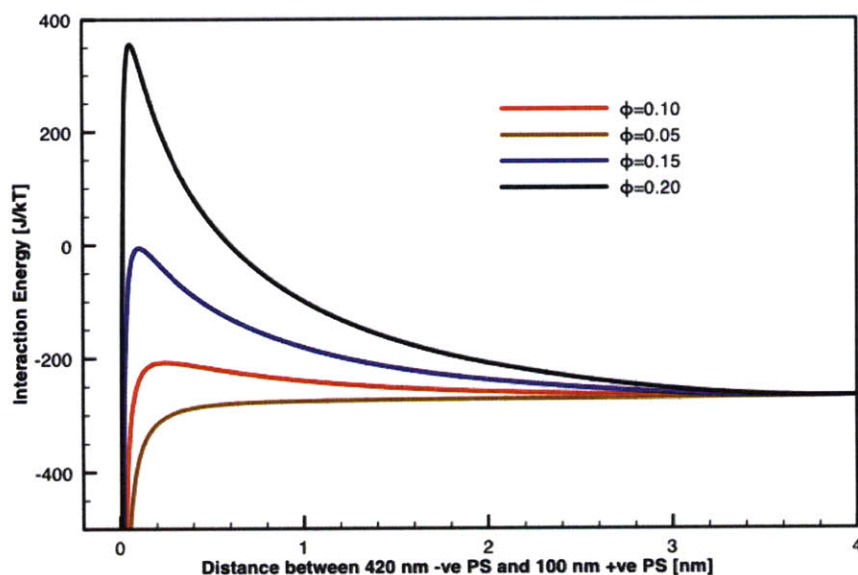


Figure 3-21: DLVO + steric interaction as a function of the adsorbed surfactant volume fraction ϕ

3.6 Colloidal Self-assembly on Charged Substrates: Role of Hydrophobicity

In this section, a discussion of colloidal self-assembly on charged surfaces is presented. In this study [156], self-assembly of negatively charged PS particles in a sessile drop, on charged substrates, was monitored in-situ. In a sessile drop, self-assembly starts from the edge of the drop and proceeds inwards.

In the absence of any surfactant in the system, if the particles and substrate are oppositely charged, the assembly of colloidal particles always results in a disordered arrangement. For instance, if the assembly takes place on negatively charged glass substrates, negatively charged PS spheres show long-range order on assembly, whereas positively charged PS particles do not. Assembly on positively charged glass substrates shows similar behavior. This behavior can be attributed to electrostatic attraction between particles and the oppositely charged substrate.

The behavior of particles is more complex when a surfactant is present in the system. Section 3.5 demonstrated that the presence of a non-ionic and amphiphilic

surfactant in a system, ensures ordered assembly of charged hydrophobic particles on a layer of oppositely charged hydrophobic particles. As shown earlier, steric hindrance prevents trapping of particles by attractive electrostatic potential. Consider a system where the substrate is hydrophilic, but the particles are hydrophobic. If the surfactant is amphiphilic and non-ionic, particle and substrate surface charges are unaffected. Surfactants adsorb onto hydrophobic particles but not on the hydrophilic substrate. Thus, there is no steric barrier between the particles and substrate. As a result, akin to ordering in a surfactant-free system, charged particles form a disordered arrangement on an oppositely charged substrate.

An interesting scenario occurs when the substrate and particles are similarly charged, and an oppositely charged surfactant is added to the system. The behavior of the particles depends on the hydrophobicity of the surfactant. For instance, in one experiment, self-assembly of negatively charged PS particles was monitored on a negatively charged substrate when (a) DTAB was present in the system and when (b) $P2VP^+I^- - PEO$ was present in the system. DTAB is a hydrophobic surfactant, whereas $P2VP^+I^- - PEO$ is an amphiphilic cationic polyelectrolyte. The mobility of PS particles in (a) was sluggish compared to the mobility of particles in (b). Additionally, domains in (b) showed long-range order compared to domains in (a). Since both surfactants are cationic, electrostatic interaction alone cannot describe the above observations. It was inferred that lower mobility in (a) is caused by attractive hydrophobic interaction between DTAB layers adsorbed on the substrate and the spheres; due to lower mobility, the particles assembled in a disordered pattern. On the other hand, adsorption of $P2VP^+I^- - PEO$ leads to a steric barrier between particles and the substrate. It was inferred that this led to greater mobility of PS particles and an ordered arrangement.

3.7 Concluding Remarks

To summarize, it was shown that oppositely charged particles can be ordered in spite of strong surface charge. A new layer-by-layer method was used to order these parti-

cles. Strong electrostatic attraction produces structures that tolerate capillary forces during drying. The final structure is stabilized by attractive electrostatic as well as van der Waals forces. It was found that a non-ionic amphiphilic surfactant, Triton-X 100, was necessary to produce long range ordering. Stable structures were obtained by spin-coating positively charged particles from solution onto a fixed substrate of negatively charged particles. By varying the concentration of particles in the suspension and the spin-speed during deposition of particles, different structures can be obtained. A model that combines the electrostatic and vdW terms, from DLVO theory, with the steric interaction term, shows that the energetic barrier to coagulation produced by steric hindrance along with the greater mobility afforded to the particles by its adsorption is consistent with our observation. As a result, it is inferred that any non-ionic amphiphilic surfactant can be used instead of Triton-X 100.

Further, it was suggested that non-close-packed zinc-blende-type structure can be made through a layer-by-layer assembly of oppositely charged particles. Non-close-packed ordering of positively charged PS on a close packed layer of negatively charged PS, was obtained through a dip-coating procedure.

Finally, ordering of like-charged colloidal particles on charged substrates was discussed. It was shown that hydrophobic attraction can lead to disordered aggregates of charged particles on like-charged surfaces when hydrophobic polyelectrolytes are used. However, use of amphiphilic polyelectrolytes can lead to the formation of ordered domains.

Chapter 4

Layer-by-Layer Self-Assembly of Non-Close-Packed Heterostructures

4.1 Introduction

In recent years, fabrication of complete photonic band gap structures has attracted a lot of attention. Presently, there are three methods that are widely used to make photonic crystals. These are: colloidal assembly [106], holographic lithography [168] and micro-machining [169]. Compared to the latter two, colloidal self-assembly is easier, cheaper and scalable [170, 171].

However, when spherical particles spontaneously assemble, the packing fraction and orientation of the crystal is limited to 0.74 and f.c.c. (111), respectively. At this packing fraction, a CPBG is not observed. Photonic band gap calculations have shown that a packing fraction of around 0.20 and a refractive index contrast of 2.5 is required to observe a CPBG. This limitation prompted researchers to look for newer strategies for making low-packing-fraction structures.

These strategies focused on using templates to direct the growth of colloidal crystals. The earliest templated colloidal crystals were fabricated by van Blaaderen et al.

[105]. By sedimenting silica particles from an aqueous dispersion (a process named “colloidal epitaxy”), they were able to grow a f.c.c. colloidal crystal with (100) orientation. Colloidal epitaxy can be used to grow crystals with other orientations too. However, it takes weeks to form a crystal through colloidal epitaxy, and the thickness of the crystal cannot be controlled. In comparison, vertical deposition methods (such as convective assembly), are best suited for use with templates, as they offer control over thickness during colloidal assembly.

Recently, Santamaria et al. [14] proposed a novel approach for making a CPBG diamond cubic crystal. They fabricated a b.c.c. crystal, composed of interpenetrating diamond cubic, silica and polymer lattices. In the end of the process, they removed the polymer particles and obtained a diamond cubic structure made of silica particles. Their approach was based on two facts. These were (i) a body centered cubic (b.c.c.) lattice is made of two interpenetrating diamond cubic lattices and (ii) a b.c.c. lattice is easier to grow since sphere sites are stable in it. Santamaria et al. used the following procedure: a silicon template with holes patterned in (110) symmetry was used to direct the assembly. By using a robot attached to a SEM, polystyrene (PS) particles were placed in alternate holes and silica particles in the remaining holes. This process was repeated particle by particle and layer by layer to make a b.c.c. crystal. In the end, PS particles were removed by etching in oxygen plasma. The silica particles that were left behind, were arranged in a diamond cubic structure. In principle, robotic assembly can be used to form any non-close-packed structure, so long as particles are in contact with one another. However, it is evident that there is a need for a more efficient and less expensive method to make non-close-packed structures.

In this chapter, templated self-assembly of an ordered 2D heterostructure of like-charged PS and silica particles is described [24, 172]. A silicon wafer with holes patterned in (100) symmetry is used as a template. Particles are arranged in the heterostructure akin to the pattern on a checkerboard; PS particles reside in every other hole and silica particles fill the remaining holes. A two-step convective assembly process is used to form this structure. In the first step, it is shown that PS particles form a sparse structure if the Debye length (κ^{-1}) of the solvent and concentration of

particles is correctly controlled. Domains with a sparse arrangement of PS particles are hundreds of micrometers large; these domains are referred to as L1-PS. In the second step, convective deposition is used to fill the remaining holes with silica particles. The resulting 2D heterostructure domains in the first layer (hereafter, referred to as L1) are tens of micrometers large.

Compared to earlier methods, this technique relies on self-assembly of charged particles to produce a sparse domain and a 2D heterostructure. By replicating the process above, layer by layer, one can create a multilayered heterostructure with two particle types. Removal of one particle type from the final heterostructure leads to a non-close-packed multilayered structure. For example, it is shown that a two-layer heterostructure of silica and PS is formed by layer-by-layer assembly. In the end of the process, PS particles are removed. This leaves behind a two-layer non-close-packed structure of silica particles.

4.2 Materials and Methods

4.2.1 Materials

Suspensions of monodisperse polystyrene (PS) beads measuring 250 nm (sulphate functionalized, $\zeta = -52.56$ mV at $\kappa^{-1} = 127$ nm, and charge density measured by the manufacturer equal to -0.019 C/m²), 140 nm (sulphate functionalized, $\zeta = -54.62$ mV at $\kappa^{-1} = 127$ nm, and charge density measured by the manufacturer equal to -0.011 C/m²) and 500 nm (sulphate functionalized, $\zeta = -61.57$ mV at $\kappa^{-1} = 127$ nm, and charge density measured by the manufacturer equal to -0.041 C/m²) were purchased from Molecular Probes Inc., Eugene, OR. Suspension of monodisperse carboxyl functionalized PS particles was also bought from the same supplier (it had $\zeta = -52.56$ mV at $\kappa^{-1} = 127$ nm, and charge density measured by the manufacturer equal to -0.032 C/m²). Monodisperse silica suspension of 250 nm particles was purchased from Corpuscular Incorporated. It had $\zeta = -45.54$ mV at $\kappa^{-1} = 127$ nm. Electrophoretic mobility for different colloidal samples was measured using a Zeta-PALS (Brookhaven

Instruments Corporation). Once electrophoretic mobility was measured, zeta potential was calculated using the Smoluchowski model (eq. 2.34). All the above suspensions were dialyzed against de-ionized (DI) water to lower their salt concentrations before use.

Poly(allylamine hydrochloride) (PAH; $M_w=50,000$) was purchased from Sigma Aldrich Inc. Polyelectrolyte solutions were prepared by thoroughly mixing appropriate amounts (1 mg/ml to 7 mg/ml) of powdered PAH in DI water.

4.2.2 Solvents

De-ionized water (DI water) was used for most of the experiments and was readily available. However, in a few cases, 99% anhydrous Ethyl Alcohol (Hubbard Hall Inc.) was used as a solvent. Ethanol-based silica suspensions were prepared via the following procedure: silica particles were centrifuged from 10 ml of their original aqueous suspension. Then they were transferred to 10 ml ethanol. The ethanol suspension was sonicated for 60 minutes. Thereafter, the particles were centrifuged again and resuspended in ethanol. Centrifuging and resuspension of the particles was repeated five times.

Conductivity of DI water was measured (YSI 3200 Conductivity Instrument) in the absence of particles, and these values were used to infer the Debye lengths. Large Debye lengths were obtained for the particle suspensions as a result of: i) dialysis of the particle suspensions (dialysis was used to lower salt concentrations in the particle suspensions). Particles were dialyzed against DI water in Float-a-lyzer dialysis bags from Spectrum Labs. These bags allow salt ions to diffuse into DI water while preventing the diffusion of particles at the same time. The salt concentration of the particle suspension was tracked by measuring the conductivity of the reference solvent, and the process continued until no further change in the conductivity of the reference solvent could be detected; and ii) low concentration of particles. Since low particle concentration was used for the experiments, the concentration of particle counter-ions was also low. Calculations showed that although the particle counter-ions led to a drop in Debye length, the Debye length in the suspension was large

enough to influence long-range interparticle interaction.

4.2.3 Template Preparation

Silicon templates with pitches = 185 nm, 330 nm or 660 nm, were prepared by interference lithography (IL). The procedure for this is outlined in section 3.2.4. These templates had holes arranged in a pattern with (100) symmetry. Fig. 4-1 is a SEM image for a template with a pitch of approximately 330 nm.

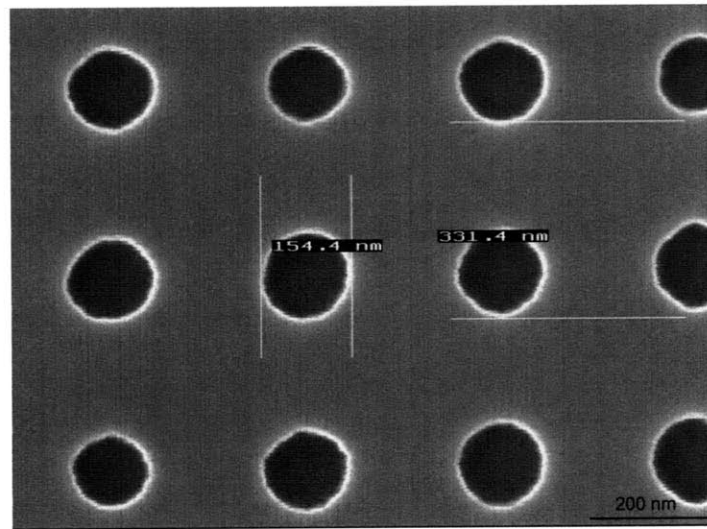


Figure 4-1: SEM image of a silicon template, which has holes arranged in a pattern with (100) symmetry. The holes were 45 nm deep. This template was created according to the procedure described in section 3.2.4

All templates had holes with a depth of 45 nm. For optimum results, the following two factors were controlled:

$$\lambda_1 = \frac{\text{Diameter of the hole}}{\text{Diameter of the particle}} \quad (4.1)$$

$$\lambda_2 = \frac{\text{Pitch of the template}}{\text{Diameter of the particle}} \quad (4.2)$$

4.2.4 Colloidal Assembly

Prior to all particle deposition steps, templates were treated with oxygen plasma at 6 mTorr for 10 seconds. Subsequent contact angle measurements showed the wetting angle of water to be between 0° and 6° . Fig. 4-2 is an image with a drop of water on a bare template. A droplet of water was placed on a bare template and it spread immediately. In fig. 4-2 the droplet is visible. Here, the contact angle was 0.80° . Particles were assembled through convective assembly. In this process, templates

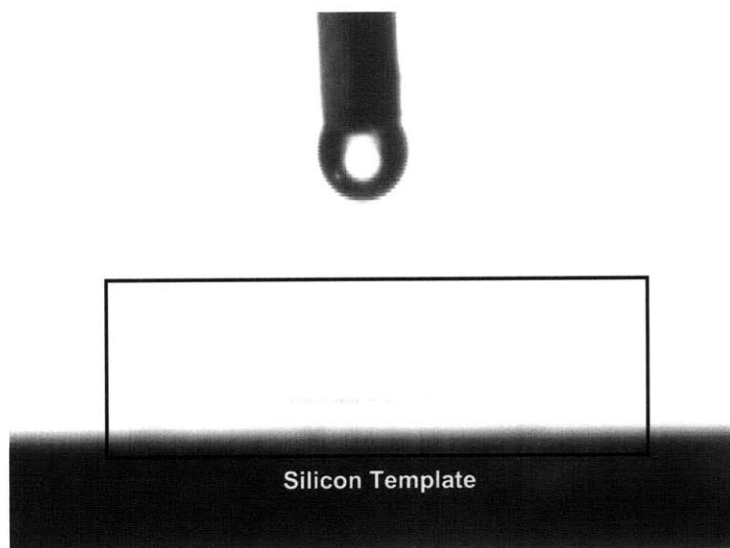


Figure 4-2: Contact angle measurement on a bare silicon template after exposure to oxygen plasma. The contact angle was 0.80° .

were attached to the side-walls of a beaker, with the particle suspension. When the suspension was slowly withdrawn, particles assembled on the template. For PS particle assembly, a 8-v/v% suspension was diluted in DI water (Debye length = 204 nm) to 0.025-v/v%. Thereafter, a beaker with PS suspension and templates, was placed in a water bath at 35°C . Silica particles were assembled as follows. A 5-v/v% aqueous suspension of silica was diluted to 0.025-v/v%. Thereafter, a beaker with this suspension and substrates, was placed in a water bath at 50°C .

Unless otherwise stated, the withdrawal speed of the suspension during all deposition steps was $46.1 \mu\text{m}/\text{min}$.

4.3 Results

4.3.1 L1-PS: Sparse Polystyrene Layer

When PS particles are assembled on a template, the final arrangement depends on the concentration of PS particles in the dispersion and the Debye length of the solvent. Fig. 4-3 is a schematic and shows the different kinds of ordering seen on the template during this work. Convective assembly of PS particles is characterized by

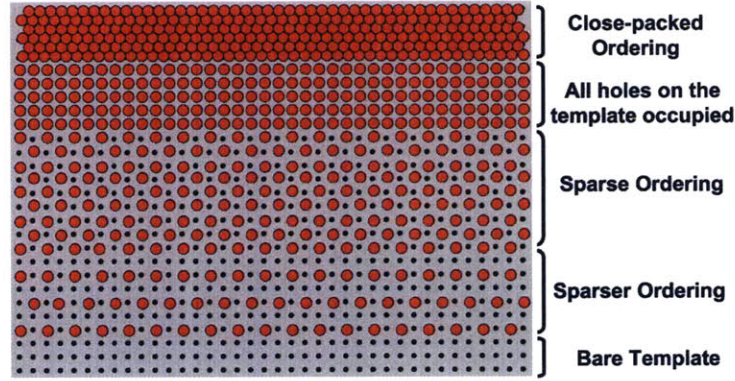


Figure 4-3: Schematic showing the different kinds of ordering seen on the template.

the formation of bands (consisting of sparse domains) separated by regions without any particles. This is shown in fig. 4-4 and is attributed to the stick and slip of meniscus on the template [173]. The effect of stick and slip is characterized through λ_{band} (eq. 4.3) and δ_{band} (eq. 4.5), whereas the extent of sparse ordering, within a band, is characterized through ϕ_{sparse} (eq. 4.4):

$$\lambda_{band} = \text{Average center-to-center distance between two bands.} \quad (4.3)$$

$$\phi_{sparse} = \text{Average area of a band, which is occupied by the sparse pattern.} \quad (4.4)$$

$$\delta_{band} = \text{Average width of a band.} \quad (4.5)$$

Fig. 4-5, fig. 4-6 and fig. 4-7 show scanning electron microscope (SEM) images of the final arrangement of PS particles on the template when the Debye length was fixed at 204 nm and the concentration of particles was 0.01-v/v% , 0.025-v/v% and

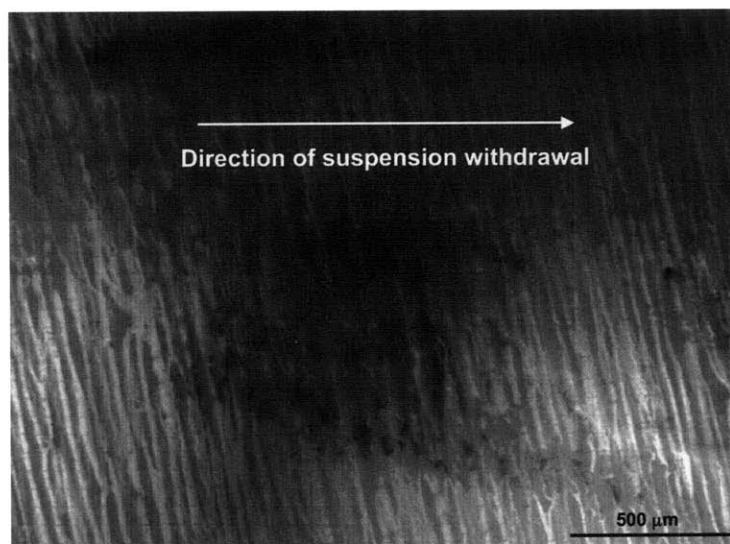


Figure 4-4: SEM image of a template after convective assembly of PS particles from a 0.025-v/v% aqueous suspension. Due to stick and slip of the meniscus, the particles assemble in bands, separated by regions on the template without any particles. In this image, bright regions are bands of PS particles, whereas dark regions are regions on the template without any particles

0.10-v/v%, respectively. Insets in these figures schematically show the arrangement of PS particles on the template. In these insets, PS particles on holes are shown in red and the empty holes are shown as open circles. The pair distribution function (PDF) for the arrangement of PS particles in the SEM images above, are plotted in fig. 4-8 and fig. 4-9 respectively. Fig. 4-10 is a SEM image, showing the side view of a template with L1-PS arrangement. Fig. 4-11 is a SEM image showing the arrangement of PS particles when the Debye length was 30 nm; concentration of particles for this experiment was 0.025-v/v%. The PDF for the arrangement of PS particles in fig. 4-11 is plotted in fig. 4-12. λ_{band} , ϕ_{sparse} , and δ_{band} for the above experiments are summarized in table 4.1:

When 0.1-v/v% suspension was used, an increase in polydispersity led to the formation of close-packed domains. In contrast, at lower concentrations (0.01-v/v% and 0.025-v/v%) the assembled pattern withstood larger fluctuations in dispersity and retained the sparse pattern. However, even at these concentrations, a few domains with close-packed order, and with PS particles occupying all holes on the template, were

Table 4.1: Variation in λ_{band} , ϕ_{sparse} , and δ_{band} at different Debye lengths and concentrations for 250 nm PS particles

κ^{-1}	concentration	λ_{band} [μm]	ϕ_{sparse}	δ_{band} [μm]
204nm	0.025-v/v%	27.6 ± 13.24	0.90 ± 0.10	15.2 ± 7.5
204nm	0.01-v/v%	40.1 ± 20.12	0.91 ± 0.06	8.0 ± 3.4
30nm	0.025-v/v%	25.1 ± 12.39	0.19 ± 0.09	14.9 ± 7.6



Figure 4-5: SEM image of a template, after convective assembly of 250 nm PS particles from a 0.01-v/v% aqueous suspension. The withdrawal speed of the suspension was $46.1 \mu m/min$ at $35^\circ C$. κ^{-1} was 204 nm. This was inferred from conductivity measurement of the solvent. As seen in this image, particles arrange in a sparse pattern. The inset shows a schematic arrangement of particles on the template: red circles denote particles and open circles denote empty holes. Due to the low concentration of the particles in suspension, narrow bands of PS particles assemble on the template.

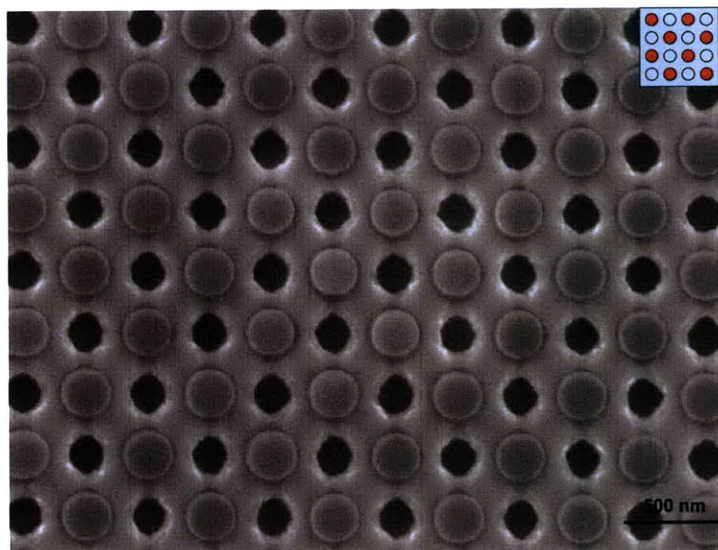


Figure 4-6: SEM image of a template, after convective assembly of 250 nm PS particles from a 0.025-v/v% aqueous suspension. The withdrawal speed of the suspension was $46.1 \mu\text{m}/\text{min}$ at 35°C . κ^{-1} was 204 nm. This was inferred from conductivity measurement of the solvent. As seen in this image, particles arrange in a sparse pattern. The inset shows a schematic arrangement of particles on the template: red circles denote particles on holes and open circles denote empty holes.

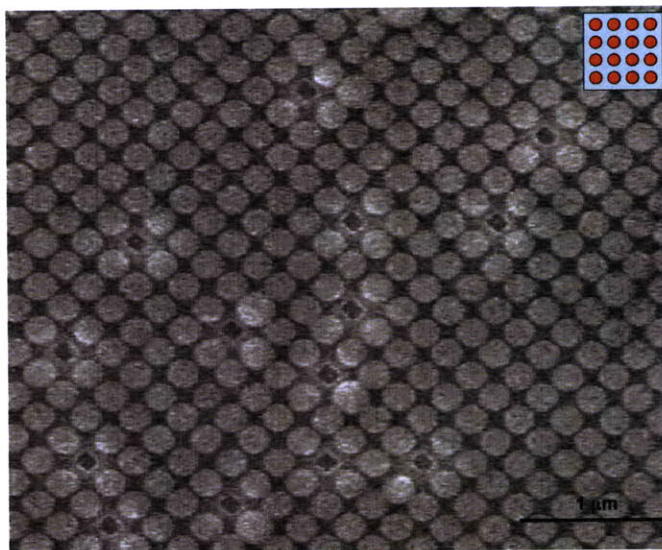


Figure 4-7: SEM image of a template after convective assembly of 250 nm PS particles from a 0.1-v/v% aqueous suspension. The withdrawal speed of the suspension was $46.1 \mu\text{m}/\text{min}$ at 35°C . κ^{-1} was 204 nm. This was inferred from conductivity measurement of the solvent. Due to high concentration of PS particles in the suspension, they fill all the holes in the template. The inset shows a schematic arrangement of particles on the template. Red circles denote PS particles on holes.

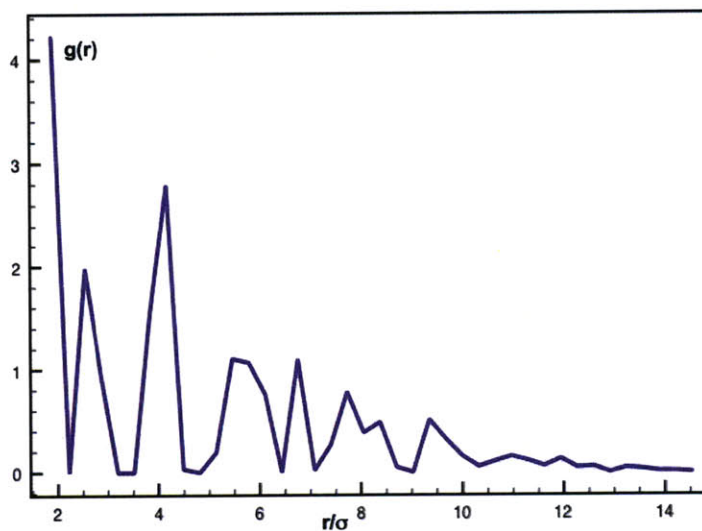


Figure 4-8: Plot of the pair distribution function for the arrangement of 250 nm PS particles in fig. 4-5 and fig. 4-6. σ is the diameter of the sphere

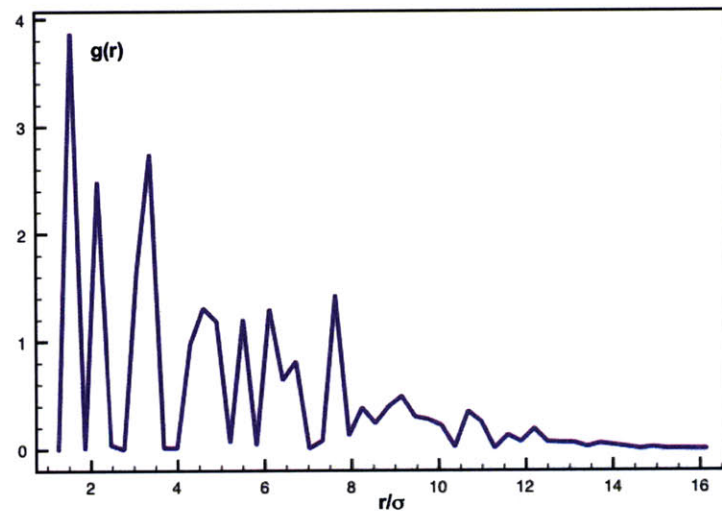


Figure 4-9: Plot of the pair distribution function for the arrangement of 250 nm PS particles in fig. 4-7. σ is the diameter of the sphere

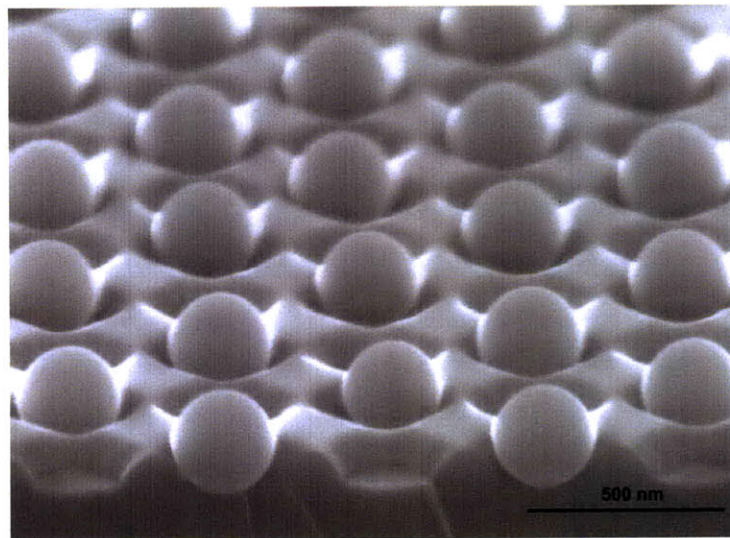


Figure 4-10: SEM image of the cross-section of a template with 250 nm PS particles ordered in L1-PS arrangement

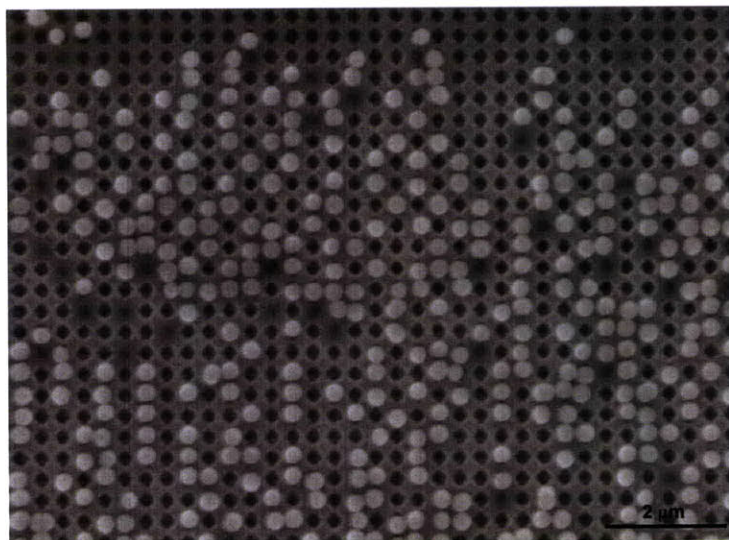


Figure 4-11: SEM image after convective assembly of 250 nm PS particles from a 0.025-v/v% aqueous suspension. The withdrawal speed of the suspension was 46.1 $\mu\text{m}/\text{min}$ at 35°C. κ^{-1} was 30 nm. This was inferred from conductivity measurement of the solvent. Random filling may be associated with the reduced Debye length.

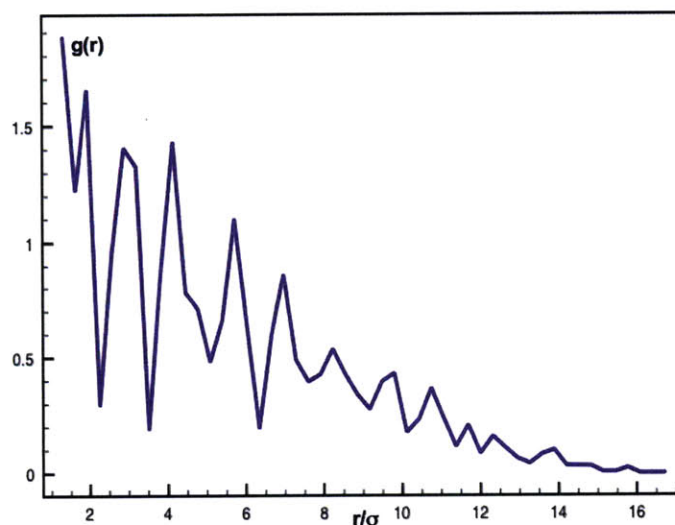


Figure 4-12: Plot of the pair distribution function for the arrangement of 250 nm PS particles in fig. 4-11. σ is the diameter of the sphere. Due to low κ^{-1} , the arrangement shows short-range order compared to the arrangement of particles in fig. 4-6

observed. In general, the number of close-packed domains and their size, decreased on lowering the concentration of particles. Due to stick and slip of the meniscus, the domains with sparse order were bigger, perpendicular to the direction of withdrawal of the suspension. Thus, typical L1-PS domains were $15\mu\text{m}$ wide along the pumping direction, and hundreds of micrometers large, perpendicular to the direction of withdrawal of the suspension. A SEM image of a typical L1-PS domain is shown in fig. 4-13.

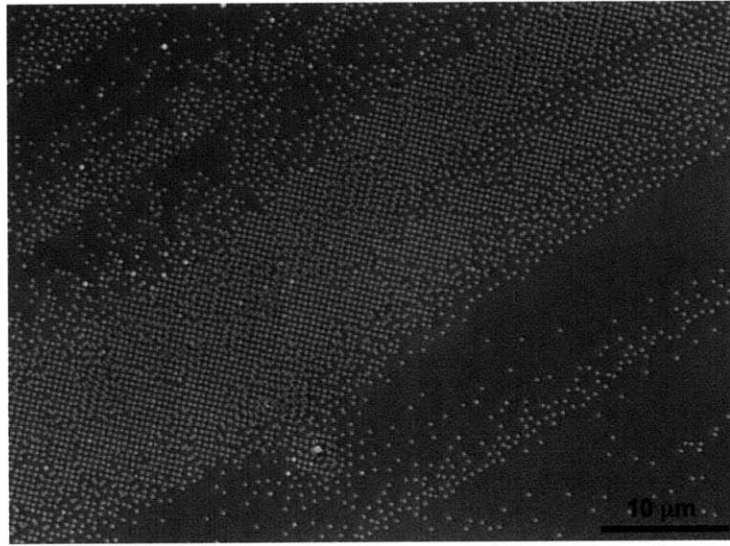


Figure 4-13: SEM image of a large area of the template after convective assembly of 250 nm PS particles from their 0.025-v/v% aqueous suspension. The withdrawal speed of the suspension was $46.1\mu\text{m}/\text{min}$ at 35°C . κ^{-1} was 204 nm. This was inferred from conductivity measurement of solvent. This image shows a L1-PS band where PS particles are arranged akin to their arrangement in fig. 4-6. Thus, typical L1-PS domains were $15\mu\text{m}$ wide along the direction of withdrawal of the suspension and hundreds of μm large, perpendicular to it.

4.3.2 Results and Discussion: Mechanism of Sparse Structure Formation

Orientation of the template during convective assembly plays a key role in the formation of the sparse structure. In a set of experiments, the template was fixed such that the holes are oriented along (100), (110) and (120), relative to the direction of

withdrawal of the suspension. Results from these experiments are shown in fig. 4-14 and fig. 4-15. Fig. 4-14 is a plot of δ_{band} and λ_{band} , and fig. 4-15 is a plot of ϕ_{sparse} for

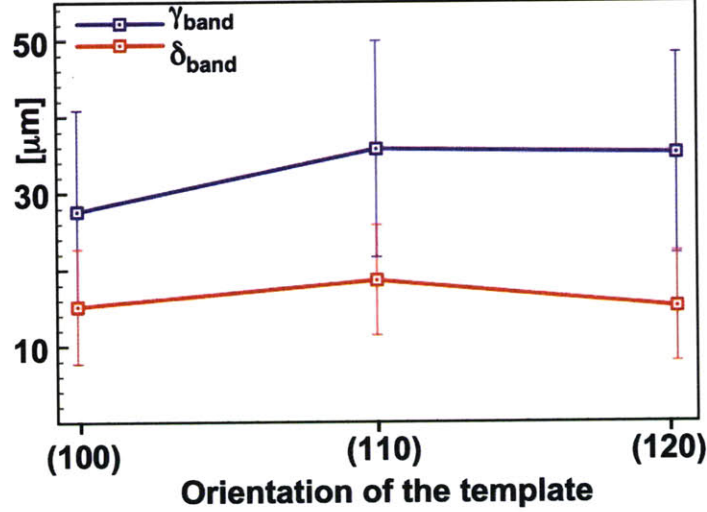


Figure 4-14: Variation of λ_{band} and δ_{band} when PS particles were assembled onto templates, fixed at different orientations relative to the direction of withdrawal of the suspension. The suspension was withdrawn at $46.1\mu\text{m}/\text{min}$ at 35°C .

different orientations. Fig. 4-15 shows that ϕ_{sparse} is larger if the template is oriented along high-symmetry directions ((110) and (100)), with respect to the direction of withdrawal of the suspension. When the template is oriented along a high-symmetry direction, such as (100), holes on the template are oriented parallel to the meniscus. On the other hand, when the template is oriented along a low-symmetry direction, such as (120), the holes are not oriented parallel to the meniscus. This may indicate that PS particles are stabilized in a non-close-packed pattern at the three-phase line (i.e. the meniscus), prior to their deposition on the template. It is shown later that this is due to electrostatic repulsion between particles.

4.3.3 Discussion: Conditions for Sparse Structure Formation

Dependence of the final arrangement of particles can be interpreted with the following ratio, λ_3 . This is given by eq. 4.6.

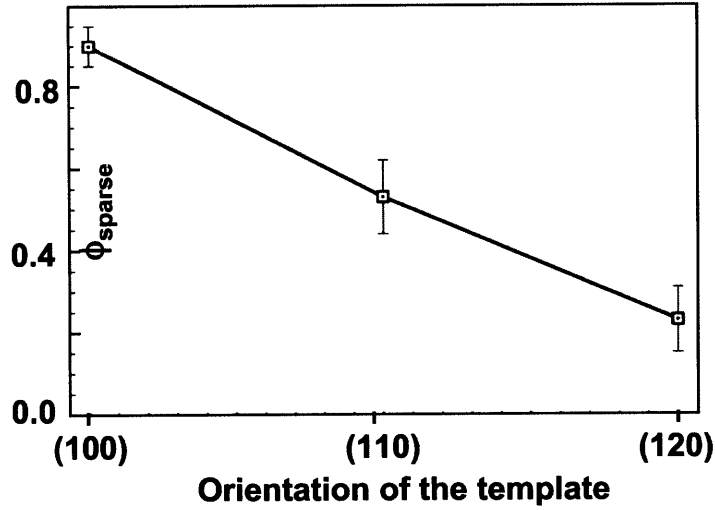


Figure 4-15: Variation of ϕ_{sparse} when PS particles were assembled onto templates, fixed at different orientations relative to the direction of withdrawal of the suspension. The suspension was withdrawn at $46.1\mu m/min$ at $35^\circ C$.

$$\lambda_3 = \frac{\text{Diameter of the particle}}{\text{Debye length of the solvent}}. \quad (4.6)$$

It was verified that formation of sparse PS domains is not restricted to 250 nm sized particles. In fact, sparse domains were observed when 140 nm and 500 nm PS particles were assembled on their respective templates at $35^\circ C$. The Debye length was 204 nm and the concentration of PS particles in the dispersion was 0.025-v/v% for both experiments. When $\kappa^{-1} = 204$ nm, λ_3 is 0.408 in a dispersion of 500 nm particles, whereas it is 0.816 for 250 nm particles and 1.46 for 140 nm particles.

Detailed Monte Carlo simulations, discussed in chapter 6, show that the concentration of particles and κ^{-1} play a central role in the formation of domains with sparse arrangement of particles. Besides these two, the other parameters that were controlled for obtaining large domains with sparse ordering are briefly discussed below.

Hydrophobicity

Surface treatment of starting templates played a key role during convective deposition. When the surface of the template was hydrophobic, the meniscus at the air-water interface had a higher concentration of particles. As a result, multiple layers assembled during deposition. On the other hand, when the surface was super-hydrophilic (wetting angle for water $\approx 0^\circ$), a monolayer of particles assembled. Common methods to make the template super-hydrophilic are, treatment with Pirhana (3:1 mixture of sulphuric acid and hydrogen peroxide respectively) or exposure to oxygen plasma. Plasma treatment was used instead of the Pirhana treatment because of its effectiveness and handling.

Withdrawal Rate of the Suspension

The largest bands of sparsely ordered PS particles were obtained when withdrawal speed was $46.1 \mu\text{m}/\text{min}$. At faster speeds, narrower bands with sparse order were observed, whereas at a slower speed ($23.3 \mu\text{m}/\text{min}$) wider bands with low ϕ_{sparse} were observed. The most likely explanation for this is the variation in concentration at different withdrawal speeds. When the withdrawal speed is slow, more particles migrate to the air-water interface. As a result, dense packing of particles is more likely. On the other hand, at high withdrawal speeds, a monolayer is formed because fewer particles migrate to the air-water interface. These results are summarized in table 4.2.

Table 4.2: Formation of the sparse structure at different speeds of withdrawal of the suspension

Speed of withdrawal of the suspension [$\mu\text{m}/\text{min}$]	$\lambda_{\text{band}} [\mu\text{m}]$	ϕ_{sparse}	$\delta_{\text{band}} [\mu\text{m}]$
46.1	27.6 ± 13.24	0.90 ± 0.10	15.2 ± 7.5
23.3	12.67 ± 6.33	0.60 ± 0.09	21.2 ± 5.2

4.3.4 L1-Silica

L1-PS was used as the starting substrate for deposition of silica particles. Before deposition, L1-PS was exposed to oxygen plasma for 10 seconds. Contact angle measurements showed that the surface is hydrophilic, with a wetting angle between 0° and 6° . As previously discussed, a super-hydrophilic surface is required for assembling a monolayer through convective assembly. Fig. 4-16 is an image of a drop of water on a L1-PS substrate, after exposure to oxygen plasma. The droplet spread immediately on coming in contact with the substrate. However, it is visible in fig. 4-16. The contact angle for this experiment was 4.7° .

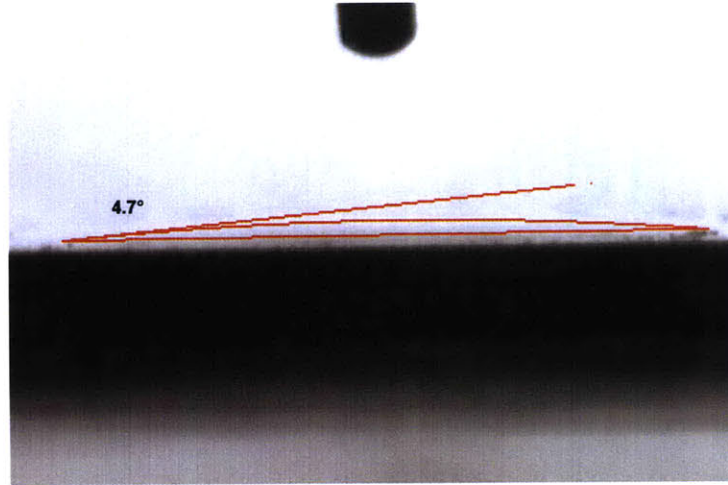


Figure 4-16: Contact angle measurement on L1-PS substrate, after it was exposed to oxygen plasma for 10 seconds. The contact angle of water was 4.7°

Silica particles were deposited from a 0.025-v/v% suspension at $46.1 \mu\text{m}/\text{min}$ and 50°C . The arrangement of these particles is also characterized by the formation of bands. Thus, bands with silica particles, arranged in a sparse pattern (hereafter, referred to as L1-silica) were separated by regions without silica particles.

When the assembly was carried out at 35°C , silica particles occupied fewer holes on the substrate. This could have been due to the higher sedimentation of silica particles. Various methods have been used to reduce sedimentation. Most researchers

use silica dispersion in ethanol instead of DI water [127]. Since ethanol is more volatile than water, a greater number of silica particles are transported to the meniscus. Other researchers prefer to assemble silica particles on a horizontal template, using gravitational force to their advantage [2]. In the present set-up, ethanol is not an appropriate dispersion medium because PS particles are partially soluble in ethanol and become inflated. For instance, fig. 4-17 is a SEM image and shows inflated PS particles (≈ 350 nm) that were originally 250 nm in diameter. These were exposed to ethanol during deposition of silica particles from a silica dispersion in ethanol. Assembly on a horizontal template is also not preferable because the thickness of the final structure cannot be controlled, unlike in vertical deposition. The preferred approach is to assemble particles from their aqueous dispersion at 50°C . During this process, the beaker was partially immersed in a water bath at 50°C . This created convective currents that transported more particles to the meniscus and reduced the effect of sedimentation.

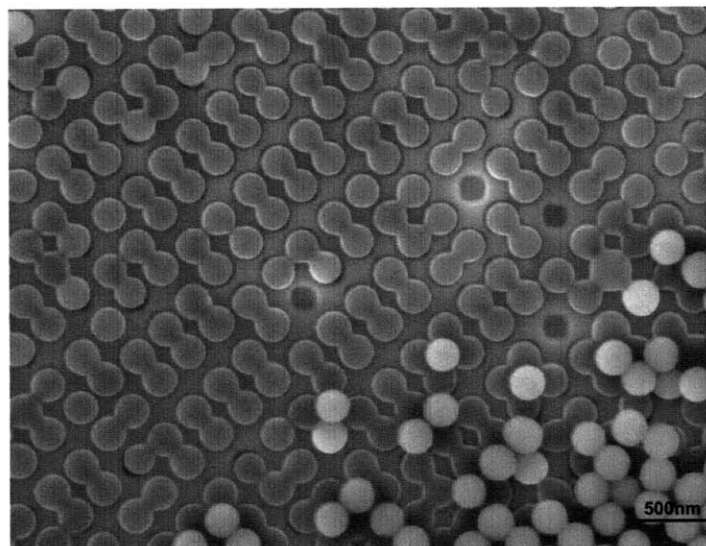


Figure 4-17: SEM image of a template with 250 nm PS particles arranged on the template. This image was taken after silica particles were assembled from a 0.025-v/v% ethanol suspension, on a substrate with 250 nm PS particles arranged on the template. PS particles are partially soluble in ethanol. As a result, they swell to 350 nm and coalesce

Fig. 4-18 is a SEM image showing bright silica particles and dull PS particles,

ordered in the first layer. The contrast was a result of different material composition of these particles. Fig. 4-19 is a SEM image showing a larger area of the first layer. Note that bands of silica particles only partially overlap with bands of PS particles. As a result, L1 domains were smaller than L1-PS domains. Typically, $\lambda_{silica-bands}$ was $26.1 \mu m$, ϕ_{L1} was 0.70 and $\delta_{silica-bands}$ was $8.74 \mu m$. This is the

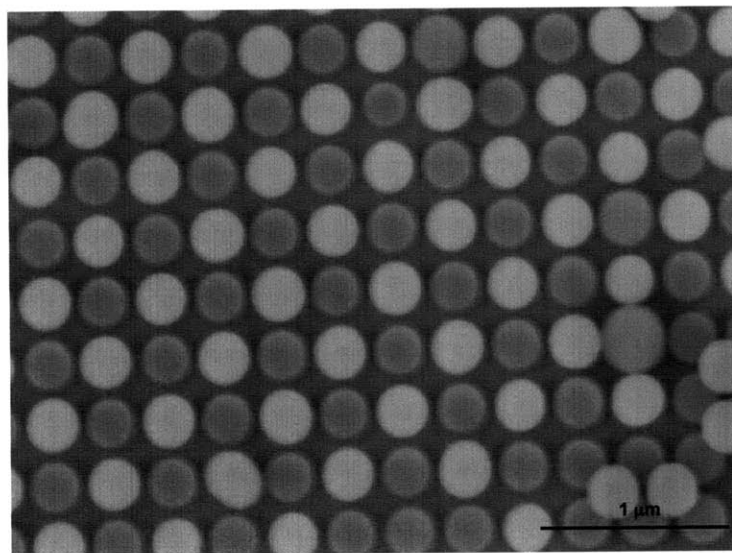


Figure 4-18: SEM image showing the arrangement of 250 nm silica and PS particles, after silica particles were assembled from a 0.025-v/v% aqueous suspension, at $50^{\circ}C$, on L1-PS substrate. The speed of withdrawal of the suspension was $46.1 \mu m/min$. This kind of order is referred to as L1. PS particles appear dark and silica particles appear bright. The contrast is due to different material composition

first experimental demonstration of self-assembly being used to form a 2D non-close-packed heterostructure. The structure was formed on a template and stabilized by repulsive electrostatic interaction between particles. Ionic colloidal crystals (ICCs) are non-close-packed structures too. However, they collapse into a close-packed or disordered structure on removal of the solvent.

By controlling the repulsive electrostatic potential between particles, multiple structures can be nucleated on a template. For instance, fig. 4-20 shows a SEM image, where PS particles formed a sparser structure. This structure were stabilized when concentration of PS particles was 0.01-v/v% and $\lambda_3 \approx 1.0$ *. The empty sites

*In this structure, second nearest neighbors are separated by 737.9 nm. Even at this distance, and

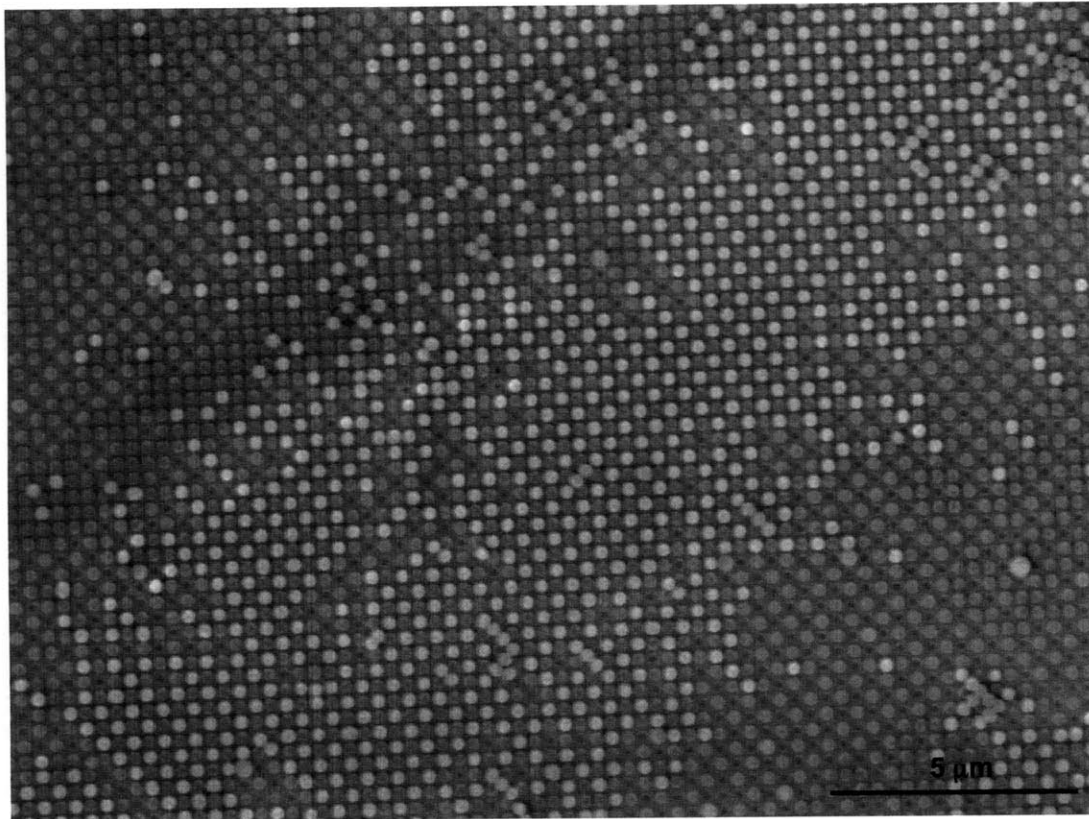


Figure 4-19: SEM image of a large area with L1 ordering. This region is made of dark 250 nm PS particles arranged in every other hole and bright 250 nm silica particles filling the remaining holes. The contrast is due to different material composition. Typical bands with L1 order were 8 μm wide along the direction of withdrawal of the suspension, and tens of micrometers large, perpendicular to it

were filled in the second step with silica particles. Fig. 4-21 is a SEM image taken after silica particles were deposited in the second step.

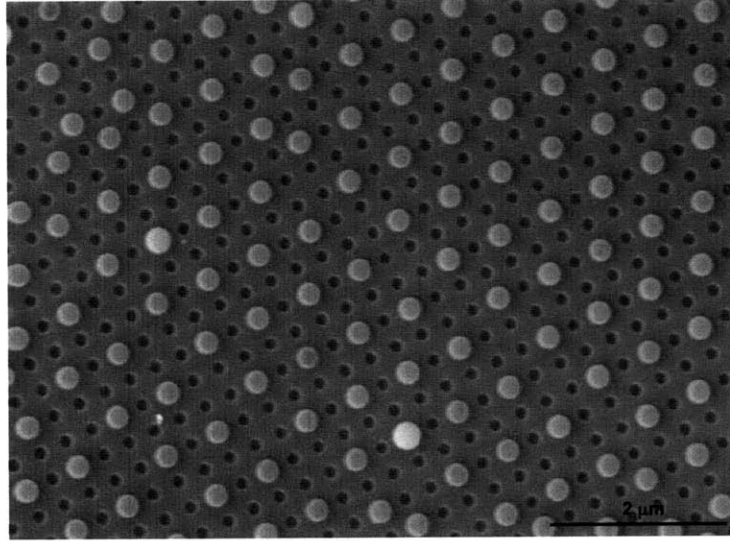


Figure 4-20: SEM image of a template after convective assembly of 250 nm PS particles from their 0.01- $v/v\%$ aqueous suspension. The withdrawal speed of the suspension was 46.1 $\mu\text{m}/\text{min}$ at 35°C and κ^{-1} was 250 nm. This was inferred from conductivity measurement of the solvent. Due to low concentration of PS particles in the suspension and due to high κ^{-1} , sparser pattern was stabilized by electrostatic repulsion between particles

Formation of sparse structures is not restricted to the present template. Templates with other geometries can be used to nucleate different 2D heterostructures. Fabrication of a stable 2D heterostructure is the key to 3D assembly of non-close-packed colloidal architectures. In the present study, a two-layer non-close-packed heterostructure was made by layer-by-layer assembly of the 2D heterostructure described in section 4.3.3. Similar to the formation of L1, the formation of the heterostructure in the second layer (L2) was a two-step process. In the first step, PS particles formed a sparse pattern on L1. This pattern is referred to as L2-PS. In the next step, unoccupied sites in L2-PS were filled with silica particles.

$\kappa^{-1} = 250$ nm, electrostatic interaction energy is approximately $2370k_B T$ and may be responsible for stabilizing this structure.

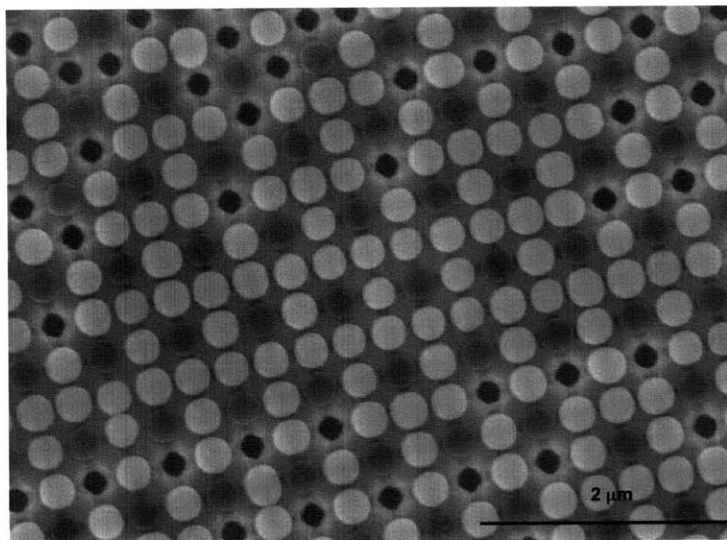


Figure 4-21: SEM image of 250 nm bright silica particles and 250 nm dark PS particles arranged on a template. Silica particles were deposited on a template with PS particles arranged in a sparser pattern, shown in fig. 4-20. Silica particles were deposited from a 0.025-v/v% aqueous suspension at 50°C. The suspension was withdrawn at 46.1 $\mu\text{m}/\text{min}$

4.3.5 L2-PS

In the second layer, sparse domains of PS particles were smaller than sparse domains in the first layer. As before, deposition of PS particles was preceded by a 10-second exposure to oxygen plasma. A 0.025-v/v% aqueous suspension of PS particles was used for deposition; Debye length in the suspension was 204 nm. Due to stick and slip of the meniscus, the deposition was characterized by the formation of bands of PS particles, separated by regions without particles. Typically, these bands were 5 μm wide. Fig. 4-22 is a SEM image of a band of PS particles in the second layer. Fig. 4-23 is a SEM image showing a smaller region with L2-PS ordering. For clarity, PS particles in L2-PS (in fig. 4-23) are colored in bright green. The colored image is shown in fig. 4-24. Dull green circles represent vacant L2-PS sites.

When the PS suspension was withdrawn at 46.1 $\mu\text{m}/\text{min}$, L2-PS domains were only a few particles large. Larger L2-PS domains were observed when the suspension was withdrawn at 23.3 $\mu\text{m}/\text{min}$. Further reduction in the withdrawal rate led to the

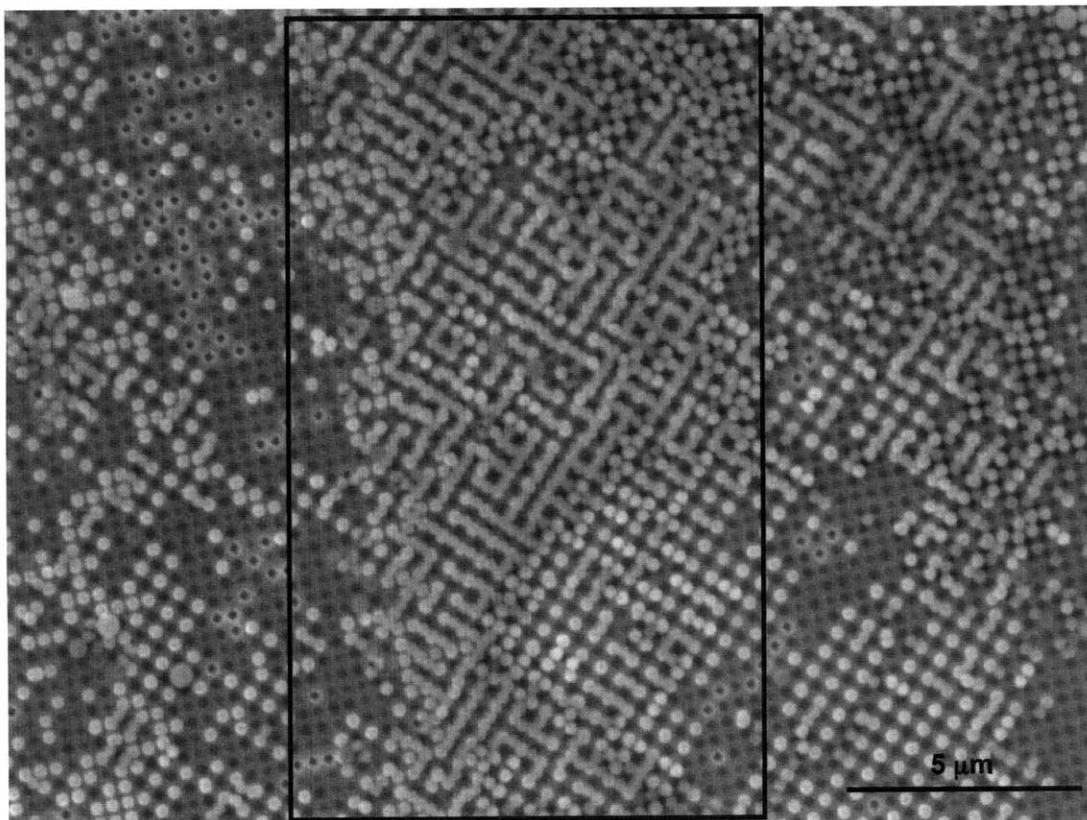


Figure 4-22: SEM image of a large area with 250 nm PS particles arranged in a sparse pattern in the second layer. The underlying first layer had L1 order. PS particles were deposited from a 0.025-v/v% aqueous suspension at 23.3 $\mu\text{m}/\text{min}$ and 35°C, through convective assembly. Typical bands with L2-PS order were 5 μm wide.

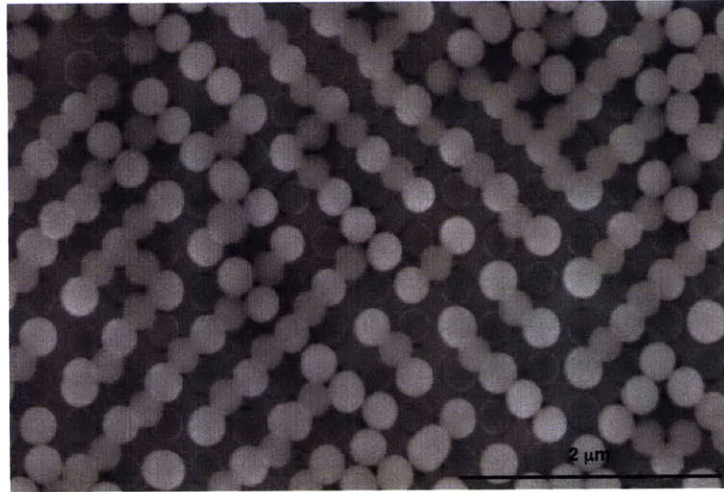


Figure 4-23: SEM image of a region with 250 nm PS particles arranged in a sparse pattern on the second layer. The underlying, first layer had L1 order. PS particles were deposited from a 0.025-v/v% aqueous suspension at 23.3 $\mu\text{m}/\text{min}$ and 35°C, through convective assembly

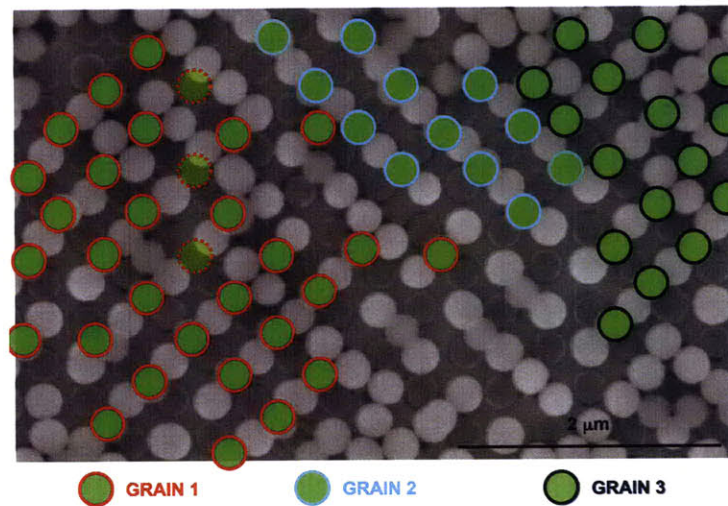


Figure 4-24: PS particles in L2-PS in fig. 4-23, are colored in green. Dull green discs denote vacancies, whereas bright green discs denote PS particles. Here, L2-PS domain is made of three L2-PS grains. These are represented by coloring the rim of the discs differently. Discs with identically colored rims belong to the same grain

formation of close-packed bands without affecting the size of sparsely packed L2-PS domains. Interestingly, larger regions of sparse L2-PS domains were observed when the underlying layer was made solely of PS particles. Fig. 4-25 is a SEM image showing sparsely ordered PS particles arranged on a first layer of PS particles.

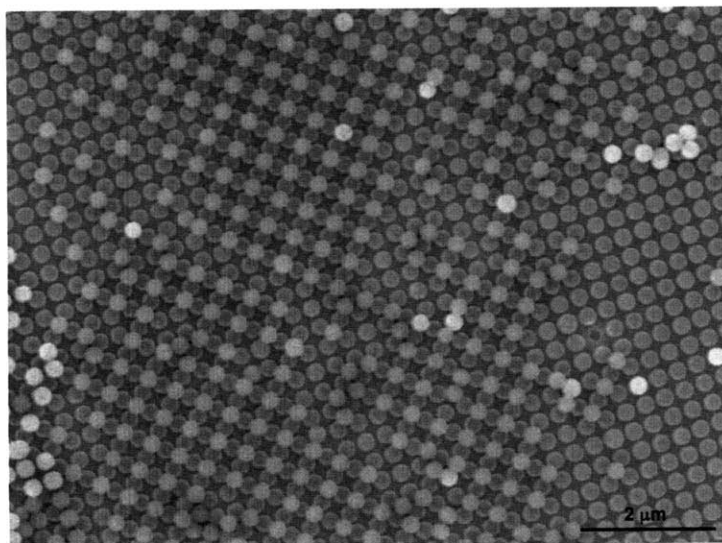


Figure 4-25: SEM image of a region with 250 nm PS particles arranged in a sparse pattern in the second layer. In the first layer PS particles occupy all the holes. Larger domains of PS particles with sparse ordering were observed when the underlying layer was made solely of PS particles. Here, PS particles were deposited in the second layer from a 0.025-v/v% aqueous suspension at 23.3 $\mu\text{m}/\text{min}$ and 35°C, through convective assembly

4.3.6 L2-Silica

After deposition of PS, the substrate was exposed to oxygen plasma for 10 seconds. Thereafter, silica particles were deposited through convective assembly. Due to stick and slip, the deposition was characterized by the formation of bands along the direction of withdrawal. However, there was negligible overlap between L2-PS and bands with sparsely ordered silica particles (hereafter, referred to as L2-silica). It was found that a reduction in the electrostatic repulsion between particles plays a key role in increasing the overlap of L2-silica with L2-PS. In addition, relative humidity (RH)

was also varied but had negligible effect on the overlap between L2-PS and L2-silica bands. Details of these experiments are discussed below.

Electrostatic Interaction

During deposition of silica, the suspension was maintained at 50°C and withdrawal speed was 46.1 μm/min. The interaction potential between the substrate and silica particles in the suspension was repulsive, as all the particles were negatively charged. It was modified as follows:

(i) Ionicity in the suspension: Ionicity was modified by changing the concentration of sodium chloride (NaCl) in the suspension. However, even at moderate (1.6×10^{-5} M) and high (10^{-4} M) ionicity, overlap of L2-silica and L2-PS bands was negligible.

(ii) Charge on the substrate: The charge on the substrate was modified by dip-coating the substrate with a cationic polyelectrolyte. Researchers have often used layer-by-layer assembly of polyelectrolyte on a layer of assembled colloids [174], to reduce or reverse the surface charge. In the current study, Poly(allylamine hydrochloride) (PAH) was used to reduce the surface charge. Although I had no means to quantify the variation of surface charge, larger regions of overlap between L2-PS and L2-silica bands were observed after longer exposure to PAH. Larger regions of overlap were also observed when denser suspensions of PAH were used during dip-coating. This may have led to greater reduction of the surface charge by adsorption of PAH.

Dipping in PAH was carried out by changing the dipping time in PAH (at constant PAH concentration) and by changing the concentration of PAH (at constant dipping time). Table 4.3 summarizes these values.

Table 4.3: Summary of Dip-coating in PAH

Concentration of PAH in the suspension [mg/ml]	Dipping time in PAH suspension [minutes]
1	5
1	10
3	5
7	5

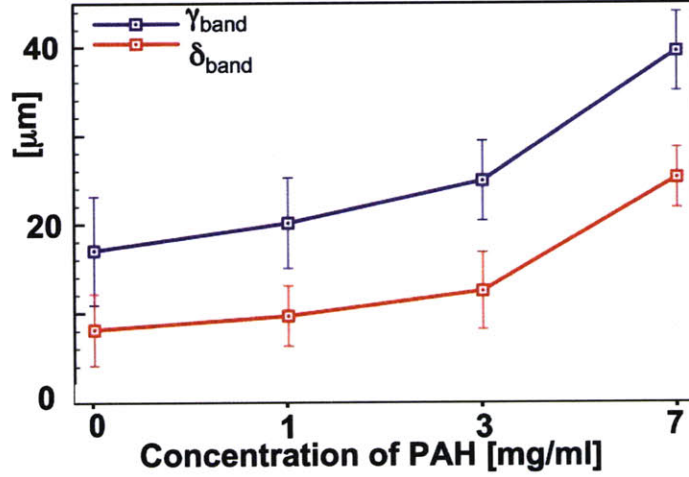


Figure 4-26: Variation of $\lambda_{\text{silica-band}}$ and $\delta_{\text{silica-band}}$ for silica particles after dip-coating in different suspensions of PAH

Fig 4-26 shows the variation in $\lambda_{\text{silica-band}}$ and $\delta_{\text{silica-band}}$, and fig. 4-27 shows the variation of ϕ_{L2} on changing the dipping conditions in PAH. According to fig. 4-27, ϕ_{L2} is zero until the samples were dipped in PAH. When samples were dipped in 1 mg/ml PAH suspension, small regions with L2 order ($\phi_{L2} = 0.05$) were observed; larger $\delta_{\text{silica-band}}$ was also observed. Fig. 4-28 is a SEM image showing a substrate that was dipped for 10 minutes in a 1 mg/ml suspension of PAH, followed by the assembly of silica particles. For better visual contrast, silica and PS particles in the second layer are colored red and green, respectively. The colored image is shown in fig. 4-29. However, according to fig 4-26, largest regions with L2 order were observed when samples were dipped in 3 mg/ml suspension of PAH for 5 minutes, followed by silica deposition ($\phi_{L2} = 0.19$). Fig. 4-30 is a SEM image and shows a region of overlap, L2, which has been circled. For better visual contrast, silica and PS particles in the second layer are colored red and green, respectively. The colored image is shown in fig. 4-31.

When silica particles were deposited on substrates that were dipped in 7 mg/ml suspension of PAH for 5 minutes, many silica particles were perched on top of the underlying PS particles. This is shown in fig. 4-32. Enclosed in the box, is a

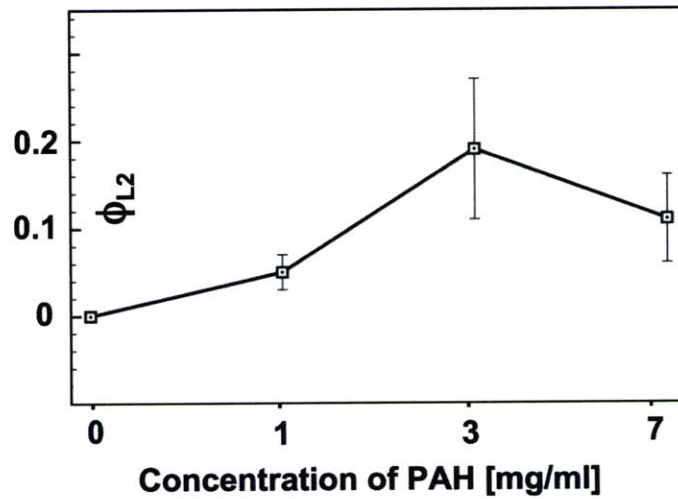


Figure 4-27: Variation of ϕ_{L2} after dip-coating in different suspensions of PAH

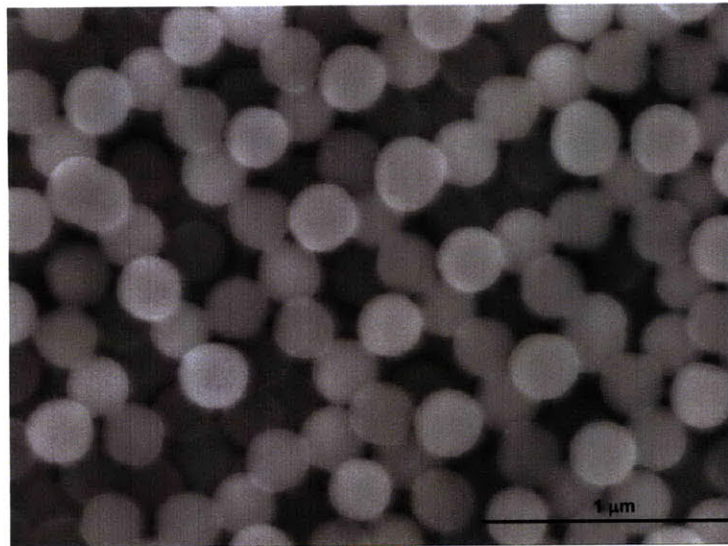


Figure 4-28: SEM image after 250 nm silica particles were deposited in the second layer, from a 0.025-v/v% aqueous suspension at 50°C and 46.1 $\mu\text{m}/\text{min}$, through convective assembly. Prior to silica deposition, the substrate was dipped in 1 mg/ml suspension of PAH for 10 minutes

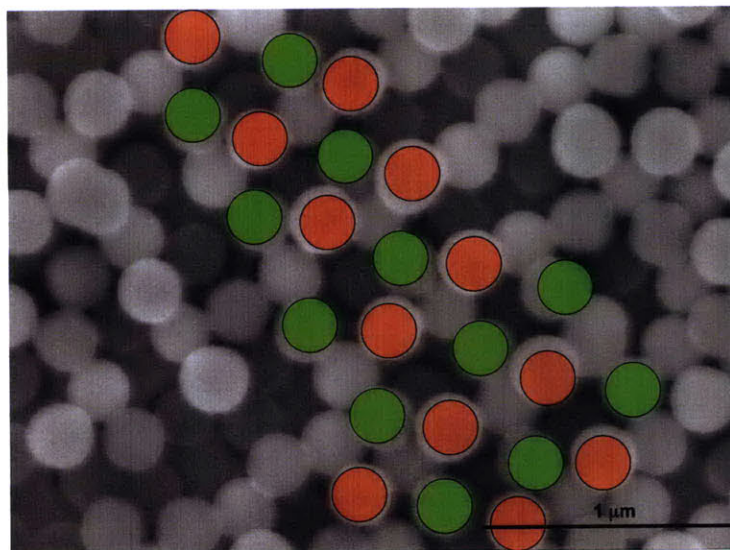


Figure 4-29: Identical SEM image to fig. 4-28. PS particles in the second layer are colored green and silica particles in the second layer are colored red, for better visual contrast. The colored particles form a L2 domain

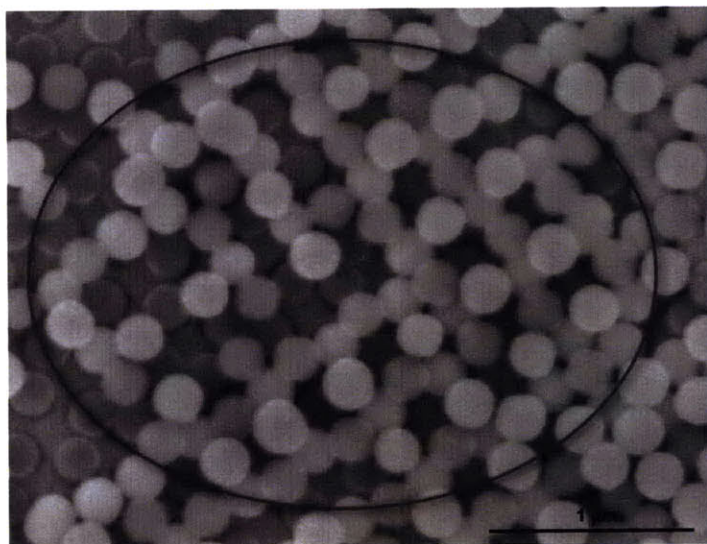


Figure 4-30: SEM image after 250 nm silica particles were deposited in the second layer, from a 0.025-v/v% aqueous suspension at 50°C and 46.1 $\mu\text{m}/\text{min}$, through convective assembly. Prior to silica deposition, the substrate was dipped in 3 mg/ml suspension of PAH for 5 minutes

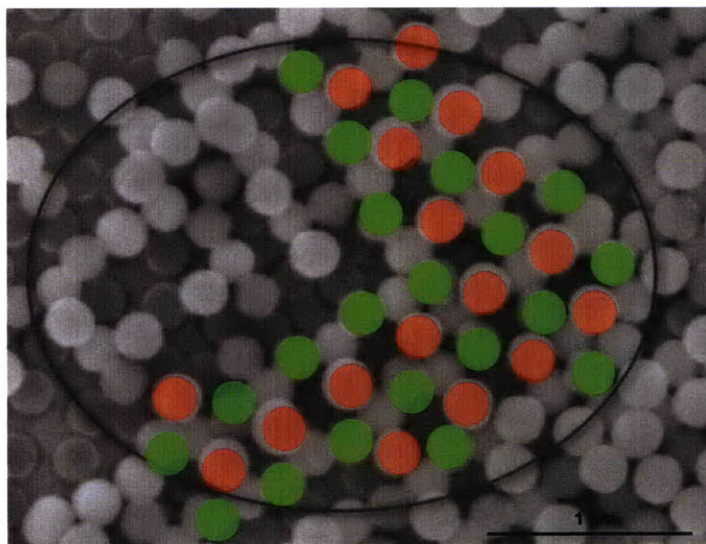


Figure 4-31: Identical SEM image to fig. 4-30. PS particles in the second layer are colored green and silica particles in the second layer are colored red, for better visual contrast. The colored particles form a L2 domain

silica particle perched on a PS particle. This kind of arrangement may indicate that the surface charge of the substrate was reversed. According to fig. 4-26 this is accompanied by the formation of larger bands (typically $\delta_{silica-bands} = 25.19\mu m$ and $\phi_{L2} = 0.11$).

Relative Humidity (RH) and Hydrophobicity

Researchers have found that stick and slip of the meniscus can be reduced by using a super-hydrophilic template [143]. Indeed, before every deposition step, the substrate was exposed to oxygen plasma for 10 seconds. In addition, the following conditions were used.

In one set-up, carboxyl-functionalized PS particles were used for L1-PS and L2-PS steps, instead of sulphate-functionalized PS particles. Although both are negatively charged, carboxyl-functionalized particles are hydrophilic. Consequently, stick and slip of the meniscus should be further reduced during formation of PS and silica bands. However, it was found that, irrespective of the functionality of PS particles, ordering of PS and silica particles led to formation of similar sized bands.

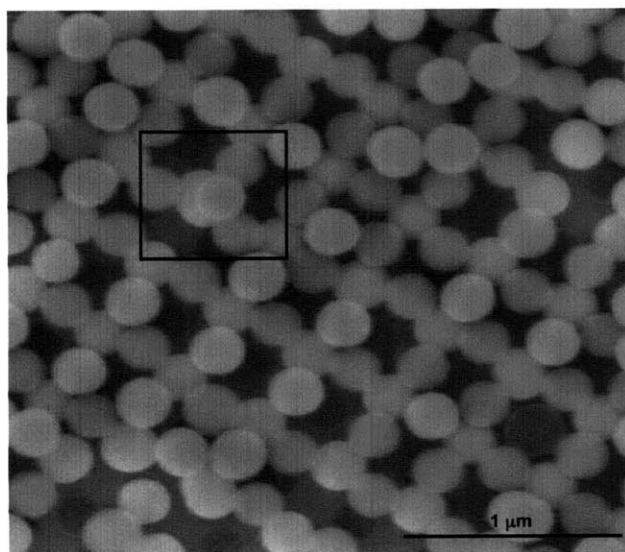


Figure 4-32: SEM image after 250 nm silica particles were deposited in the second layer, from a 0.025-v/v% aqueous suspension at 50°C and 46.1 $\mu\text{m}/\text{min}$, through convective assembly. Prior to silica deposition, the substrate was dipped in 7 mg/ml suspension of PAH for 5 minutes. Note that a negatively charged silica particle is perched on top of another particle in the first layer. This may indicate that charge reversal took place for particles in the first layer, after dipping in the 7 mg/ml suspension of PAH

Table 4.4 shows that L1-PS bands formed from carboxyl and sulphate functionalized particles have similar characteristics.

Table 4.4: Characteristics of L1-PS bands from carboxyl and sulphate functionalized PS particles

Functionalization of PS particles	λ_{band} [μm]	ϕ_{sparse}	δ_{band} [μm]
sulphate	27.6 ± 13.24	0.90 ± 0.10	15.2 ± 7.5
carboxyl	25.1 ± 12.35	0.85 ± 0.07	14.3 ± 6.85

In another experiment, deposition of silica particles was carried out at different relative humidities (RH). It has been shown that stick and slip of the meniscus can be reduced at high RH [143, 175]. Fig. 4-33 is a plot of the characteristics of the bands of silica particles after deposition. As shown here, an increase in RH leads to wider bands; at RH= 80%, no particles are deposited on the template due to high slip on the template. However, silica particles have close-packed order in these bands. As a result, ϕ_{L2} was approximately 0 at all relative humidities. A plot of ϕ_{L2} is shown in fig. 4-34.

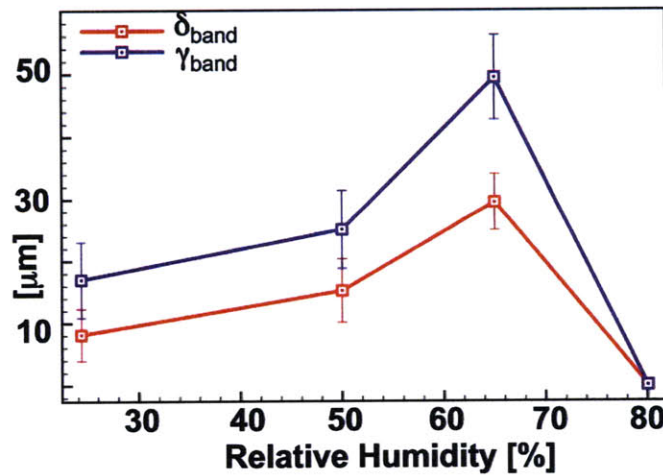


Figure 4-33: Variation of $\lambda_{silica-band}$ and $\delta_{silica-band}$ after deposition of silica particles at different relative humidities.

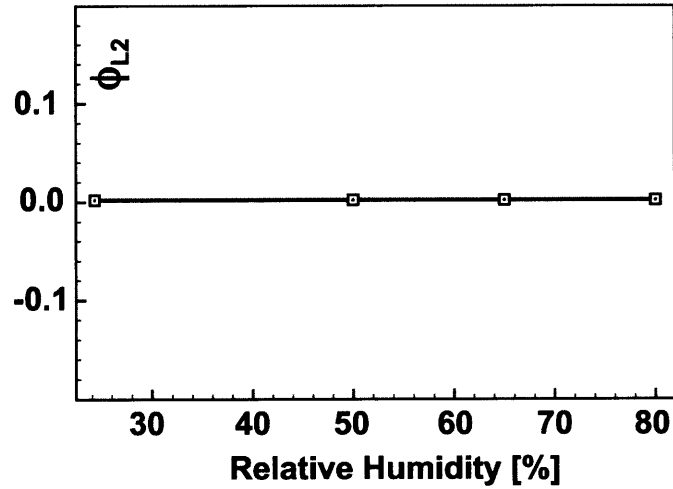


Figure 4-34: Variation of ϕ_{L2} after deposition of silica particles at different relative humidities

4.3.7 L2

From the above discussion, one can infer that optimum domains of L2 were obtained when L2-PS substrates were dipped in 3 mg/ml PAH suspension for 5 minutes. L2 is a two-layer heterostructure formed from PS and silica particles. A low volume fraction silica structure was obtained from this heterostructure by removing the PS particles, without disturbing the silica ones. Latex calcination was not considered for this purpose because it produced liquid latex, which dragged the silica beads by surface tension and caused the structure to collapse. Therefore, a more gentle method was used: oxygen plasma etching at 6 mTorr for 7 minutes. Plasma selectively removes PS and hardly affects the silicon wafer or silica particles.

Fig. 4-35 shows a SEM image of the resulting structure after removal of PS spheres. Fig. 4-36 and fig. 4-37 show a close-up of the top view and the cross-section of the resulting structure. Typically, average values for $\delta_{non--close-packed}$, $\phi_{non--close-packed}$, and $\lambda_{non--close-packed}$ are $24.2\mu m$, 0.11 and $51.2\mu m$ respectively.

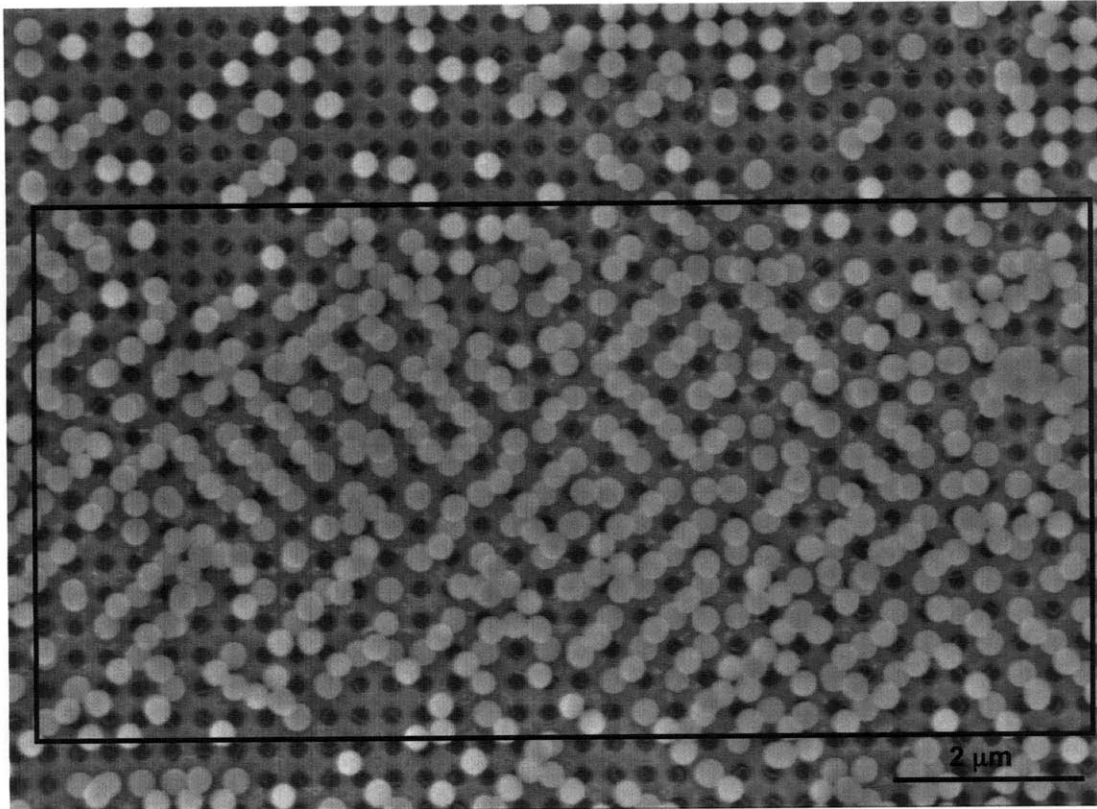


Figure 4-35: SEM image showing a band of 250 nm silica particles arranged in a 3D non-close-packed structure. PS particles were removed from the sample by exposure to oxygen plasma.

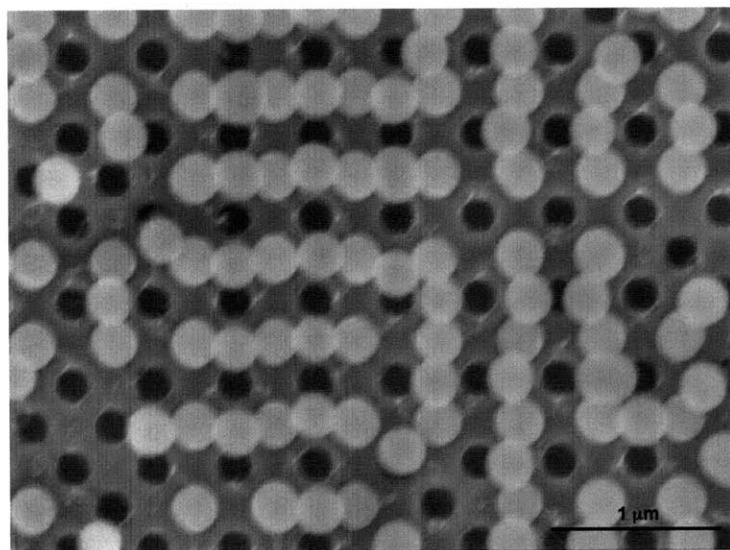


Figure 4-36: SEM image of 250 nm silica particles arranged in a 3D non-close-packed structure. PS particles were removed from the original sample by exposure to oxygen plasma

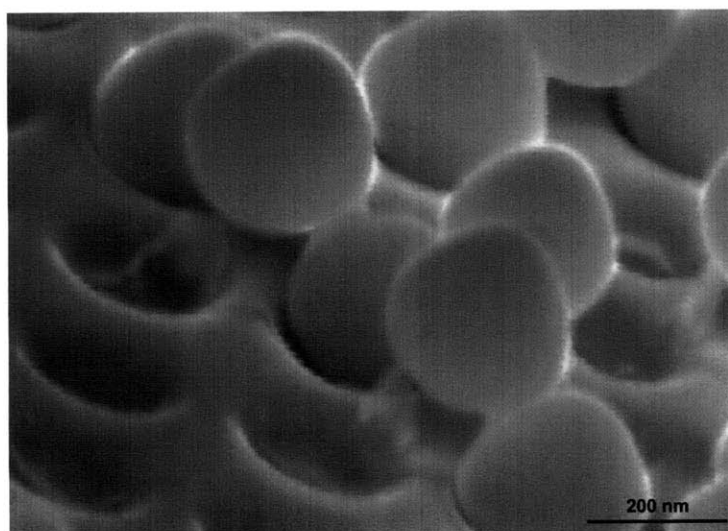


Figure 4-37: SEM image of a cross-section of a template with 250 nm silica particles arranged in a 3D non-close-packed structure

4.4 Concluding Remarks

In summary, it was shown that a sparse pattern of PS particles on a template was obtained by convective assembly. This was obtained at high Debye length in the solvent and low concentration of particles in the suspension. It was further shown that at low Debye length or high concentration of particles, the sparse pattern cannot be stabilized. The sparse pattern was used to make an ordered 2D heterostructure of PS and silica particles. This was fabricated by deposition of identically sized silica particles in the empty sites of the sparse pattern. Compared to traditional methods of obtaining 2D heterostructures, this method is facile, faster, scalable and can potentially produce layers with different symmetries, governed by template geometry. Additionally, a layer-by-layer method of making 3D heterostructures from 2D heterostructures was proposed. Through this method, a two-layer heterostructure of PS and silica was fabricated. Removal of PS particles from the final assembly led to a non-close-packed structure of silica particles. This structure represents the first two layers of a CPBG diamond cubic unit cell. Because self-assembly is used, one is not limited by the particle and solvent type, as long as the process conditions are correctly controlled. Stick and slip of the meniscus was identified as the main impediment in obtaining large domains.

Chapter 5

Stick and Slip During Convective Assembly

In chapter 4, it was shown that convective assembly of colloids leads to the formation of bands with particles separated by regions without any particles. This stripe pattern is formed due to stick and slip of the meniscus on the template. A reduction in stick and slip may lead to larger bands (δ_{band} , eqn. 4.5) and therefore larger domains with sparse structure. Recently, a few methods have been proposed that can prevent stick and slip [145, 176, 177]. Thus, the applicability of these methods to the present set-up is discussed.

The vertical deposition method was developed by Nagayama et al. [122]. They showed that the main factors that contribute to the ordering of particles are the attractive capillary attraction between particles and the convective transport of the suspension to the meniscus. It was further shown that stick and slip of the meniscus during horizontal deposition is a result of the competition between the surface tension of the deposited film, γ_{DF} , surface tension of the suspension, γ_S , and the friction force at the contact line. Leh et al. [173] showed that stick and slip during vertical deposition is due to the interplay between γ_{DF} and the surface tension at the substrate-suspension-air contact line. They suggested that controlling particle concentration, relative humidity and temperature are essential in reducing stick and slip.

Fig. 5-1 shows the different surface tension forces during convective assembly. The equation of motion of the contact line, $L(t)$, for this set-up, is shown in eq. 5.1.

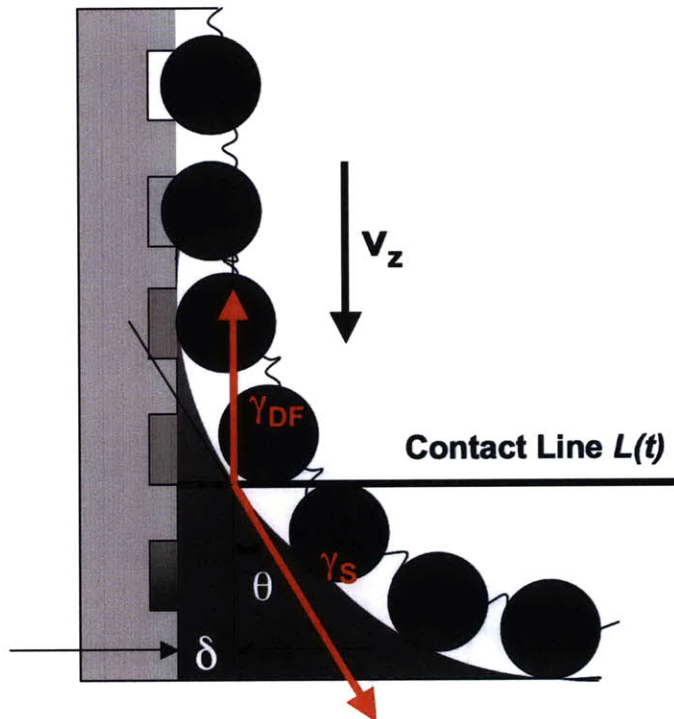


Figure 5-1: Plot of the surface tension forces during convective assembly. The suspension is withdrawn at a rate v_z .

$$\rho \frac{d^2 L}{dt^2} = \gamma_{DF} - \gamma_S \cos(\theta) + \eta \frac{\partial v_z}{\partial x} - \rho g. \quad (5.1)$$

Here, ρ is the density of the suspension, η is the viscosity of the suspension, v_z is the z -component of the velocity of the suspension, and g is the gravitational acceleration. This is similar to the analysis presented by Won et al. [176].

Won et al. [176] recently showed that stick and slip can be avoided when colloidal films are assembled through Langmuir-Blodgett (LB) technique at high humidity and high concentration of particles. They found that the final particle density on the template is significantly lower than the initial particle density at the air-water

interface. In their experiments, transfer efficiencies were $0.19 \pm 0.04^*$ when a template with holes arranged in (100) symmetry was used. They also showed that the transfer efficiency decreases with an increase in the lifting speed of the substrate. In their model, they assumed that at high humidity, water does not evaporate during self-assembly. With this assumption, their analysis showed that ϕ , the particle area fraction in the monolayer on a template, is given by eq. 5.2:

$$\phi = \phi_0 + \frac{D^2}{c \cdot \cos(\theta)} \left(\frac{\partial \gamma}{\partial \phi} \right)_{\phi=\phi_0} \left(\frac{6\eta U}{D\delta} + \rho g \right). \quad (5.2)$$

Here, ϕ_0 is the particle area fraction in the monolayer on the solvent (i.e. far away from the contact line), D is the particle diameter, c is an adjustable parameter, U is the velocity at which the template is withdrawn during LB assembly, and δ is the wetting film thickness. In the sparse pattern, fig. 4-6, ϕ is 0.22. The corresponding ϕ_0 , according to eq. 5.2, is 0.24 for particles with $D = 250nm$. This corresponds to a concentration of 5×10^{12} *particles/m*². For this calculation, it was assumed that $\delta = D$, $U = 1mm/min$, $c \cdot \cos\theta = 15.15 \times 10^{-15}$, and $\partial\gamma/\partial\phi = -3.2 \times 10^{-4}mN \cdot m$. In comparison, if an isotropic distribution of particles is assumed during convective assembly, the concentration at the air-solvent interface is 9.77×10^{10} *particles/m*²†—assuming a volume concentration of 0.025-v/v%. This indicates that a lower ϕ_0 may be required during LB assembly.

According to eq. 5.2, a lower ϕ_0 can be used if the second term on right side of eq. 5.2 is decreased. This indicates that during LB assembly of particles, it is ideal to have transfer efficiency as close to 1.0 as possible. As shown by Won et al. this is possible if the colloidal film is assembled at a lower U . At very low U , it may be possible to ignore the entire second term on the right side in eq. 5.2 and obtain transfer efficiency close to 1.0. Clearly, in this regime, the final arrangement of particles on the template will also be influenced by the interaction between particles. Additionally, a high humidity may be required to avoid stick and slip during deposition.

*Transfer efficiency is defined as the ratio of the density of particles assembled on a template to the density of particles on the air-solvent interface.

†This corresponds to a $\phi_0 = 0.0048$

Besides LB method, spin coating [177] and hydrodynamic flow of particles [145] can lead to domains without stick and slip. However, both these methods are kinetically driven, where the particles are forced to arrange in or between surface features due to rapid solvent evaporation or flow. Additionally, a high concentration of particles is required. Therefore, these may not lead to the formation of the sparse pattern.

Chapter 6

Monte Carlo Simulations of Sparse Ordering

A number of methods exist to predict the nucleation of stable colloidal phases [2, 100]. Researchers have often relied on free energy calculations to predict the most stable colloidal structures. They have shown that when the potential in a colloidal system is repulsive, packing arguments and entropy alone are sufficient to cause bulk crystallization of stable phases [123].

Contrary to this argument, in chapter 4 it was shown that sparse structures do not nucleate at high κR , irrespective of the concentration of particles. To investigate this further, detailed Monte Carlo simulations are discussed in this chapter. These show that the final order in fig. 4-6 results from an interplay of the concentration and electrostatic repulsion between particles.

In Monte Carlo methods, random system changes are rejected or accepted according to predefined rules. The scheme followed here is the Metropolis algorithm [179]. In this scheme, a change is always accepted if it results in lower system energy. However, it is only accepted with a Boltzmann probability, if it leads to an increase in the total system energy. These rules satisfy the conditions of detailed balance, which states that the number of transitions from state A to state B must equal the number of transitions from state B to state A. More detailed information about Monte Carlo schemes can be obtained elsewhere [180].

The internal energy in a colloidal system is obtained by a pairwise summation of the interaction energy. In a canonical ensemble (NVT system), the movement of a particle leads to a change in the internal energy ΔU_i . The acceptance rules for a transition in such a system from A_i to B_i are:

$$\Delta U_i < 0 \quad acc(A_i \rightarrow B_i) = 1 \quad (6.1)$$

$$\Delta U_i > 0 \quad acc(A_i \rightarrow B_i) = \exp\left(-\frac{\sum_{j \neq i} \Delta U_{ij}}{k_B T}\right). \quad (6.2)$$

In a grand canonical ensemble (μVT), in addition to the movement of particles, the internal energy can change due to creation or destruction of a particle. As a result, there are additional acceptance rules. These are:

For particle creation:

$$\Delta U_i - \mu T < 0 \quad acc(A_i \rightarrow B_i) = 1 \quad (6.3)$$

$$\Delta U_i - \mu T > 0 \quad acc(A_i \rightarrow B_i) = \exp\left(-\frac{\sum_{j \neq i} \Delta U_{ij} - \mu T}{k_B T}\right), \quad (6.4)$$

and for particle destruction:

$$\Delta U_i + \mu T < 0 \quad acc(A_i \rightarrow B_i) = 1 \quad (6.5)$$

$$\Delta U_i + \mu T > 0 \quad acc(A_i \rightarrow B_i) = \exp\left(-\frac{\sum_{j \neq i} \Delta U_{ij} + \mu T}{k_B T}\right), \quad (6.6)$$

where μ is the chemical potential.

6.1 Simulation Set-up

Simulations were conducted to verify the formation of a sparse pattern of polystyrene (PS) particles, discussed in section 4.3. The templated assembly set-up described

in chapter 4 is best simulated by a grand canonical ensemble. Indeed, the template represents a system where particles may enter or leave at will; this is dictated by the chemical potential and the volume of the suspension. Thus, a grand canonical ensemble was chosen for the Monte Carlo (MC) simulations. The simulation box is a template with holes arranged in a square pattern, akin to fig. ???. For the current set-up, the simulation template had 24×24 sites. All templates were tested with periodic boundary conditions. Since $\lambda_2 > 1$, the final arrangement of colloidal particles is non close packed, even when all the holes are occupied. Thus, vdW interactions can be ignored. As a result, internal energy is given by a pairwise summation of the electrostatic energy only. The picture that emerges is that of an Ising model type system, with each site either with or without a particle.

MC simulations were carried out to obtain optimal arrangement of 140 nm, 250 nm and 500 nm sized PS particles. Corresponding pitches for the templates were 185 nm, 330 nm and 660 nm, respectively. A colloidal dispersion is characterized by κ^{-1} in the solvent, the concentration of particles in the suspension and temperature, T . Thus, for each particle type, MC runs were carried out when $\kappa^{-1} = 30$ nm, 100 nm and 204 nm.

The phase boundary between sparsely ordered phase and the phase where all sites on the template were occupied, was tracked by the change in a translational order parameter, τ . τ [181, 182, 183], was computed over $T - \mu$ phase space, at constant κ^{-1} . The translational order parameter, τ , is given by eq. 6.7 [183]:

$$\tau = \frac{1}{s_c} \int_0^{s_c} |g(s) - 1| ds, \quad (6.7)$$

where $g(s)$ is the pair distribution function, and $s = r\rho^{1/3}$, is the radial distance scaled by the number density, and s_c is a numerical cutoff. In this work $s_c=6.0$.

For each MC set-up, initial arrangement of particles was chosen by randomly deciding if a site is occupied (that is, if it has a particle), or vacant. A thousand MC steps were run before recording any data. Fluctuations in the system energy were negligible after 1,000 steps. A further 2,000 steps were run to gather data after

initialization. During each of these steps, system energy and arrangement of the particles were recorded.

6.2 Simulation Results

The energy of a configuration depends on the electrostatic interaction between particles and the chemical potential energy of the system. Electrostatic energy is calculated as a pairwise summation of the Yukawa interaction between particles. On the other hand, the chemical potential energy is proportional to the concentration of particles and the temperature of the system. It is given as a product between the chemical potential for the system and the average number of particles on the template. Mathematically, the system energy is written as:

$$U_{system} = U_{Yukawa} + \mu \times N_{avg}, \quad (6.8)$$

where

$$\mu = k_B \times T \times \ln(c). \quad (6.9)$$

Although τ was tracked over $\mu - T$ space, it is more instructive to look at changes in τ in the concentration- T landscape. The system energy varied smoothly over $\mu - T$ and concentration- T phase spaces. As a result, nucleation of a new phase was undetectable from energy plots. On the other hand, τ showed discontinuous variation over $\mu - T$. Since μ is proportional to concentration, c , these discontinuities were observed on the $c - T$ landscape too. This indicates that there might be one or more phase transitions in the system.

For all particle sizes, when κ^{-1} was 30 nm, electrostatic interaction between particles was weak. Thus, system energy was dominated by the chemical potential energy. As a result, configurations where all sites on the template were filled, were stabilized over all others. For 140 nm particles, this is seen in the contour plot of τ (fig. 6-1). Here, $\tau = 1.1$, when all sites on the template are occupied. This configuration is labeled and is stable over most of the plot. When κ^{-1} is 100 nm, the configuration

when all sites on the template are occupied, is stable over a smaller region in the $c-T$ landscape (fig. 6-2). Finally, when κ^{-1} is 204 nm, the configuration when all sites on the template are occupied, is stable over a very small region in the $c-T$ landscape (fig. 6-3). Similar plots are shown for 250 nm and 500 nm particles in fig. 6-4-fig. 6-6 and fig. 6-7-fig. 6-9 respectively.

When κ^{-1} is 204 nm, there are numerous features on the $c-T$ landscape; many phases may be stable. For a better understanding, a brief discussion for the arrangement of particles at different T , $\kappa^{-1}=204$ nm, and $\ln(c)=40.1$ is presented.

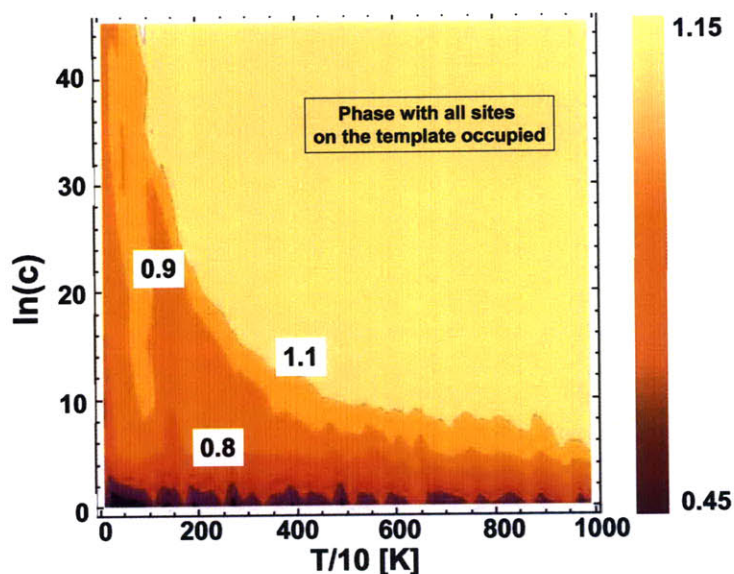


Figure 6-1: Plot of τ across $\ln(c) - T$ landscape, for the arrangement of 140 nm particles, when $\kappa^{-1}=30$ nm

6.3 Discussion

The variation in the arrangement of 140 nm, 250 nm and 500 nm particles at $\kappa^{-1} = 204$ nm and $\ln(c) = 40.1$ is presented in fig. 6-10 - 6-13, fig. 6-14 - 6-17 and fig. 6-18 - 6-21 respectively. In these figures, solid red circles represent an occupied site, whereas an empty circle represents an empty site. A pair distribution function (PDF) for each arrangement is plotted next to its respective figure.

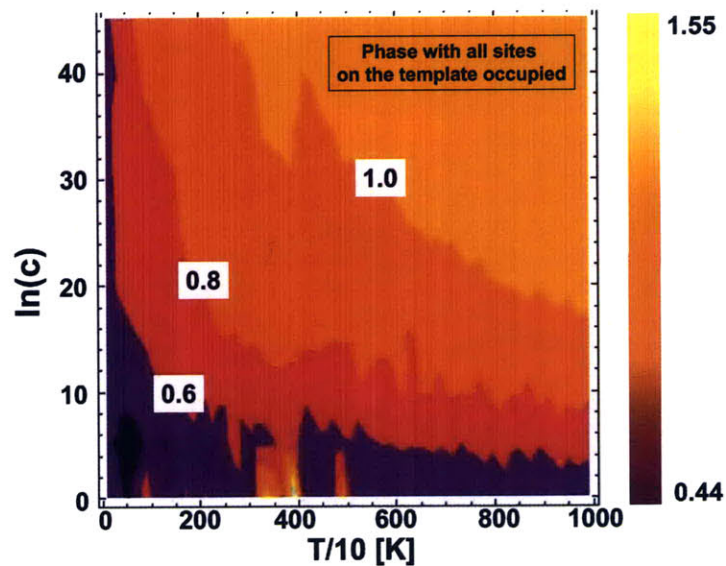


Figure 6-2: Plot of τ across $\ln(c) - T$ landscape, for the arrangement of 140 nm particles, when $\kappa^{-1}=100$ nm

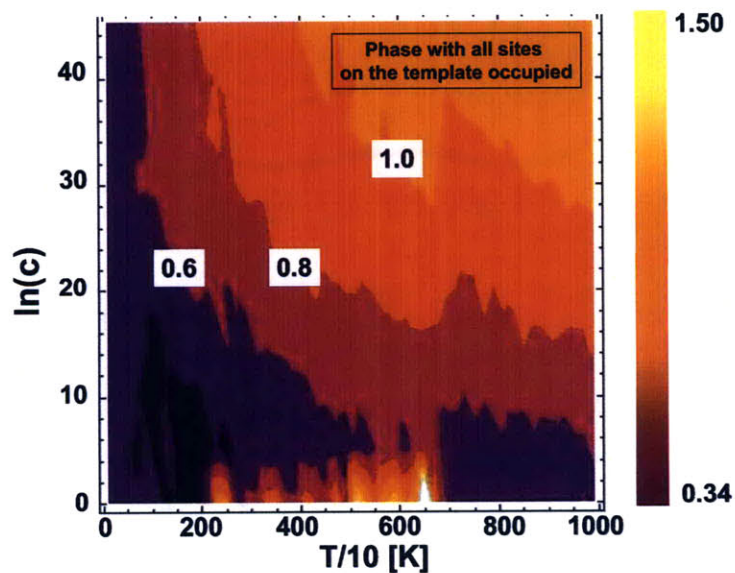


Figure 6-3: Plot of τ across $\ln(c) - T$ landscape, for the arrangement of 140 nm particles, when $\kappa^{-1}=204$ nm

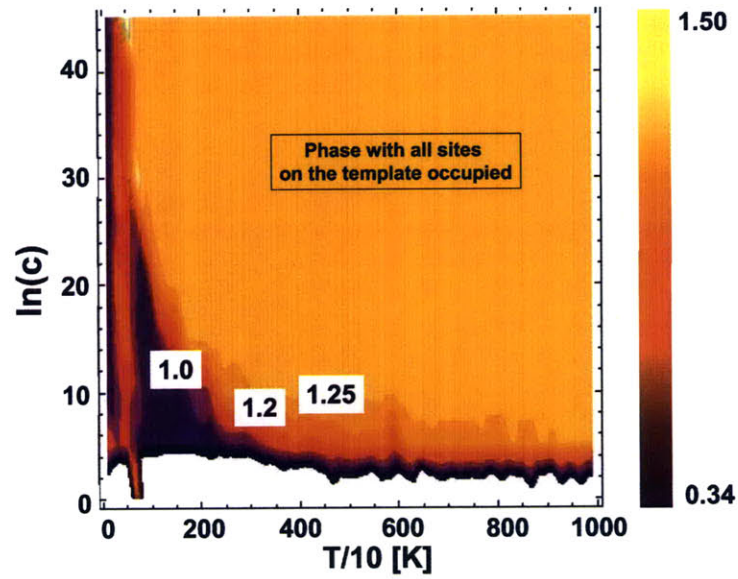


Figure 6-4: Plot of τ across $\ln(c) - T$ landscape, for the arrangement of 250 nm particles, when $\kappa^{-1}=30$ nm

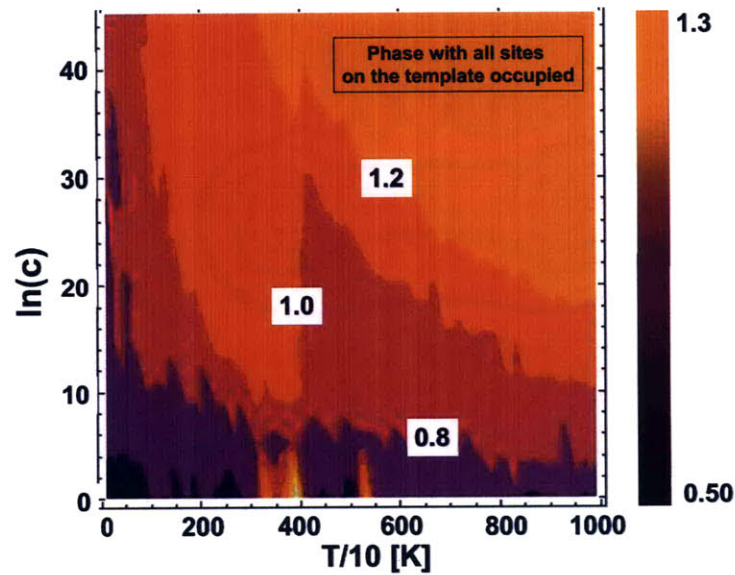


Figure 6-5: Plot of τ across $\ln(c) - T$ landscape, for the arrangement of 250 nm particles, when $\kappa^{-1}=100$ nm

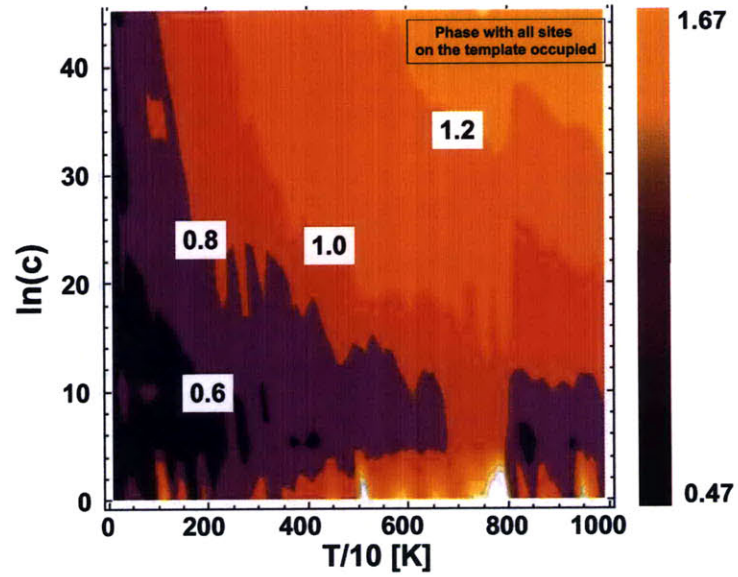


Figure 6-6: Plot of τ across $\ln(c) - T$ landscape, for the arrangement of 250 nm particles, when $\kappa^{-1}=204$ nm

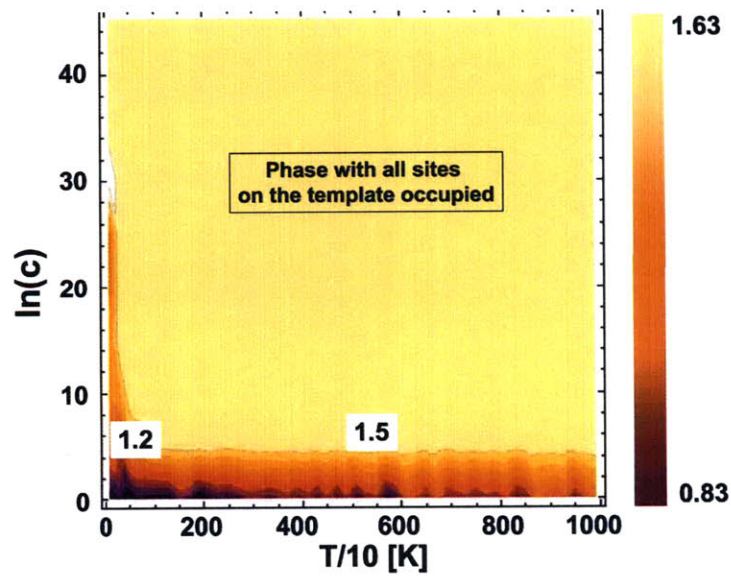


Figure 6-7: Plot of τ across $\ln(c) - T$ landscape, for the arrangement of 500 nm particles, when $\kappa^{-1}=30$ nm

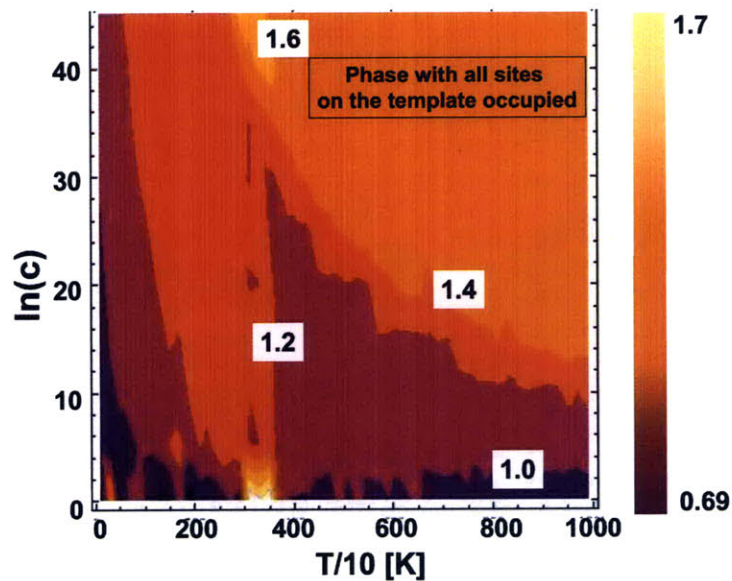


Figure 6-8: Plot of τ across $\ln(c) - T$ landscape, for the arrangement of 500 nm particles, when $\kappa^{-1}=100$ nm

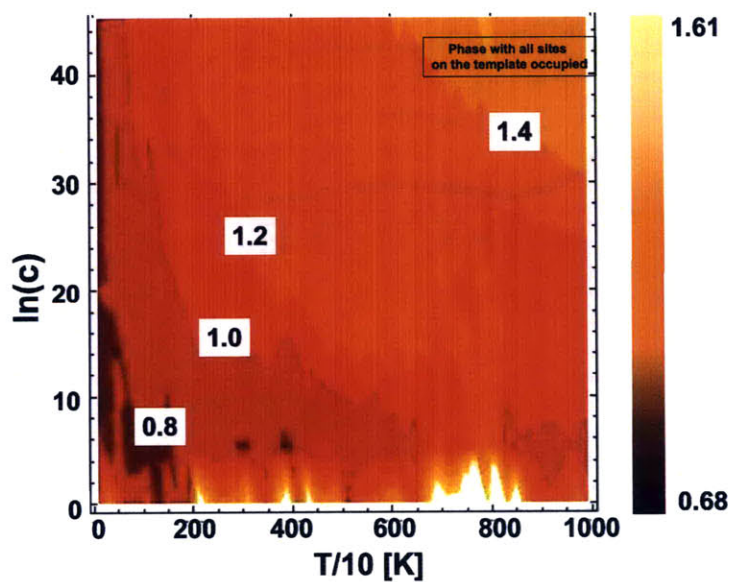


Figure 6-9: Plot of τ across $\ln(c) - T$ landscape, for the arrangement of 500 nm particles, when $\kappa^{-1}=204$ nm

At $T=1100\text{K}$, nuclei of a sparser structure (similar to fig. 4-20) are visible in the arrangement of 140 nm (fig. 6-10) and 250 nm (fig. 6-14) particles. In comparison, 500 nm particles arrange randomly. Their arrangement at $T=1100\text{ K}$ is shown in fig. 6-18. At $T=3100\text{K}$, nuclei of sparse structure are stabilized for all particle sizes. Fig. 6-11, fig. 6-15 and fig. 6-19 show the arrangement of 140 nm, 250 nm and 500 nm particles at 3100 K, respectively. Sparse domains of 140 nm (fig. 6-12) and 250 nm (fig. 6-16) particles remain stable up till $T=5100\text{K}$; sparse domains of 500 nm particles start to shrink at $T=5100\text{ K}$ (fig. 6-20). Finally, when $T=7100\text{K}$, the sparse structure disappears completely and is replaced by a structure in which all sites are occupied. Fig. 6-13, fig. 6-17 and fig. 6-21 show the arrangement of 140 nm, 250 nm and 500 nm particles at 7100 K, respectively.

For all particle sizes, the sparse structure is stable up to $T \approx 3100\text{K}$, when $\kappa^{-1}=100$ nm, and not stable at all when $\kappa^{-1}=30$ nm. These simulations show that decreasing κ^{-1} reduces the size of domains with sparse arrangement of particles. This agrees with the experimental observations discussed in chapter 4. As a result, it can be inferred that although entropy maximization may have a role to play in stabilizing the sparse structure, the key role is played by the high Debye length in the system and a low concentration of particles.

Fig. 6-10 and fig. 6-14 show that small domains with sparser structure can also be nucleated if the concentration of particles is low. However, as seen in fig. 4-20, stabilization of large domains with this structure, requires an even higher κ^{-1} .

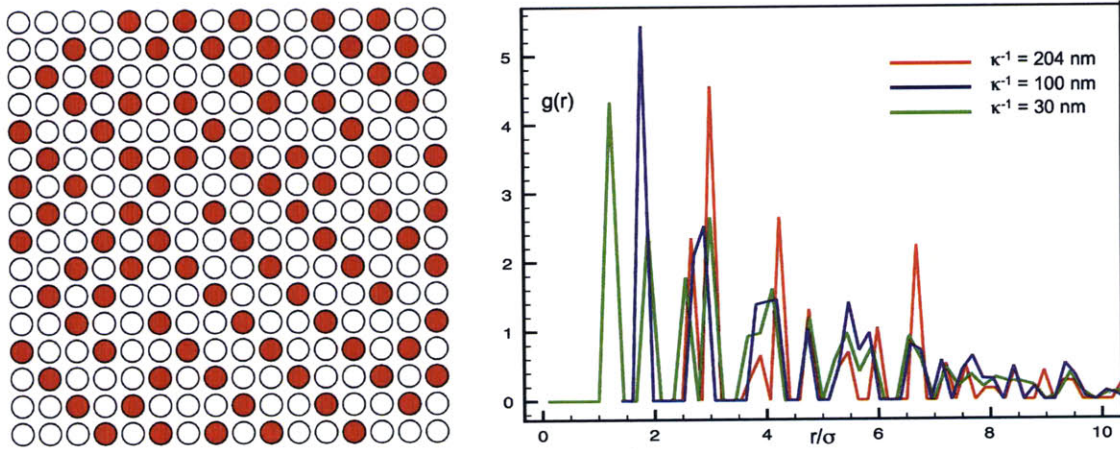


Figure 6-10: (a)Arrangement of 140 nm particles at $\kappa^{-1}=204$ nm, $\ln(c)=40.1$ and $T=1100$ K. (b)Pair Distribution Function (PDF) for the particles on the template, in (a), is plotted in red. For comparison, PDF for the arrangement of particles at $\kappa^{-1}=100$ nm and 30 nm are plotted in blue and green respectively. These PDF plots show that unlike at $\kappa^{-1}=204$ nm, at $\kappa^{-1}=30$ nm, all sites on the template are occupied.

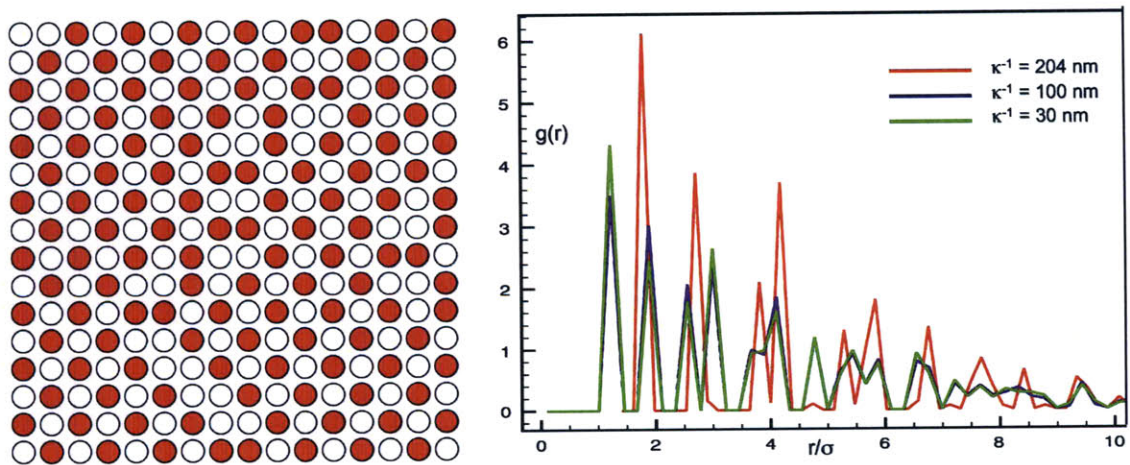


Figure 6-11: (a)Arrangement of 140 nm particles at $\kappa^{-1}=204$ nm, $\ln(c)=40.1$ and $T=3100$ K. (b)Pair Distribution Function (PDF) for the particles on the template, in (a), is plotted in red. For comparison, PDF for the arrangement of particles at $\kappa^{-1}=100$ nm and 30 nm are plotted in blue and green respectively. These PDF plots show that unlike at $\kappa^{-1}=204$ nm, at $\kappa^{-1}=30$ nm, all sites on the template are occupied.

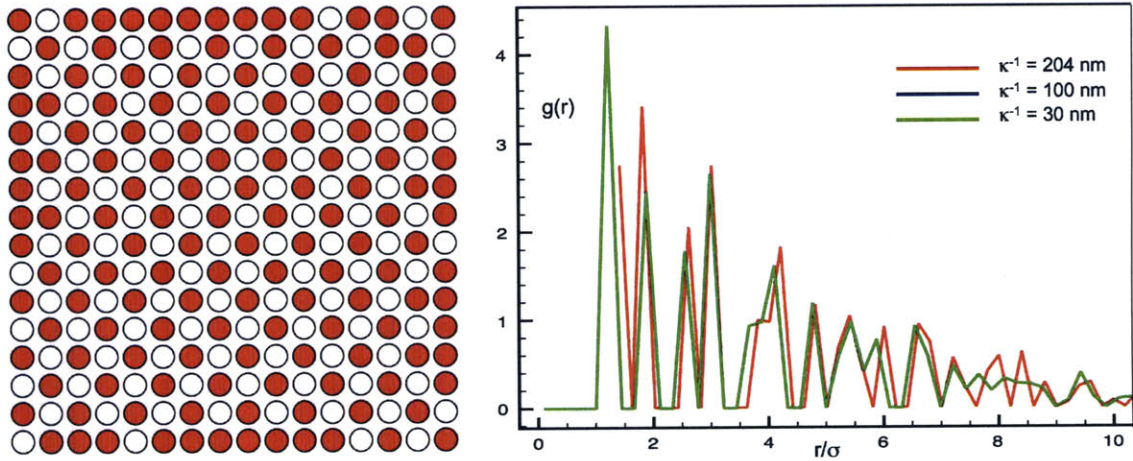


Figure 6-12: (a) Arrangement of 140 nm particles at $\kappa^{-1}=204$ nm, $\ln(c)=40.1$ and $T=5100$ K. (b) Pair Distribution Function (PDF) for the particles on the template, in (a), is plotted in red. For comparison, PDF for the arrangement of particles at $\kappa^{-1}=100$ nm and 30 nm are plotted in blue and green respectively. These PDF plots show that at $\kappa^{-1}=30$ nm all sites on the template are occupied; many domains where all sites are occupied, are also stabilized for $\kappa^{-1}=204$ nm.

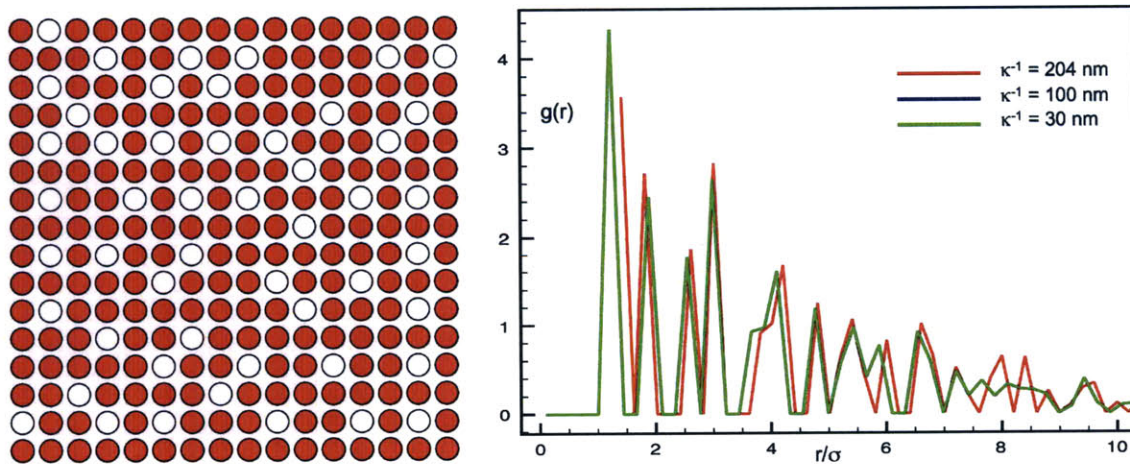


Figure 6-13: (a) Arrangement of 140 nm particles at $\kappa^{-1}=204$ nm, $\ln(c)=40.1$ and $T=7100$ K. (b) Pair Distribution Function (PDF) for the particles on the template, in (a), is plotted in red. For comparison, PDF for the arrangement of particles at $\kappa^{-1}=100$ nm and 30 nm are plotted in blue and green respectively. These PDF plots show that at all κ^{-1} values, all sites on the template are occupied.

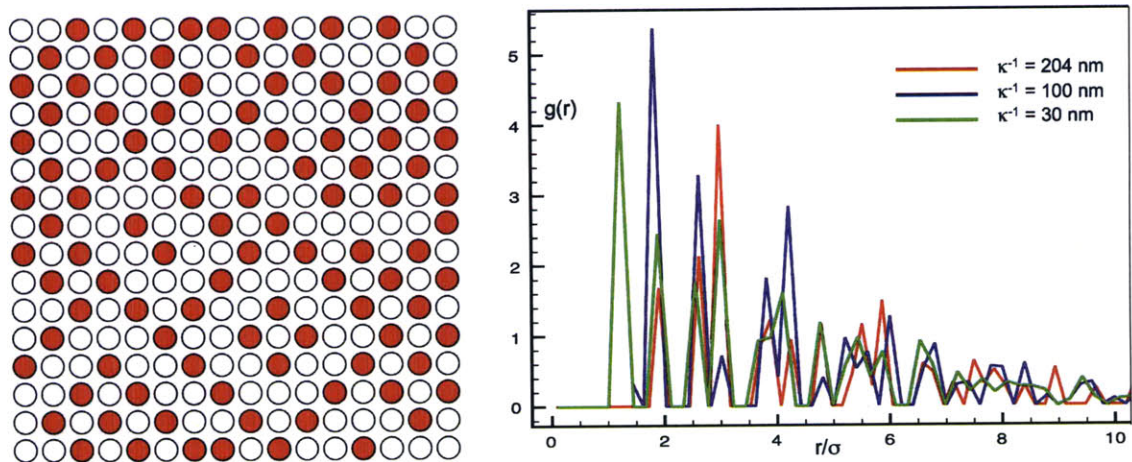


Figure 6-14: (a)Arrangement of 250 nm particles at $\kappa^{-1}=204$ nm, $\ln(c)=40.1$ and $T=1100$ K. (b)Pair Distribution Function (PDF) for the particles on the template, in (a), is plotted in red. For comparison, PDF for the arrangement of particles at $\kappa^{-1}=100$ nm and 30 nm are plotted in blue and green respectively. These PDF plots show that unlike at $\kappa^{-1}=204$ nm, at $\kappa^{-1}=30$ nm, all sites on the template are occupied.

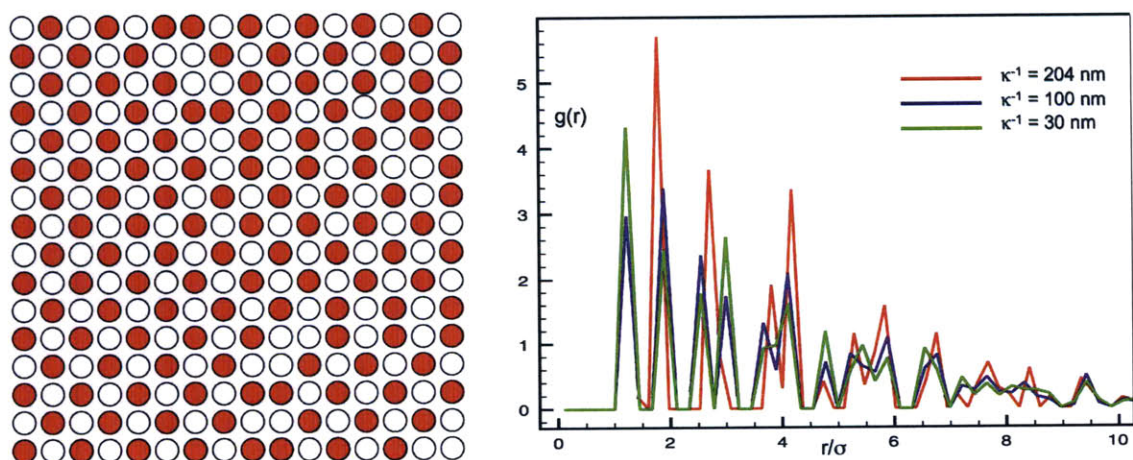


Figure 6-15: (a)Arrangement of 250 nm particles at $\kappa^{-1}=204$ nm, $\ln(c)=40.1$ and $T=3100$ K. (b)Pair Distribution Function (PDF) for the particles on the template, in (a), is plotted in red. For comparison, PDF for the arrangement of particles at $\kappa^{-1}=100$ nm and 30 nm are plotted in blue and green respectively. These PDF plots show that unlike at $\kappa^{-1}=204$ nm, at $\kappa^{-1}=30$ nm, all sites on the template are occupied.

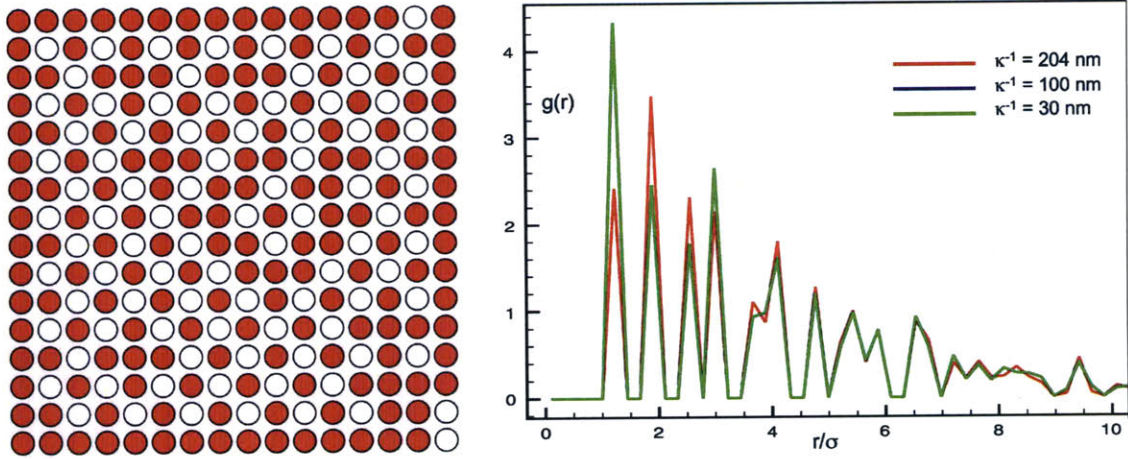


Figure 6-16: (a) Arrangement of 250 nm particles at $\kappa^{-1}=204$ nm, $\ln(c)=40.1$ and $T=5100$ K. (b) Pair Distribution Function (PDF) for the particles on the template, in (a), is plotted in red. For comparison, PDF for the arrangement of particles at $\kappa^{-1}=100$ nm and 30 nm are plotted in blue and green respectively. These PDF plots show that at $\kappa^{-1}=30$ nm all sites on the template are occupied; many domains where all sites are occupied, are also stabilized for $\kappa^{-1}=204$ nm.

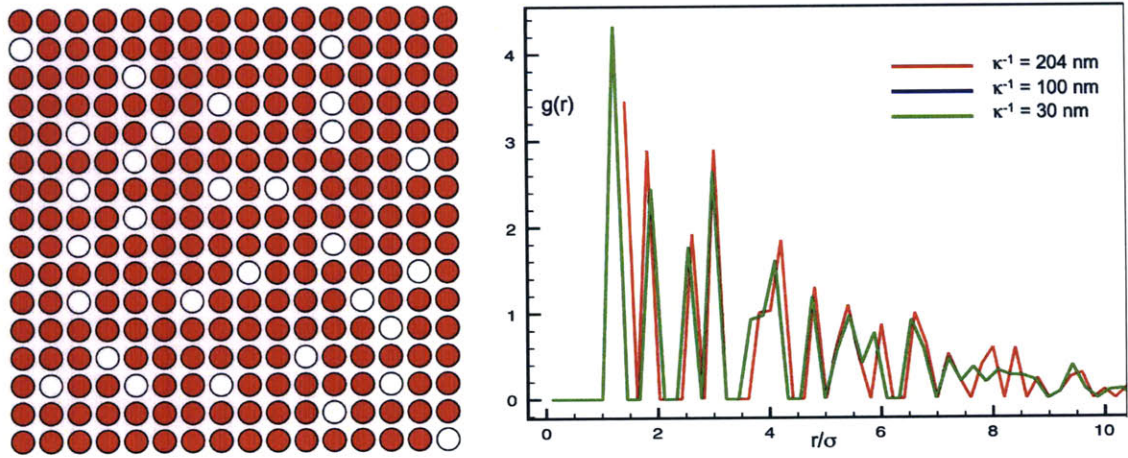


Figure 6-17: (a) Arrangement of 250 nm particles at $\kappa^{-1}=204$ nm, $\ln(c)=40.1$ and $T=7100$ K. (b) Pair Distribution Function (PDF) for the particles on the template, in (a), is plotted in red. For comparison, PDF for the arrangement of particles at $\kappa^{-1}=100$ nm and 30 nm are plotted in blue and green respectively. These PDF plots show that at all κ^{-1} values, all sites on the template are occupied.

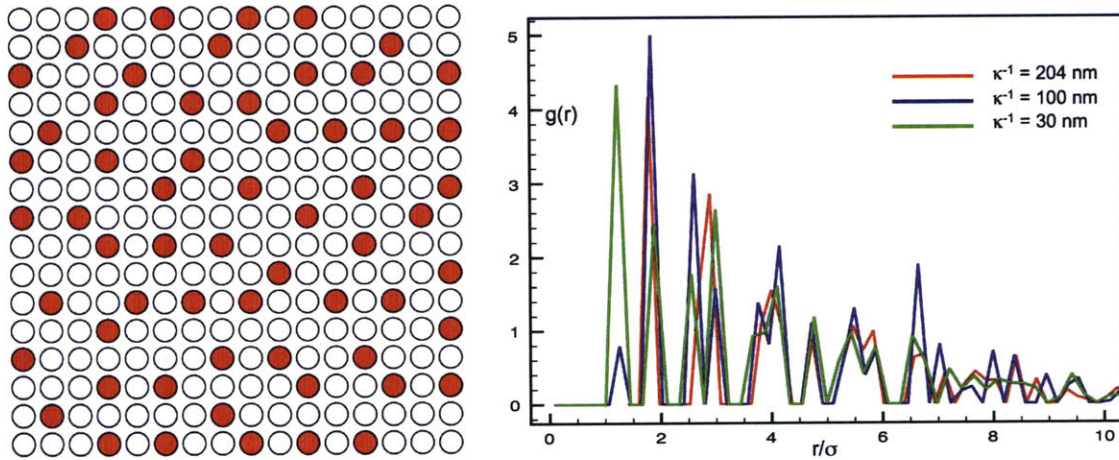


Figure 6-18: (a)Arrangement of 500 nm particles at $\kappa^{-1}=204$ nm, $\ln(c)=40.1$ and $T=1100$ K. (b)Pair Distribution Function (PDF) for the particles on the template, in (a), is plotted in red. For comparison, PDF for the arrangement of particles at $\kappa^{-1}=100$ nm and 30 nm are plotted in blue and green respectively. These PDF plots show that unlike at $\kappa^{-1}=204$ nm, at $\kappa^{-1}=30$ nm, all sites on the template are occupied.

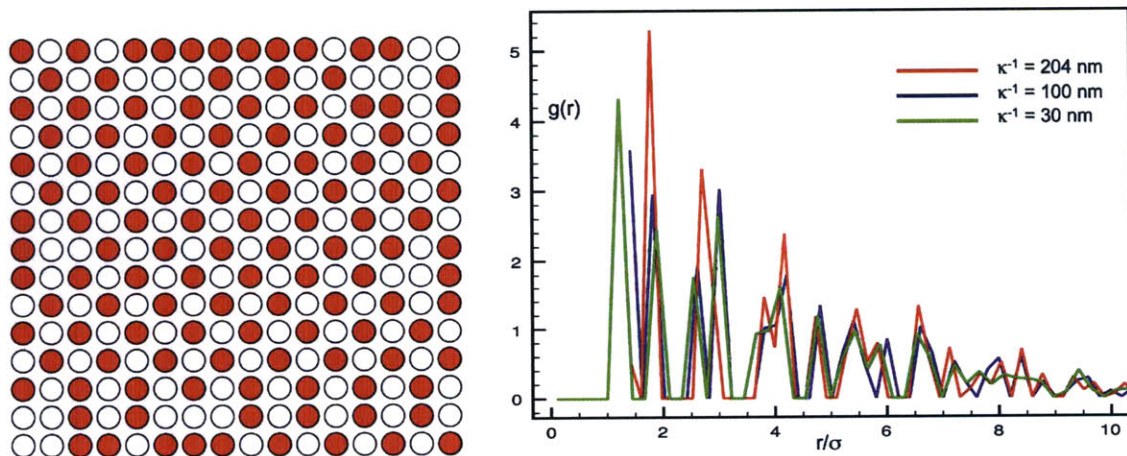


Figure 6-19: (a)Arrangement of 500 nm particles at $\kappa^{-1}=204$ nm, $\ln(c)=40.1$ and $T=3100$ K. (b)Pair Distribution Function (PDF) for the particles on the template, in (a), is plotted in red. For comparison, PDF for the arrangement of particles at $\kappa^{-1}=100$ nm and 30 nm are plotted in blue and green respectively. These PDF plots show that unlike at $\kappa^{-1}=204$ nm, at $\kappa^{-1}=30$ nm, all sites on the template are occupied.

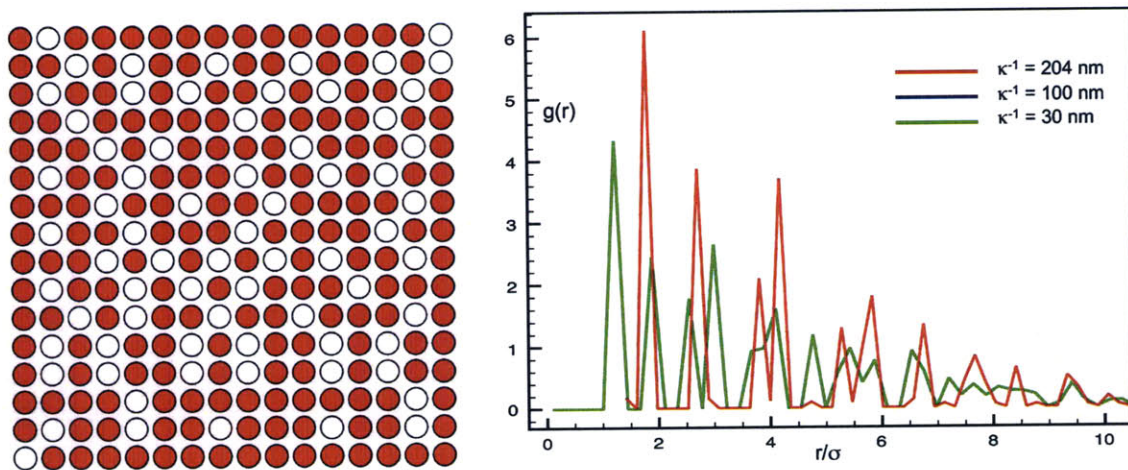


Figure 6-20: (a)Arrangement of 500 nm particles at $\kappa^{-1}=204$ nm, $\ln(c)=40.1$ and $T=5100$ K. (b)Pair Distribution Function (PDF) for the particles on the template, in (a), is plotted in red. For comparison, PDF for the arrangement of particles at $\kappa^{-1}=100$ nm and 30 nm are plotted in blue and green respectively. These PDF plots show that at $\kappa^{-1}=30$ nm all sites on the template are occupied; many domains where all sites are occupied, are also stabilized for $\kappa^{-1}=204$ nm.

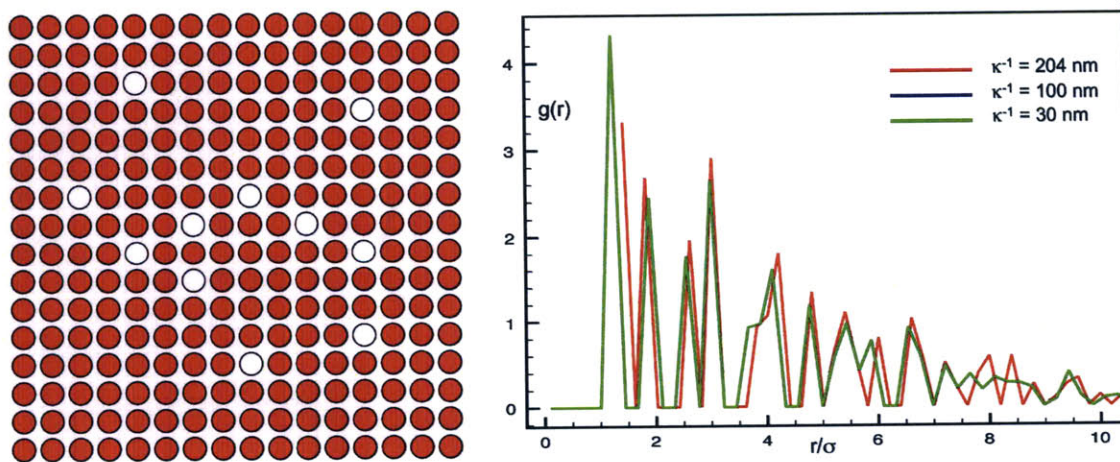


Figure 6-21: (a)Arrangement of 500 nm particles at $\kappa^{-1}=204$ nm, $\ln(c)=40.1$ and $T=7100$ K. (b)Pair Distribution Function (PDF) for the particles on the template, in (a), is plotted in red. For comparison, PDF for the arrangement of particles at $\kappa^{-1}=100$ nm and 30 nm are plotted in blue and green respectively. These PDF plots show that at all κ^{-1} values, all sites on the template are occupied.

6.4 Conclusion

In summary, it was correlated with simulation that nucleation of stable sparse structures, akin to fig. 4-6 and fig. 4-20, takes place at high κ^{-1} and low concentration of particles. It was shown that electrostatic repulsion is the key to obtaining large domains with sparse order. Moreover, sparser domains can be nucleated and stabilized over large distances if κ^{-1} is higher, and concentration of particles in the system, lower. Although higher κ^{-1} may not be achievable in aqueous suspensions, it can be obtained in mildly polar solvents, like isopropanol or ethyl alcohol. Thus, in these solvents it may be possible to nucleate and stabilize other sparser structures over larger distances.

Chapter 7

Conclusions and Outlook

Among the many approaches to create non-close-packed structures, self-assembly is appealing because it can create a colloidal crystal quickly and over a desired length scale. In this thesis, lower symmetry structures were created by exploiting interparticle interactions between strongly charged particles.

It was shown that oppositely charged hydrophobic particles can be rapidly arranged into ordered 2D architectures through spin-coating. Calculations showed that non-ionic amphiphilic surfactants create a steric barrier, that prevents these particles from coagulating during self-assembly. Previously, only oppositely charged particles with charge densities two orders of magnitude lower had been ordered. It was shown that, at high Debye length and low particle concentration, a layer-by-layer method can be used to create a non-close-packed arrangement of like-charged particles, on a substrate of close-packed and oppositely charged particles.

Electrostatic repulsion between similarly charged colloidal particles was exploited to nucleate and stabilize non-close-packed structures with sparse ordering on lithographically fabricated templates. It was shown that a 2D heterostructure can be created by filling the remaining holes on the template with another particle type. Two layers of a 2D heterostructure were created through layer-by-layer assembly. In the end, one kind of particle was removed to create a two-layer non-close-packed structure of silica particles. Stick and slip of the meniscus limited the overlap between bands of particles during each deposition step. As a result, non-close-packed domains

were only a few micrometers large. Monte Carlo simulations confirmed that sparse structures are nucleated only at high Debye lengths and low particle concentrations. In addition, it was found that sparser domains can be nucleated at an even higher Debye length and lower concentration of particles.

Implications from the above studies are many. Newer structures, which are more robust compared to their like-charged counterparts, can now be fabricated from oppositely charged particles. These include binary structures or non-close-packed structures, like zinc blende. On the other hand, templates with different geometries may be used to create multiple sparse structures.

The biggest challenge lies in arresting the effect of stick and slip. It was shown that bands with sparse order were around $15\ \mu\text{m}$ wide, although these were hundreds of micrometers long perpendicular to the direction of meniscus slip. If stick and slip can be arrested, it may lead to very wide bands. This may encourage the discovery of newer self-assembly processes. Already, horizontal assembly reduces stick and slip, but it provides no control over the thickness of colloidal crystals that are fabricated. It may be that a combination of vertical and horizontal deposition is required to overcome stick and slip.

Interest in the fabrication of crystals of colloidal particles with controlled packing, symmetry, periodicity, crystal orientation and packing quality, is fueled by the need for colloidal crystals exhibiting tailored structures in many applications. Methods and results described herein constitute a step in this direction, allowing for the use of self-assembly to fabricate novel non-close-packed structures.

Bibliography

- [1] A. Vrij, E. A. Nieuwenhuis, H. M. Fijnaut, and W. G. Agterof. Application of modern concepts in liquid state theory to concentrated particle dispersions. *Faraday Discussions of the Chemical Society*, 65:101–113, 1978.
- [2] Jacob Hoogenboom. *Colloidal Epitaxy: A Real-Space Analysis*. PhD thesis, Universiteit Utrecht, 2002.
- [3] P. N. Pusey, editor. *Liquids, freezing and the glass transition*. Elsevier, Amsterdam, 1990.
- [4] A. van Blaaderen. Quantitative real-space analysis of colloidal structures and dynamics with confocal scanning light microscopy. *Progress in Colloid and Polymer Science*, 104:59–65, 1997.
- [5] A. Vrij, J. W. Jansen, J. K. G. Dhont, C. Pathmamanoharan, M. M. Kops-Werkhoven, and H. M. Fijnaut. Light scattering of colloidal dispersion in non-polar solvents at finite concentrations. silica spheres as model particles for hard-sphere interactions. *Faraday Discussions*, 76:19–36, 1983.
- [6] R. W. J. Scott. Electronically addressable SnO_2 inverted opal gas sensors fabricated on interdigitated gold microelectrodes. *Chemical Communications*, 6:688–689, 2003.
- [7] A. C. Sharma. A general photonic crystal sensing motif: Creatinine in bodily fluids. *Journal of American Chemical Society*, 126(9):2971–2977, 2004.
- [8] S. A. Asher. Photonic crystal aqueous metal cation sensing materials. *Analytical Chemistry*, 75(7):1676–1683, 2003.
- [9] Michael R. Newton, Andrew K. Bohaty, Henry S. White, and Ilya Zharov. Chemically modified opals as thin permselective nanoporous membranes. *Journal of American Chemical Society*, 127:7268–7269, 2005.
- [10] Andrew K. Bohaty and Ilya Zharov. Suspended self-assembled opal membranes. *Langmuir*, 22:5533–5536, 2006.
- [11] K. M. Ho, C. T. Chan, and C. M. Soukoulis. Existence of a photonic gap in periodic dielectric structures. *Physical Review Letters*, 65:3152–3155, 1990.

- [12] A. Moroz. Metallo-dielectric diamond and zinc-blende photonic crystals. *Physical Review B*, 66:115109–1 – 115109–15, 2002.
- [13] Fabrication of micro and nanostructures with monodispersed colloidal spheres as the active components. *Material Research Society Symposium Proceedings*, 636:D9.15, 2000.
- [14] F. G-Santamaria, H. T. Miyazaki, A. Urquia, M. Belmonte, N. Shinya, F. Meseguer, and C. Lopez. Nanorobotic manipulation of microspheres for on-chip diamond architectures. *Advanced Materials*, 14(16):1144–1147, 2002.
- [15] Y. Xia, B. Gates, Y. Yin, and Y. Lu. Monodispersed colloidal spheres: Old materials with new applications. *Advanced Materials*, 12(10):693–713, 2000.
- [16] A-P. Hynninen and M. Dijkstra. Phase diagram of hard-core repulsive yukawa particles with a density-dependent truncation: a simple model for charged colloids. *Journal of Physics: Condensed Matter*, 15:S3557–S3567, 2003.
- [17] A-P. Hynninen and M. Dijkstra. Phase diagrams of hard-core repulsive yukawa particles. *Physical Review E*, 68:021407–1 – 021407–8, 2003.
- [18] P. Bartlett, R. H. Ottewill, and P. N. Pusey. Superlattice formation in binary mixtures of hard-sphere colloids. *Physical Review Letters*, 68(25):3801–3805, 1992.
- [19] A. van Blaaderen and P. Wiltzius. Growing large, well-oriented colloidal crystals. *Advanced Materials*, 9(10):833–835, 1997.
- [20] D. J. Norris. A view of the future. *Nature Materials*, 6:177–178, 2007.
- [21] A-P. Hynninen, J. H. J. Thijssen, E. C. M. Vermolen, M. Dijkstra, and A. van Blaaderen. Self-assembly route for photonic crystals with a bandgap in the visible region. *Nature Materials*, 6:202–205, 2007.
- [22] V. Sharma, Q. Yan, C. C. Wong, W. C. Carter, and Y-M. Chiang. Controlled and rapid ordering of oppositely charged colloidal particles. *Journal of Colloid and Interface Science*, 333:230–236, 2009.
- [23] M. E. Leunissen et al. Ionic colloidal crystals of oppositely charged particles. *Nature*, 437:235–240, 2005.
- [24] V. Sharma, D. Xia, C. C. Wong, W. C. Carter, and Y-M. Chiang. Directed self-assembly of 2d heterostructures. *To be submitted*, 2009.
- [25] R. J. Hunter. *Foundations of Colloid Science*. Oxford New York: Oxford University Press, 2 edition, 2001.
- [26] P. C. Hiemenz and R. Rajagopalan. *Principles of Colloid and Surface Chemistry*. Marcel Dekker, New York, 3 edition, 1997.

- [27] A. W. Adamson and A. P. Gast. *Physical Chemistry of Surfaces*. New York, Wiley, 6 edition, 1997.
- [28] J. N. Israelachvili. *Intermolecular and surface forces*. Academic Press, 2 edition, 1991.
- [29] D. J. Shaw. *Introduction to colloid and surface chemistry*. Butterworth-Heinemann, 4 edition, 1992.
- [30] W. B. Russel, D. A. Saville, and W. R. Schowalter. *Colloidal Dispersions (Cambridge Monographs on Mechanics)*. Wiley WCH, 1997.
- [31] J. Goodwin. *Colloids and Interfaces with Surfactants and Polymers: An Introduction*. Wiley WCH, 2003.
- [32] D. Myers. *Surfaces, Interfaces and Colloids: Principles and Applications*. Wiley WCH, 2 edition, 1999.
- [33] W. H. Keesom. On the deduction of the equation of state from boltzmann's entropy principle. *Communications Physical Laboratory, University of Leiden Supplement 24a(121-132):3-20*, 1912.
- [34] W. H. Keesom. On the deduction from boltzmann's entropy principle of the second virial coefficient for materials particles (in the limit of rigid spheres of central symmetry) which exert central forces upon each other and for rigid spheres of central symmetry containing an electric doublet at their centers. *Communications Physical Laboratory, University of Leiden Supplement 24b(121-132):23-41*, 1912.
- [35] W. H. Keesom. On the second virial coefficient for di-atomic gases. *Communications Physical Laboratory, University of Leiden Supplement 25(121-132):3-19*, 1912.
- [36] P. J. W. Debye. Molekularkrafte und ihre elektrische deutung. *Physikalische Zeitschrift*, 22:302-308, 1921.
- [37] P. J. W. Debye. Die van der waalsschen kohasionskrafte. *Physikalische Zeitschrift*, 21:178-187, 1920.
- [38] F. London. The general theory of molecular forces. *Transactions of the Faraday Society*, 33:8-26, 1937.
- [39] F. London. Zur theorie und systematik der molekularkrafte. *Zeitschrift fur Physik*, 63:245-279, 1930.
- [40] R. H. French. Origins and applications of london dispersion forces and hamaker constants in ceramics. *Journal of American Ceramic Society*, 83(9):2117-2146, 2000.

- [41] H. C. Hamaker. The london-van der waals attraction between spherical particles. *Physica*, 4(10):1058–1072, 1937.
- [42] J. H. de Boer. The influence of van der waals' forces and primary bonds on binding energy, strength and orientation, with special reference to some artificial resins. *Transactions of the Faraday Society*, 32:10, 1936.
- [43] V. A. Parsegian. *Van der Waals Forces: A Handbook for Biologists, Chemists, Engineers, and Physicists*. Cambridge University Press, 2006.
- [44] D. B. Hough and L. R. White. The calculation of hamaker constants from liftshitz theory with applications to wetting phenomena. *Advances in Colloid and Interface Science*, 14:3–41, 1980.
- [45] I. E. Dzyaloshinskii, E. M. Lifshitz, and L. P. Pitaevskii. General theory of van der waals forces. *Soviet Physics Uspekhi*, 4:153–176, 1961.
- [46] J. Lyklema. *Fundamentals of Interface and Colloid Science*, volume 2. Academic Press, 1995.
- [47] B. V. Derjaguin and L. Landau. Theory of the stability of strongly charged lyophobic sols and of the adhesion of strongly charged particles in solution of electrolytes. *Acta Physicochimica URSS*, 14:633–662, 1941.
- [48] E. J. W. Verwey and J. Th. G. Overbeek. *Theory of Stability of Lyophobic Colloids*. Elsevier, Amsterdam, 1948.
- [49] H. J. Ohshima. Electrostatic interaction between two dissimilar spheres: Image-interaction correction to the linear superposition approximation. *Journal of Colloid and Interface Science*, 176:7–16, 1995.
- [50] H. J. Ohshima. Electrostatic interaction between two spherical colloidal particles. *Journal of Colloid and Interface Science*, 53:77–102, 1994.
- [51] H. J. Ohshima. Electrostatic interaction between two dissimilar spheres with constant surface charge density. *Journal of Colloid and Interface Science*, 170:432–439, 1995.
- [52] P. S. Kuhn. Melting of a colloidal crystal. *Physica a-Statistical Mechanics and Its Applications*, 247(1-4):235–246, 1997.
- [53] D. Fu et al. Study on osmotic pressure and liquid-liquid equilibria for micelle, colloid and microemulsion systems by yukawa potential. *Chinese Journal of Chemistry*, 22(7):627–637, 2004.
- [54] R. S. Hoy and M. O. Robbins. Fcc-bcc transition for yukawa interactions determined by applied strain deformation. *Physical Review E*, 69(5), 2004.
- [55] J. Dobnikar et al. Poisson-boltzmann brownian dynamics of charged colloids in suspension. *Computer Physics Communications*, 159(2):73–92, 2004.

- [56] F. W. Tavares and J. M. Prausnitz. Analytic calculation of phase diagrams for solutions containing colloids or globular proteins. *Colloid and Polymer Science*, 282(6):620–632, 2004.
- [57] Y. Chem. Effect of size polydispersity on melting of charged colloidal systems. *Chinese Physics Letters*, 20(9):1626–1629, 2003.
- [58] K. S. Schmitz, A. K. Mukherjee, and L. B. Bhuiyan. Screened coulomb pair potential in colloidal interactions in suspensions revisited. *Journal of Physical Chemistry B*, 107(37):10040–10047, 2003.
- [59] L. Yeomans-Reyna. Self-consistent theory of collective brownian dynamics: Theory versus simulation. *Physical Review E*, 67(2), 2003.
- [60] S. N. Petris et al. Modeling the structure of charged binary colloidal dispersions. *Langmuir*, 19(4):1121–1126, 2003.
- [61] S. K. Lai and K. L. Wu. Liquid-liquid and liquid-solid phase separation and flocculation for a charged colloidal dispersion. *Physical Review E*, 66(4), 2002.
- [62] S. Auer and D. Frenkel. Crystallization of weakly charged colloidal spheres: A numerical study. *Journal of Physics: Condensed Matter*, 14(33):7667–7680, 2002.
- [63] J. Dzubiella, G. P. Hoffmann, and H. Lowen. Lane formation in colloidal mixtures driven by an external field. *Physical Review E*, 65(2), 2002.
- [64] L. Yeomans-Reyna and M. Medina-Noyola. Self-consistent generalized langevin equation for colloid dynamics. *Physical Review E*, 64(6), 2001.
- [65] R. Pesche and G. Nagele. Dynamical properties of wall-confined colloids. *European Physics Letters*, 51(5):584–589, 2000.
- [66] H. Lowen and G. P. Hoffmann. Melting of polydisperse colloidal crystals in nonequilibrium. *Physical Review E*, 60(3), 1999.
- [67] A. C. Branka and D. M. Heyes. Algorithms for brownian dynamics computer simulations: Multivariable case. *Physical Review E*, 60(2), 1999.
- [68] E. Huckel. *Physikalische Zeitschrift*, 25:204, 1924.
- [69] M. V. Smoluchowski. *Handbuch der Electricitat und des Magnetismus*, volume 2. Barth, Leipzig, 1921.
- [70] A. B. Jodar-Reyes, J. L. Ortega-Vinuesa, and A. Martin-Rodriguez. Electrokinetic behavior and colloidal stability of polystyrene latex coated with ionic surfactants. *Journal of Colloid and Interface Science*, 297:170–181, 2006.

- [71] D. Qiu, T. Cosgrove, and A. M. Howe. Steric interactions between physically adsorbed polymer-coated colloidal particles: Soft or hard? *Langmuir*, 23:475–481, 2007.
- [72] A-M. Sung and I. Piirma. Electrosteric stabilization of polymer colloids. *Langmuir*, 10(1393-1398), 1994.
- [73] D. H. Napper. The steric stabilization of hydrosols by nonionic macromolecules. *Journal of Colloid and Interface Science*, 29(1):168–171, 1969.
- [74] A. Imhof and D. J. Pine. Stability of nonaqueous emulsions. *Journal of Colloid and Interface Science*, 192:368–374, 1997.
- [75] J. J. Cerda, T. Sintes, and R. Toral. Pair interaction between end-grafted polymers onto spherical surfaces: A monte carlo study. *Macromolecules*, 36:1407–1413, 2003.
- [76] S. Auer, W. C. K. Poon, and D. Frenkel. Phase behavior and crystallization kinetics of poly-12-hydroxystearic-coated polymethylmethacrylate colloids. *Physical Review E*, 67:020401, 2003.
- [77] D. H. Napper. Steric stabilization and the hofmeister series. *Journal of Colloid and Interface Science*, 33(3):384–392, 1970.
- [78] D. H. Napper. Flocculation studies of sterically stabilized dispersions. *Journal of Colloid and Interface Science*, 32(1):106–114, 1970.
- [79] J. Liu and E. Luijten. Colloidal stabilization via nanoparticle halo formation. *Physical Review E*, 72:061401, 2005.
- [80] D. J. Kinning and E. L. Thomas. Hard-sphere interactions between spherical domains in diblock copolymers. *Macromolecules*, 17:1712–1718, 1984.
- [81] A. Doroszkowski and R. Lambourne. The measurement of the dependence of the strength of steric barriers on their solvent environment. *Journal of Colloid and Interface Science*, 43(1):97–104, 1973.
- [82] A. Doroszkowski and R. Lambourne. Measurement of the strength of steric barriers in non-aqueous polymer dispersions. *Journal of Polymer Science: Part C*, 34:253–264, 1971.
- [83] A. K. Dolan and S. F. Edwards. The effect of excluded volume on polymer dispersant action. *Proceedings of Royal Society of London A*, 343:427–442, 1976.
- [84] A. K. Dolan and S. F. Edwards. Theory of the stabilization of colloids by adsorbed polymer. *Proceedings of Royal Society of London A*, 337:509–516, 1974.

- [85] B. A. de L. Costello and P. F. Luckham. Investigation of the interaction forces of polymer-coated surfaces using force balance, rheology, and osmotic pressure results. *Langmuir*, 8:464–468, 1992.
- [86] P. Bagchi. Theory of stabilization of spherical colloidal particles by nonionic polymers. *Journal of Colloid and Interface Science*, 47:86–99, 1974.
- [87] A. Lozsan, M. Garcia-Sucre, and G. Urbina-Villalba. Steric interaction between spherical colloidal particles. *Physical Review E*, 72:061405, 2005.
- [88] E. E. Meyer, Q. Lin, T. Hassenkam, E. Oroudjev, and J. N. Israelachvili. Origin of the long-range attraction between surfactant-coated surfaces. *Proceedings of the National Academy of Sciences*, 102(19):6839–6842, 2005.
- [89] F. Despa and R. S. Berry. The origin of long-range attraction between hydrophobes in water. *Biophysical Journal*, 92:373–378, 2007.
- [90] R. M. Pashley, P. M. McGuiggan, B. W. Ninham, and D. F. Evans. Attractive forces between uncharged hydrophobic surfaces: Direct measurements in aqueous solution. *Science*, 229(4718):1088–1089, 1985.
- [91] Y-H. Tsao, D. F. Evans, and H. Wennerström. Long-range attractive force between hydrophobic surfaces observed by atomic force microscopy. *Science*, 262(5133):547–550, 1993.
- [92] J. N. Israelachvili and R. Pashley. The hydrophobic interaction is long range, decaying exponentially with distance. *Nature*, 300:341–342, 1982.
- [93] Y. Mori. Effect of surface hydrophobicity on interaction between particle and flat plate at final stage of wet coating. *Colloids and Surfaces A: Physicochem. Eng. Aspects*, 311:61–66, 2007.
- [94] W. A. Druker, Z. Xu, and J. N. Israelachvili. Measurements of hydrophobic and dlvo forces in bubble-surface interactions in aqueous solutions. *Langmuir*, 10:3279–3289, 1994.
- [95] D. Landau. *Acta Physicochim*, 14:633, 1941.
- [96] E. J. W. Verwey, J. T. G. Overbeek, and K. van Nes. *Theory of Stability of Lyophobic Colloids: the interaction of sol particles having an electric double layer*. Elsevier, New York, 1948.
- [97] B. D. Gates et al. New approaches to nanofabrication: Molding, printing and other techniques. *Chemical Review*, 105:1171–1196, 2005.
- [98] A. van Blaaderen. Colloids under external control. *MRS Bulletin*, pages 85–90, February 2004.

- [99] G. R. Maskaly. *Attractive Electrostatic Self-Assembly of Ordered and Disordered Heterogeneous Colloids*. PhD thesis, Massachusetts Institute of Technology, 2005.
- [100] G. R. Maskaly, R. E. Garcia, W. C. Carter, and Y-M. Chiang. Ionic colloidal crystals: Ordered, multicomponent structures via controlled heterocoagulation. *Physical Review E*, 73(1), 2006.
- [101] G. R. Maskaly, Y-M. Chiang, W. C. Carter, and R. E. Garcia. Ionic colloidal crystals, US Patent 7,446,130.
- [102] A. Wurger. Capillary attraction of charged particles at a curved liquid interface. *Europhysics Letters*, 75(6):978, 2006.
- [103] A. Yethiraj and A. van Blaaderen. A colloidal model system with an interaction tunable from hard sphere to soft and dipolar. *Nature*, 421:513–516, 2003.
- [104] Y. Monovoukas and A. P. Gast. The experimental phase diagram of charged colloidal suspensions. *Journal of Colloid and Interface Science*, 128(2):533–548, 1989.
- [105] A. van Blaaderen, R. Ruel, and P. Wiltzius. Template-directed colloidal crystallization. *Nature*, 385:321–324, 1997.
- [106] R. Mayoral et al. 3d long-range ordering in an sio2 submicrometer-sphere sintered superstructure. *Advanced Materials*, 9:257–260, 1997.
- [107] H. Miguez, F. Meseguer, C. Lopez, A. Mifsud, J. S. Moya, and L. Vazquez. Evidence of fcc crystallization of sio2 nanospheres. *Langmuir*, 13(23):6009–6011, 1997.
- [108] M. A. Bevan, J. A. Lewis, P. V. Braun, and P. Wiltzius. Structural evolution of colloidal crystals with increasing ionic strength. *Langmuir*, 20(17):7045–7052, 2004.
- [109] M. Holgado et al. Electrophoretic deposition to control artificial opal growth. *Langmuir*, 15(14):4701–4704, 1999.
- [110] S-R Yeh, M. Seul, and B. I. Shraiman. Assembly of ordered colloidal aggregates by electric-field-induced fluid flow. *Nature*, 386:57–58, 1997.
- [111] M. Trau, D. A. Saville, and I. A. Aksay. Assembly of colloidal crystals at electrode interfaces. *Langmuir*, 13(24):6375–6381, 1997.
- [112] K-Q. Zhang and X. Y. Liu. In situ observation of colloidal monolayer nucleation driven by an alternating electric field. *Nature*, 429:739–742, 2004.

- [113] M. Golosovsky, Y. Saado, and D. Davidov. Self-assembly of floating magnetic particles into ordered structures: A promising route for the fabrication of tunable photonic band gap materials. *Applied Physics Letters*, 75(26):4168–4170, 1999.
- [114] L. E. Helseth, H. Z. Wen, R. W. Hansen, T. H. Johansen, P. Heinig, and T. M. Fischer. Assembling and manipulating two-dimensional colloidal crystals with movable nanomagnets. *Langmuir*, 20(17):7323–7332, 2004.
- [115] O. D. Velev and A. M. Lenhoff. *Current Opinions in Colloid and Interface Science*, 5:56, 2000.
- [116] A. S. Dimitrov and K. Nagayama. Continuous convective assembling of fine particles into two-dimensional arrays on solid surfaces. *Langmuir*, 12(5):1303–1311, 1996.
- [117] P. Jiang, J. F. Bertone, K. S. Hwang, and V. L. Colvin. Single-crystal colloidal multilayers of controlled thickness. *Chemistry of Materials*, 11(8):2132–2140, 1999.
- [118] P. A. Kralchevsky and N. D. Denkov. *Current Opinions in Colloid and Interface Science*, 6:383, 2001.
- [119] S. H. Im, M. H. Kim, and O. O. Park. Thickness control of colloidal crystals with a substrate dipped at a tilted angle into a colloidal suspension. *Chemistry of Materials*, 15(9):1797–1802, 2003.
- [120] M. A. McLachlan, N. P. Johnson, R. M. De La Rue, and D. W. McComb. Thin film photonic crystals: synthesis and characterisation. *Journal of Materials Chemistry*, 14:144–150, 2004.
- [121] V. Kitaev and G. A. Ozin. Self-assembled surface patterns of binary colloidal crystals. *Advanced Materials*, 15(1):75–78, 2003.
- [122] N. D. Denkov, O. D. Velev, P. A. Kralchevsky, I. B. Ivanov, H. Yoshimura, and K. Nagayama. Mechanism of formation of two-dimensional crystals from latex particles on substrates. *Langmuir*, 8(12):3183–3190, 1992.
- [123] K. P. Velikov, C. G. Christova, R. P. Dullens, and A. van Blaaderen. Layer-by-layer growth of binary colloidal crystals. *Science*, 296(5565):106–109, 2002.
- [124] Y. Xia, Y. Yin, Y. Lu, and J. McLellan. Template-assisted self-assembly of spherical colloids into complex and controllable structures. *Advanced Functional Materials*, 13(12):907–918, 2003.
- [125] N. V. Dziomkina and G. J. Vancso. Colloid crystal assembly on topologically patterned templates. *Soft Matter*, 1:265–279, 2005.

- [126] N. V. Dziomkina, M. A. Hempenius, and G. J. Vancso. Symmetry control of polymer colloidal monolayers and crystals by electrophoretic deposition onto patterned templates. *Advanced Materials*, 17(2):237–240, 2005.
- [127] J. P. Hoogenboom et al. Template-induced growth of close-packed and non-close-packed colloidal crystals during solvent evaporation. *Nano Letters*, 4(2):205–208, 2004.
- [128] D. Wang and H. Mohwald. Template-directed colloidal self-assembly- the route to 'top-down' nanochemical engineering. *Journal of Materials Chemistry*, 14:458–468, 2004.
- [129] Y. Yin, Y. Lu, B. Gates, and Y. Xia. Template-assisted self-assembly: A practical route to complex aggregates of monodisperse colloids with well-defined sizes, shapes and structures. *Journal of American Chemical Society*, 123:8718–8729, 2001.
- [130] P. Rai-Choudhury, editor. *Handbook of Microlithography, Micromachining, and Microfabrication*, volume 1. SPIE Press, Washington, 1997.
- [131] S. Kuiper, H. A. G. M. van Wolferen, C. van Rijn, W. Nijdam, G. Krijnen, and M. Elwenspoek. Fabrication of microsieves with sub-micron pore size by laser interference lithography. *Journal of Micromechanics and Microengineering*, 11:33–37, 2001.
- [132] C. J. M. van Rijn, G. J. Veldhuis, and S. Kuiper. Nanosieves with microsystem technology for microfiltration applications. *Nanotechnology*, 9:343–345, 1998.
- [133] V. Berger, O. Gauthier-Lafaye, and E. Costard. Fabrication of a 2d photonic bandgap by a holographic method. *Electronics Letters*, 33(5):425, 1997.
- [134] A. Ulman. Formation and structure of self-assembled monolayers. *Chemical Reviews*, 96(4):1533–1554, 1996.
- [135] E. Delamarche, H. Schmid, A. Bietsch, N. B. Larsen, H. Rothuizen, B. Michel, and H. Biebuyck. Transport mechanisms of alkanethiols during microcontact printing on gold. *Journal of Physical Chemistry B*, 102(18):3324–3334, 1998.
- [136] Y. Xia and G. M. Whitesides. Soft lithography. *Angewandte Chemie International Edition*, 37(5):550–575, 1998.
- [137] P. Bertrand, A. Jonas, A. Laschewsky, and R. Legras. Ultrathin polymer coatings by complexation of polyelectrolytes at interfaces: suitable materials, structure and properties. *Macromolecular Rapid Communications*, 21(7):319–348, 2000.
- [138] C. M. Sotomayor Torres. *Alternative Lithography: Unleashing the Potentials of Nanotechnology*. Kluwer Academic, NY, 2003.

- [139] J. Tien, A. Terfort, and G. M. Whitesides. Microfabrication through electrostatic self-assembly. *Langmuir*, 13(20):5349–5355, 1997.
- [140] K. M. Chen, X. Jiang, L. C. Kimerling, and P. T. Hammond. Selective self-organization of colloids on patterned polyelectrolyte templates. *Langmuir*, 16(20):7825–7834, 2000.
- [141] I. Lee, H. Zheng, M. F. Rubner, and P. T. Hammond. Controlled cluster size in patterned particle arrays via directed adsorption on confined surfaces. *Advanced Materials*, 14(8):572–577, 2002.
- [142] J. Aizenberg, P. V. Braun, and P. Wiltzius. Patterned colloidal deposition controlled by electrostatic and capillary forces. *Physical Review Letters*, 84(13):2997–3000, 2000.
- [143] C. A. Fustin, G. Glasser, H. W. Spiess, and U. Jonas. Parameters influencing the templated growth of colloidal crystals on chemically patterned surfaces. *Langmuir*, 20(21):9114–9123, 2004.
- [144] Y. Masuda, T. Itoh, M. Itoh, and K. Koumoto. Self-assembly patterning of colloidal crystals constructed from opal structure or nacl structure. *Langmuir*, 20(13):5588–5592, 2004.
- [145] E. Kumacheva, P. Garstecki, H. Wu, and G. M. Whitesides. Two-dimensional colloid crystals obtained by coupling of flow and confinement. *Physical Review Letters*, 91(12):128301, 2003.
- [146] S. M. Yang and G. A. Ozin. Opal chips: vectorial growth of colloidal crystal patterns inside silicon wafers. *Chemical Communications*, pages 2507–2508, 2000.
- [147] J. Zhang, A. Alsayed, K. H. Lin, S. Sanyal, F. Zhang, W-J Pao, V. S. K. Balagurusamy, P. A. Heiney, and A. G. Yodh. Template-directed convective assembly of three-dimensional face-centered-cubic colloidal crystals. *Applied Physics Letters*, 81(17):3176–3178, 2002.
- [148] Y. Yin and Y. Xia. Growth of large colloidal crystals with their (100) planes oriented parallel to the surfaces of supporting substrates. *Advanced Materials*, 14(8):605–608, 2002.
- [149] Y. Yin, Z-Y Li, and Y. Xia. Template-directed growth of (100)-oriented colloidal crystals. *Langmuir*, 19(3):622–631, 2003.
- [150] S. Matsuo, T. Fujine, K. Fukuda, S. Juodkazis, and H. Misawa. Formation of free-standing micropyrational colloidal crystals grown on silicon substrate. *Applied Physics Letters*, 82(24):4283–4285, 2003.
- [151] D. Wang and H. Moehwald. Rapid fabrication of binary colloidal crystals by stepwise spin-coating. *Advanced Materials*, 16:244–247, 2004.

- [152] Z. Zhou and X. S. Zhao. Flow-controlled vertical deposition method for the fabrication of photonic crystals. *Langmuir*, 20(4):1524–1526, 2004.
- [153] P. Bartlett and A. I. Campbell. Three-dimensional binary superlattices of oppositely charged colloids. *Physical Review Letters*, 95:128302, 2005.
- [154] R. Mukhopadhyay et al. Ordering of binary polymeric nanoparticles on hydrophobic surfaces assembled from low volume fraction dispersions. *Journal of American Chemical Society*, 129(44):13390–13391, 2007.
- [155] E. V. Shevchenko, D. V. Talapin, N. A. Kotov, S. O'Brien, and C.B. Murray. Structural diversity in binary nanoparticle superlattices. *Nature*, 439:55–59, 2006.
- [156] Q. Yan, L. Gao, V. Sharma, Y-M Chiang, and C. C. Wong. Particle and substrate charge effects on colloidal self-assembly in a sessile drop. *Langmuir*, 24(20):11518–11522, 2008.
- [157] M. C. Barbero, J. M. Valpuesta, E. Rial, J. I. G. Gurtubay, F. M. Go, and J. M. Macarulla. *Archives Biochemistry and Biophysics*, 228:560, 1984.
- [158] Y. C. Wu and P. A. Berezansky. Low electrolytic conductivity standards. *Journal of Research of the National Institute of Standards and Technology*, 100:521, 1995.
- [159] A. Martin-Rodriguez, M. S. Romero-Cano, and F. J. de las Nieves. Colloidal stability of a cationic latex covered with triton x-100. *Progress in Colloid and Polymer Science*, 115:1–4, 2000.
- [160] M. Romero-Cano, A. Martin-Rodriguez, and F. de las Nieves. Electrokinetic behaviour of polymer colloids with adsorbed triton x-100. *Colloid and Polymer Science*, 280:526–532, 2002.
- [161] J. Liu, S. Xu, and Z. Sun. Toward an understanding of the turbidity measurement of heterocoagulation rate constants of dispersions containing particles of different sizes. *Langmuir*, 23(23):11451–11457, 2007.
- [162] W. Lin, M. Kobayashi, M. Skarba, C. Mu, P. Galletto, and M. Borkovec. Heteroaggregation in binary mixtures of oppositely charged colloidal particles. *Langmuir*, 22(3):1038–1047, 2006.
- [163] J.A. Marato and F.J. de las Nieves. Influence of the adsorption of non-ionic surfactant triton x-100 on the homocoagulation and heterocoagulation processes of model colloids with equal sizes and opposite sign of charge. *Colloids and Surfaces A: Physiochem. Eng. Aspects*, 145(1-3):271–279, 1998.
- [164] A. M. Islam, B. Z. Chowdhry, and M. J. Snowden. Heteroaggregation in colloidal dispersions. *Advances in Colloid and Interface Science*, 62(2-3):109–136, 1995.

- [165] R. Hogg, T. W. Healy, and D. W. Fuerstenau. *Transactions of the Faraday Society*, 62:1638, 1966.
- [166] V. Sharma. The poisson-boltzmann solver is freely downloadable software written by and available from the author.
- [167] S. Emmett, B. Vincent, J. Edwards, and A. Jones. *Colloids and Surfaces*, 261, 1986.
- [168] M. Campbell, D. N. Sharp, M. T. Harrison, R. G. Denning, and A. J. Turberfield. Fabrication of photonic crystals for the visible spectrum by holographic lithography. *Nature*, 404:53, 2000.
- [169] S. Noda. Three-dimensional photonic crystals operating at optical wavelength region. *Physica B*, 279:142–149, 2000.
- [170] A. Imhof. *Nanoscale Materials*. 423-452. Kluwer Academic Publishers.
- [171] G. A. Ozin and S. M. Yang. The race for the photonic chip: Colloidal crystal assembly in silicon wafers. *Advanced Functional Materials*, 11(2):95–104, 2001.
- [172] V. Sharma, W. C. Carter, and Y-M. Chiang. Ordered colloidal structures and methods of preparation. US Patent Application 61/146,282, filed January 21, 2009., 2009.
- [173] L. K. Leh, N. K. Tan, C. C. Wong, and S. Li. Growth imperfections in three-dimensional colloidal self-assembly. *Applied Physics A: Materials Science and Processing*, 81(7):1399–1404, 2005.
- [174] F. Caruso, H. Lichtenfeld, M. Giersig, and H. Moehwald. Electrostatic self-assembly of silica nanoparticle: Polyelectrolyte multilayers on polystyrene latex particles. *Journal of American Chemical Society*, 120(33):8523–8524, 1998.
- [175] S-L Kuai, X-F Hu, A. Hache, and V. V. Truong. High-quality colloidal photonic crystals obtained by optimizing growth parameters in a vertical deposition technique. *Journal of Crystal Growth*, 267:317–324, 2004.
- [176] J. Hur and Y-Y. Won. Fabrication of high-quality non-close-packed 2d colloid crystals by template-guided langmuir-blodgett particle deposition. *Soft Matter*, 4:1261–1269, 2008.
- [177] P. Jiang, T. Prasad, M. J. McFarland, and V. L. Colvin. Two-dimensional non-close-packed colloidal crystals formed by spin-coating. *Applied Physics Letters*, 89:011908, 2006.
- [178] K. Chari et al. The viscosity of polymer-surfactant mixtures in water. *Journal of Chemical Physics*, 100(7):5294–5300, 1994.

- [179] N. Metropolis, A. W. Rosenbluth, M. N. Rosenbluth, A. N. Teller, and E. Teller. Equation of state calculations by fast computing machines. *Journal of Chemical Physics*, 21:1087–1092, 1953.
- [180] D. Frenkel and B. Smit. *Understanding molecular simulation : from algorithms to applications*. Academic Press, 2 edition, 2002.
- [181] T. M. Truskett, S. Torquato, and P. G. Debenedetti. Towards a quantification of disorder in materials: Distinguishing equilibrium and glassy sphere packings. *Physical Review E*, 62(1):993–1001, 2000.
- [182] J. R. Errington et al. Quantification of order in the lennard-jones system. *Journal of Chemical Physics*, 118(5):2256–2263, 2003.
- [183] J. R. Errington and P. G. Debenedetti. Relationship between structural order and the anomalies of liquid water. *Nature*, 409:318–321, 2001.
- [184] E. Adachi, A. S. Dimitrov, and K. Nagayama. Stripe patterns formed on a glass surface during droplet evaporation. *Langmuir*, 11:1057–1060, 1995.
- [185] Y-H. Ye et al. Self-assembly of colloidal spheres on patterned substrates. *Applied Physics Letters*, 79(6):872–874, 2001.
- [186] L. Onsager. The effects of shape on the interaction of colloidal particles. *Annals of the New York Academy of Sciences*, 51:627–659, 2006.
- [187] G. Chauveteau, M. S. Romero-Cano, A. Martin-Rodriguez, and F. J. de las Nieves. Colloidal stabilization of polystyrene particles by adsorption of nonionic surfactant: II. electrosteric stability studies. *Journal of Colloid and Interface Science*, 198:273–281, 1998.